ISBN 82-471-8198-3 (trykt utg.)
ISBN 82-471-8197-5 (elektr. utg.)
ISSN 1503-8181

NTNU
Norwegian University of
Science and Technology

Hans Kristian Helgesen

Doctoral Thesis

Doktoravhandlinger ved NTNU, 2006:210

NTNU
Norges teknisk-naturvitenskapelige
universitet
Avhandling for graden
doktor ingeniør
Fakultet for naturvitenskap og teknologi
Institutt for fysikk

NTNU

Doktoravhandlinger ved NTNU, 2006:210

Hans Kristian Helgesen

Anisotropic depth migration of converted wave data, inversion of multicomponent data to estimate elastic parameters at the seafloor and one-dimensional data-driven inversion

NTNU
Norwegian University of
Science and Technology

Hans Kristian Helgesen

Anisotropic depth migration of converted wave data, inversion of multicomponent data to estimate elastic parameters at the seafloor and one-dimensional data-driven inversion

Avhandling for graden doktor ingeniør

Trondheim, november 2006

Norges teknisk-naturvitenskapelige universitet
Fakultet for naturvitenskap og teknologi
Institutt for fysikk

NTNU
Det skapende universitet

NTNU
Norges teknisk-naturvitenskapelige universitet

Avhandling for graden doktor ingeniør

Fakultet for naturvitenskap og teknologi
Institutt for fysikk

ISBN 82-471-8198-3 (trykt utg.)
ISBN 82-471-8197-5 (elektr utg.)
ISSN 1503-8181

Doktoravhandlinger ved NTNU, 2006:210

Trykt av Tapir Uttrykk

Anisotropic depth migration of converted wave data, inversion of multicomponent data to estimate elastic parameters at the seafloor and one-dimensional data-driven inversion

Hans Kristian Helgesen

November 20, 2006

Abstract

The increasing demand for oil and gas in the world today drives the need for new and improved methods for identifying hydrocarbon prospects. The petroleum industry uses information about the subsurface in the exploration and production of oil and gas. The industry's tendency to explore deeper waters and more geologically complex areas requires reliable and more robust methods for extracting such information.

This thesis illustrates possible strategies for using seismic reflection data in the inversion for subsurface earth properties. One strategy which is the traditional approach in seismic is to consider inversion as a stepwise procedure consisting of a model-driven global reflectivity imaging process (migration) followed by target-related elastic inversion of the reflectivity information into earth property parameters.

In this thesis a method describing wave equation prestack depth migration of converted wave data in anisotropic media is presented. The migration is accomplished by numerical wavefield extrapolation in the frequency-space domain using precomputed space-variant filter operators. Imaging is performed by crosscorrelating the source wavefield with the data wavefield at each depth level. Data examples demonstrate good dip response and correct kinematic behavior and illustrate the method's ability to handle complex multi-layer models with a relatively high degree of anisotropy.

By considering seismic inversion as a stepwise approach, this thesis also presents a method for inversion of reflection information into medium parameters. The method provides estimation of density and P-wave and S-wave velocities at the seafloor by inversion of the acoustic-elastic PP reflection coefficient estimated at the seafloor. The PP reflection coefficient is calculated in the frequency-slowness domain from seafloor measurements of the pressure and the vertical component of the particle velocity. The algorithm gives estimates of seafloor parameters in good agreement with the true model parameters.

Another strategy for using seismic data in the inversion for subsurface earth properties is to perform inversion as a data-driven procedure where the medium parameters are directly inverted for. In this thesis a new method on inverse scattering for the estimation of the medium properties of a one-dimensional acoustic layered medium from single scattering data is presented. The method provides an explicit, non-iterative and fully data-driven solution of the inverse one-dimensional scattering problem.

Preface

The work presented in this thesis was carried out at the Department of Physics at the Norwegian University of Science and Technology (NTNU).

Outline of the thesis

The thesis is divided into two parts:

Part 1 – Introduction This part contains a introduction to the thesis - the motivation for the work presented and a short summary of the suggested solutions.

Part 2 – Papers In this part my scientific work is presented in the form of four papers. The first and second paper have been prepared for publishing. The third paper is already published. The fourth paper is not ready for publishing yet. The paper is in its present form more like an extension of the third paper and will probably need some restructuring before it can be submitted. The papers included in this thesis are:

Paper 1 Wave equation prestack depth migration of converted wave data in TIV and TIH media
by Hans Kristian Helgesen, Børge Arntsen and Tage Røsten.

Paper 2 Estimation of seafloor wave velocities and density from multicomponent data by AVA analysis
by Hans Kristian Helgesen and Lasse Amundsen.

Paper 3 Data-driven inversion/depth imaging derived from approximations to one-dimensional inverse acoustic scattering
by Lasse Amundsen, Arne Reitan, Hans Kristian Helgesen and Børge Arntsen.

Paper 4 Forward and inverse models in one-dimensional acoustic scattering

Paper 3 is included as published with some exceptions: I have here included one more numerical example together with three additional appendices (with additional references in the main text).

Acknowledgements

During my time as a doctor student I have had my daily working office at Statoil Research Center in Trondheim. With this I want to thank friends at Statoil for interesting conversations, good working conditions and an inclusive social atmosphere. These were elements that made it easier to complete this work.

In particular I am grateful to my supervisors Prof. Lasse Amundsen and Prof. Alex Hansen for giving me the possibility to work on this project. I am indebted to Lasse for sharing his knowledge and experience on migration and inversion with me. I also want to thank Børge Arntsen and Tage Røsten for many interesting discussions and helpful advise during my work, Einar Otnes for good conversations and all help on computer software and Anders Sollid for help on synthetic data modeling.

I want to honor Statoil and the Department of Physics at the Norwegian University of Science and Technology for financial support and for access to their computer facilities. I am also grateful to my present employer, Hydro, for giving me the possibility to finish my doctor work while working as a geophysicist in the company.

To my family:

Jeg vil takke mine foreldre, Kristine og Helge, mine brødre Jan Helge, Roger og Steinar - *vi savner deg*, min søster Lone Lise samt deres familier for all støtte og omtanke. En stor takk til min kjære Inger, som har gitt meg to fantastiske sønner, Hans August og Johan Henrik, som har måttet ta mye av den ekstra belastningen i en travel tid og som alltid har vist stor kjærlighet og tålmodighet. Vi går forhåpentligvis en litt roligere tid i møte.

Kjeller, November 2006

Hans Kristian Helgesen

Contents

List of Figures

List of Tables

Introduction

Chapter 1

Introduction to the thesis

This thesis consists of four separate self-contained papers together with this introduction. Four papers are presented in Chapters 2, 3, 4 and 5, and each paper has its own abstract, introduction and conclusion. A list of references is also given at the end of each paper.

1.1 Motivation for the present work

In the oil and gas industry, various methods for determining subsurface earth properties have been developed to identify and evaluate hydrocarbon prospects. Seismic surveying is probably the most widely used method for extracting such information, but other methods like gravemetric measurements and electro-magnetic surveying are becoming more common, and they are often used in conjunction with seismic in order to reduce risk and optimize recovery of a prospect. The problem of determining earth properties from such measurements is an inverse problem that is theoretically and practically challenging.

General inverse geophysical methods have been the subject of many research papers since the 1970s. In particular, inverse scattering methods from mainstream physics were introduced to the petroleum exploration industry during the late 1970s and early 1980s (see, e.g., Razavy (1975) and Weglein (1985)). As a alternative to full seismic inversion one might consider inversion in steps as described by Berkout and Wapenaar (1990). The inversion in steps consists of three major steps. The first step is a surface-related preprocessing step which involves transformation of the recorded data into primary upgoing and downgoing waves. The second step is reflectivity imaging where the propagation effects are removed from the seismic data by true amplitude prestack migration and structural images of the reflectivity are obtained. The third and final step is a target-related postprocessing procedure which involves transformation of the reflectivity information into earth property parameters. The three major steps can be classified as: (1) Multiple removal, (2) depth migration and (3) amplitude versus angle (AVA) analysis. The stepwise approach to seismic inversion has for many years proven to be a powerful and robust alternative to full seismic inversion.

The three steps in the stepwise inversion procedure have also separately been the subject of many research studies. In the field of seismic data processing it has long been standard practice to seek to attenuate all multiples from the seismic data before using primaries for imaging changes in the medium's properties. The literature on multiple suppression is voluminous [see, e.g., Claerbout (1971), Weglein (1985), Stolt and Benson (1986), and Ikelle and Amundsen (2005)]. The methods for performing seismic migration, which may be considered as the nucleus of "seismic inversion in steps", have during the last forty years undergone a tremendous development from relatively simple migration schemes for homogeneous media to more advanced methods that handle inhomogeneous media, account for anisotropy and preserve amplitudes. Classical references to migration are Claerbout (1971,1985), Schneider (1978), Stolt (1978), Berkhout (1982), and Hubral (1983). More recent references on migration are Holberg (1988), de Bruin *et al* (1990), Hale (1991), Schleicher *et al* (1993), Ristow and Ruhl (1994), Huang and Wu (1996), Gary *et al* (2001), Hill (2001), Ferguson and Margrave (2002), Biondi (2002), Ursin (2004) and Sava and Fomel (2005). If proper amplitude preserving processes have been applied to the seismic data in the demultiple step and migration step, AVA analysis on the reflectivity information can be performed in order to invert for the subsurface earth properties (density and seismic velocities).

Full seismic inversion aims at transforming the seismic measurements into earth property parameters in one large unified inversion procedure. The full inverse scattering problem of seismic, viewed as a 3D problem, is one of the most challenging problems of geophysics and mathematical physics. In the field of seismic inverse scattering, two different solutions for inversely reconstructing the scattering potential have recently been proposed.

Weglein and coworkers have in a series of papers [Weglein *et al* (2000, 2002, 2003), Innanen (2003), Innanen and Weglein (2003), Shaw *et al* (2004), Shaw (2005), Zhang and Weglein (2005), and Liu *et al* (2005)] described a general approach to the problem of inversely reconstructing the potential. The potential to be recovered is expanded in a series, each term of which is determined in terms of the scattering data and a reference Green's function. The approach requires no prior information about the subsurface medium parameters. Further, Weglein and coworkers show the validity of the concept of "subseries" within the expansion of the potential, where each subseries is associated with a specific inversion task that can be carried out separately. The four subseries associated with the inversion process are: (1) Free-surface related multiple removal, (2) internal multiple attenuation or elimination, (3) spatial location of reflectors in the subsurface (depth imaging), and (4) identification of changes in medium properties across reflectors (inversion). The two last subseries work on primaries, that is, those events in the data that have experienced a single upward reflection in the subsurface. The primaries are those reflection events that in the two last subseries are used to determine the locations and properties (contrast in wave velocities) of the reflector that caused their observation (recording at the surface).

The inverse scattering series is exact (Weglein *et al* (2003)). Although all developments based on the inverse scattering series have been very useful for the processing and interpretation of seismic data, it turns out to be extremely challenging to identify all high-order terms related to the subseries for imaging primaries at depth, also for the case of an one-dimensional (1D) layered medium. Even though work is in progress to extend the depth imaging and inversion capability of the inverse scattering series (see, e.g., Innanen, 2003; Innanen and Weglein, 2003), the current depth imaging scheme is based on what is called leading-order inverse scattering. It is well appreciated in physics that approximations play an important role in the understanding of processes that cannot analytically be solved exactly. Depth imaging derived from the inverse scattering series, for 1D media, contains an infinite number of terms of which many, based on physical insight, are neglected to give useful and practical algorithms for imaging (Innanen 2003, and Shaw *et al* 2004).

Realizing that approximations are inevitable at some stage in the inverse scattering series, one is lead to ask: building on the tremendous achievements already obtained by inverse scattering series analysis, can we achieve added understanding of the inverse scattering problem if approximations are introduced into the forward scattering model instead of the inverse scattering series? As a response to this challenge, influenced by the leading-order closed-form 1D depth imaging/inversion algorithms described by Shaw *et* *al* (2003) and Innanen (2003), Amundsen *et al* (2005a, 2005b) suggested a closed-form solution of the 1D inverse scattering problem that is precise when the product of reflection coefficients from any three interfaces of the medium is negligible compared to the reflection coefficients themselves. This approach is now extended to include elastic multidimensional single scattering.

Neither the direct inversion approach based on inverse scattering series nor the direct inversion approach of Amundsen and coworkers require prior information about the subsurface medium parameters below the reference medium within the specific model types for which the methods have been developed, but they require that the scattering data consist of primaries only. All types of multiples that are normally recorded in the seismic experiment need to be removed or well attenuated through data preprocessing. The preprocessing is in agreement with the standard practice to seek to attenuate all multiples from seismic data before using primaries for imaging changes in the medium's properties. Furthermore, they require an estimate of the seismic wavelet.

The increasing demand for oil and gas in the world today drives the need for reliable and more robust methods for identifying hydrocarbon prospects. Information about the subsurface is used in the petroleum industry both to identify and evaluate possible prospects and to help the planning of wells and to monitor changes in the reservoir due to production. The development of new and improvement of existing methods for extracting such information is important in order to correctly evaluate and optimize the recovery of a prospect.

1.2 Summary

In this thesis I consider inversion and migration of seismic data in order to extract information from the subsurface. The work I present here represent development of new and improvement of existing methods for extracting such information which is used in the exploration and recovery of hydrocarbons.

In Chapter 2 a paper describing wave equation prestack depth migration of converted wave data in anisotropic media is presented. The anisotropy considered is that of a transversely isotropic (TI) medium with a symmetry axis that can be either vertical (TIV) or horizontal (TIH). The migration is accomplished by numerical wavefield extrapolation in the frequency-space domain where the upgoing and downgoing wavefields are extrapolated in depth with space-variant filter operators. The filter operators are precomputed in a separate design program and accessed by the migration algorithm. Imaging is performed by crosscorrelating the source wavefield with the data wavefield at each depth level. The method is evaluated based on a study of migration impulse responses, a synthetic data example and a real data example. Data examples demonstrate good dip response and correct kinematic behavior and illustrate the method's ability to handle complex multi-layer models with a relatively high degree of anisotropy. The paper is prepared for publishing in an international journal.

In Chapter 3 a paper describing estimation of density and P-wave and S-wave velocities at the seafloor is presented. The parameters are estimated by inversion of the acoustic-elastic reflection coefficient calculated from point-source measurements of pressure and vertical component of particle velocity recorded at the seafloor. A regular Fourier transform (FT) is used to transform the pressure and particle velocity recordings from time domain to frequency domain while a triangle-Fourier transform (T-FT) is used to transform the data from space domain to radial slowness domain. The reflection coefficient is then calculated by spectral division of the transformed two-component recordings. By performing the spectral division in the frequency-radial slowness domain we obtain a calculated reflection coefficient that is directly comparable to the theoretical reflection coefficient. The paper is prepared for publishing in an international journal.

Chapter 4 presents a new mathematical framework based on inverse scattering for the estimation of the scattering potential and its nature of a one-dimensional acoustic layered medium from single scattering data. Given the Born potential associated with constant-velocity imaging of the single scattering data, a closed-form, implicit expression for the scattering potential is derived in the WKBJ and eikonal approximations. Adding physical insight, the WKBJ and eikonal solutions can be adjusted so that they conform to the geometrically-derived precise solutions of the 1D scattering problem recently suggested by Amundsen *et al* (2005a). In a layered medium the WKBJ and eikonal approximations, in addition to providing an implicit solution for the scattering potential, provide an explicit estimate of the potential, not within the actual potential discontinuities (layer interfaces), but within the Born potential discontinuities derived by the constant velocity imaging. This estimate of the potential is called the “squeezed” potential since it mimics the actual potential when the depth axis is squeezed so that the discontinuities of the actual potential match those of the Born potential. In the 1D case, it is shown that the squeezed potential can be estimated by amplitude-scaling the Born potential by an amplitude function of the Born potential. The accessibility of the squeezed potential makes the inverse acoustic scattering problem explicit and non-iterative since the estimated squeezed potential can non-linearly be stretched with respect to the depth axis so that the potential discontinuities are moved towards their correct depth location. The non-linear stretch function is a function of the Born potential. The solution is fully data-driven in the respect that no information of the medium other than the Born potential is required. In the nomenclature of reflection seismic, the three steps of the non-iterative, data-driven inverse solution are constant-velocity migration, inversion and residual migration (stretch). The paper is published in Inverse Problems **21** (1823-1850).

In Chapter 5 a new and improved forward model for single scattering of acoustic waves in a 1D stratified medium is derived. The new model is inverted following the same strategy as described in Chapter 4. The model is then compared with the model already considered in Chapter 4. The models are compared both with regards to the amplitude handling in the forward modeling and with regards to inversion results.

References

Amundsen L, Reitan A and Arntsen B 2005a Geometric analysis of data-driven inversion/depth imaging *Journal Seismic Exploration* **14** 51-62

Amundsen L, Reitan A, Helgesen H K and Arntsen B 2005b Data-driven inversion/depth imaging derived from approximations to one-dimensional inverse acoustic scattering *Inverse Problems* **21** 1823-1850

Berkhout A J 1982, *Seismic Migration, Imaging of Acoustic Wave Energy by Wavefield Extrapolation, A: Theoretical Aspects* 2nd edn (Amsterdam: Elsevier)

Berkhout A J and Wapenaar C P A 1990 DELPHI: Delft philosophy on acoustic and elastic inversion, Part 1 *The Leading Edge* **9** No. 2 30-33

Biondi B 2002 Stable wide-angle Fourier finite-difference downward extrapolation of 3-D wavefields *Geophysics* **67** 872-882

Claerbout J F 1971 Towards a unified theory of reflector mapping *Geophysics* **36** 467-481

Claerbout J F 1985 Imaging the Earth's interior *Blackwell Scientific Publications*

de Bruin C G M, Wapenaar C P A and Berkhout A J 1990 Angle-dependent reflectivity by means of prestack migration *Geophysics* **55** 1223-1234

Ferguson R J and Margrave G F 2002 Depth imaging in anisotropic media by symmetric non-stationary phase shift *Geophys. Prosp.* **50** 281-288

Gray S H, Etgen J, Dellinger J and Whitmore D 2001 Y2K Review Article: Seismic migration problems and solutions *Geophysics* **43** 23-48

Hale D 1991 Stable explicit depth extrapolation of seismic wavefields *Geophysics* **56** 1770-1777

Hill N R 2001 Prestack Gaussian-beam depth migration *Geophysics* **66** 1240-1250

Holberg O 1988 Towards optimal one-way wave propagation *Geophys. Prosp.* **36** 99-114

Huang L Y and Wu R S 1996 Prestack depth migration with acoustic screen propagators *66th Annual International Meeting, SEG, Expanded Abstracts* 415-418

Hubral P 1983 Computing true amplitude reflections in a laterally inhomogeneous Earth *Geophysics* **48** 1051-1062

Ikelle L T and Amundsen L 2005 *Introduction to petroleum seismology* (Society of Exploration Geophysics)

Innanen K A 2003 *Methods for the treatment of acoustic and absorptive/dispersive wave field measurements* (Ph.D. thesis, University of British Columbia)

Innanen K A and Weglein A B 2003 Simultaneous imaging and inversion with the inverse scattering series *Proc. 8th Internat. Cong. of the SBGf and 5th Latin American Geophys. Conf.*

Liu F, Weglein A B, Innanen K A, and Nita B G, 2005, Extension of the non-linear depth imaging capability of the inverse scattering series to multidimensional media: strategies and numerical results *Proc. 9th Internat. Cong. of the SBGf and 6th Latin American Geophys. Conf.*

Razavy M 1975 Determination of the wave velocity in an inhomogeneous medium from the reflection coefficient *J. Acoust. Soc. Am.* **58** 956-963

Ristow D and Ruhl T 1994 Fourier finite-difference migration *Geophysics* **59** 1882-1893

Sava P and Fomel S 2005 Riemannian wavefield extrapolation *Geophysics* **70** T45-T56

Schleicher J, Tygel M and Hubral P 1993 3-D true-amplitude, finite-offset migration *Geophysics* **58** 1112-1126

Schleicher W A 1978 Integral formulation for migration in two and three dimensions *Geophysics* **43** 49-76

Shaw S A 2005 *An inverse scattering series algorithm for depth imaging of reflection data from a layered acoustic medium with an unknown velocity model* (Ph.D. thesis, University of Houston)

Shaw S A, Weglein A B, Foster D J, Matson K H and Keys R G 2004 Isolation of a leading order depth imaging series and analysis of its convergence properties for a 1D acoustic medium *J. Seis. Expl.* **13** 99-120

Stolt R H 1978 Migration by Fourier transforms *Geophysics* **43** 23-48

Stolt R H and Benson A K 1986 *Seismic migration: Theroy and Practice* (London: Geophysical Press)

Ursin B 2004 Tutorial: Parameter inversion and angle migration in anisotropic elastic media *Geophysics* **69** 1125-1142

Weglein A B 1985 The inverse scattering concept and its seismic application *Developments in Geophysical Exploration Methods* vol 6, ed A A Fitch (Amsterdam: Elsevier) pp 111-138

Weglein A B, Araújo R V, Carvalho P M, Stolt R H, Matson K H, Coates R T, Corrigan D, Foster D J, Shaw S A and Zhang H 2003 Inverse scattering series and seismic exploration *Inverse Problems* **19** R27-R83

Weglein A B, Foster D J, Matson K H, Shaw S A, Carvalho P M and Corrigan D 2002 Predicting the correct spatial location of reflectors without knowing or determining the precise medium and wave velocity: initial concept, and analytic and numerical example *J. Seis. Expl.* **10** 367-382

Weglein A B, Matson K H, Foster D J, Carvalho P M , Corrigan D and Shaw S A 2000 Imaging and inversion at depth without a velocity model: theory, concepts, and initial evaluation *Expanded Abstracts, 70th Ann. Internat. Mtg., Soc. Expl. Geophys.*

Zhang H and Weglein A B 2005 The inverse scattering series for tasks associated with primaries: depth imaging and direct non-linear inversion of 1D variable velocity and density acoustic media *Expanded Abstracts, 75th Ann. Internat. Mtg., Soc. Expl. Geophys.*

Papers

Chapter 2

Wave equation prestack depth migration of converted wave data in TIV and TIH media

Abstract

This paper describes prestack depth migration of converted wave data in transversely isotropic (TI) media where the symmetry axis is either vertical (TIV) or horizontal (TIH). The migration is accomplished by numerical wavefield extrapolation in the frequency-space domain where the upgoing and downgoing wavefields are extrapolated in depth with space-variant filter operators. The filter operators are precomputed in a separate design program and accessed by the migration algorithm. The ratio between the temporal frequency and the local velocity, together with the anisotropic parameters and wave mode (qP or qSV), are used to determine the correct filter operator at each grid point during the wavefield extrapolation. Imaging is performed by crosscorrelating the source wavefield with the data wavefield at each depth level. The method is evaluated based on a study of migration impulse responses, a synthetic data example and a real data example. Impulse responses demonstrate good dip response and correct kinematic behavior and the synthetic data example illustrates the method's ability to handle complex models with a relatively high degree of anisotropy. The real data example shows that the method is applicable to real data and that correcting for anisotropy might be very important in converted wave imaging.

2.1 Introduction

Depth migration is the preferred imaging technique for both compressional wave data (P-P data) and converted wave data (P-S data). Earlier studies regarding imaging indicate that wave equation based prestack depth migration techniques provide better solutions to the imaging problem than traditional Kirchhoff techniques. We want to utilize the strengths of wave equation based prestack depth migration for converted wave imaging where we in addition include proper handling of anisotropy.

Depth imaging of P-S data can be accomplished and will usually provide better images than time imaging methods. Depth imaging of P-P data and P-S data will also provide images that have the same depth axis (as opposed of P-P and P-S time axes). Depth images of P-P data and P-S data may therefore be easier to correlate and interpret than time images. Several case studies considering isotropic, Kirchhoff prestack depth migration of converted wave data illustrate the benefits of performing imaging in depth rather then imaging in time. Kendall *et al* (1998) reported that prestack depth migration of converted wave data from the Mahogany field (Gulf of Mexico) allowed better imaging than time imaging of the shallow sediments above salt as well as for imaging salt and below salt. The added shear wave information also helped improve reservoir characterization by providing further constrains on the rock properties, lithology and fracture density and orientation. Hoffe and Lines (1999) showed in a case study from the Blackfoot field (Alberta, Canada) that depth migrated P-S sections might have similar or even better resolution than the depth migrated P-P sections, and that converted wave information allows for enhanced lithology discrimination, especially between sandstones and shales. Zhu *et al* (1999) used prestack depth imaging for imaging complex salt dome structures and showed that not only is depth migration the preferred product for P-wave data, it is also the preferred product for converted waves. Common for all the depth imaging studies above is that the imaging methods are based on Kirchhoff prestack depth migration.

Wave equation based prestack depth migration techniques might provide better solutions to the imaging of converted wave data than the traditional Kirchhoff techniques. In areas with complex structures and strong lateral velocity variations several examples using compressional waves have shown that depth migration based on wave equation algorithms give significantly better results than Kirchhoff depth migration methods. Jin *et al* (2002) developed a pseudoscreen prestack depth migration technique and used synthetic 2D and 3D P-data to demonstrate that the technique is superior to Kirchhoff implementations when considering image quality. Rousseau *et al* (2003) presented a 3D depth imaging technique using generalized screens in a case study and showed that the wave equation approach to prestack depth migration produces better images than the equivalent Kirchhoff approach. Arntsen and Røsten (2002) and Soubaras (2002) have also reported that wave equation based imaging techniques provide better images than traditional Kirchhoff imaging techniques. We expect that wave equation depth migration algorithms give better results than Kirchhoff depth migration methods also for converted waves. Several authors have investigated methods for wave equation based prestack depth migration using compressional waves. Holberg (1988) presented a scheme for 2D numerical wavefield extrapolation in the frequency-space domain using space-variant symmetric filter operators designed based on a least-squares method. Hale (1991) considered a modified Taylor series method for designing the explicit filter operators for wavefield extrapolation. Sollid and Arntsen (1993) extended the work of Holberg (1988) to describe wave extrapolation in 3D. In all these papers the wave extrapolation algorithms were derived and tested with respect to extrapolation of compressional waves in isotropic media. These techniques can however, easily be modified to handle extrapolation of converted waves in anisotropic media.

The earth is anisotropic in nature and especially sedimentary rocks exhibit anisotropy. These sedimentary rocks may often be described as being transversely isotropic (TI) with a symmetry axis perpendicular to the bedding plane. A homogeneous medium which is fractured may also be described as being TI, now with a symmetry axis perpendicular to the fractures. Seismic waves are affected by anisotropy and converted waves are more affected than compressional waves. In areas with complex structures, strong lateral velocity variations and possibly anisotropy, one must consider anisotropic depth migration for correct imaging of converted wave data. Thomsen (1986) considered wave propagation in elastic anisotropic media. Uzcatequi (1995) combined the work of Holberg (1988) and Thomsen (1986) and derived formulas for seismic wavefield depth extrapolation in TI media with a vertical symmetry axis (TIV). Zhang *et al* (2001) extended the work of Holberg (1988) and developed a method for wavefield depth extrapolation in TI media with a tilted symmetry axis using asymmetric numerically optimized explicit filter operators. The techniques of Uzcatequi (1995) and Zhang *et al*

(2001) were tested on synthetic models using simulated P-data and S-data separately.

In this paper, a method for anisotropic wave equation prestack depth migration of converted wave data is presented. The migration is accomplished by numerical wavefield extrapolation where the upgoing and downgoing wavefields are extrapolated in depth with space-variant filter operators. The explicit filter operators are designed using a constrained least-squares method. Imaging is performed by a crosscorrelation of the upgoing and downgoing wavefields at each depth level. The method is valid for TI media with either a vertical (TIV) or a horizontal (TIH) axis of symmetry and arbitrary strength of the anisotropy. The method is evaluated based on a study of migration impulse responses, a synthetic data example and a real data example.

2.2 Methodology

In this section a more detailed description of the prestack depth migration is presented. The migration is expressed as a wavefield extrapolation step followed by an imaging step. The wavefield extrapolation is accomplished by space variant convolution in the frequency-space domain and imaging is performed by crosscorrelating the upgoing wavefield with the downgoing wavefield divided by the source illumination at each depth level. The space variant extrapolation operators are precomputed in a separate operator design program and accessed by the migration algorithm. The problem of designing proper extrapolation operators is formulated as a linear least-squares filter optimization problem with non-linear constraints.

2.2.1 Prestack depth migration algorithm

Most prestack depth migration algorithms can be expressed as a wavefield extrapolation step followed by an imaging condition. Usually we consider one-way wavefield extrapolation, where the upgoing receiver wavefield (U) and the downgoing source wavefield (D) are extrapolated in depth by appropriate extrapolation operators. In 2D, one-way downward wavefield extrapolation (the z-direction is positive downwards) may be expressed in the frequency-wavenumber domain by

$$P(\omega, k_x, z + \Delta z) = \exp[ik_z \Delta z] P(\omega, k_x, z), \tag{2.1}$$

where ω is (angular) frequency, k_x and k_z are horizontal and vertical wavenumber, respectively. $P(\omega, k_x, z + \Delta z)$ is the extrapolated wavefield at depth $z + \Delta z$ and $P(\omega, k_x, z)$ is the wavefield at depth z.

Wavefield extrapolation by application of equation (2.1) is, strictly speaking, only valid for a homogeneous medium. However, by doing wavefield extrapolation iteratively in depth and assuming that the velocity model is locally smooth, a laterally-varying extrapolator may be applied such that inhomogeneous velocity fields can be handled. The extrapolation operator may be approximately represented by a finite-length discrete filter (Holberg (1988)) to obtain spatially varying extrapolators. This is also described in more detail in Appendix 2.B. Downward wavefield extrapolation can then be expressed as a space-variant convolution in the frequency-space domain by

$$P(\omega, x, z + \Delta z) = \sum_{l=0}^{L} w_l [P(\omega, x + l\Delta x, z) + P(\omega, x - l\Delta x, z)], \qquad (2.2)$$

where w_l are the numerically optimized discrete complex-valued filter coefficients of the appropriate filter with total length $(2L + 1)$. The filter is then an approximation of the exact extrapolation operator. Here is Δz the extrapolation step length in the vertical direction while Δx is the horizontal distance between data points. In TIV and TIH media the filter coefficients become functions of ω/V_{P0}, the Thomsen (1986) parameters ε, δ and the ratio V_{P0}/V_{S0}. The filter coefficients will also depend on wave mode (qP or qSV). V_{P0} and V_{S0} are the vertical qP- and qSV-wave velocities, respectively. The Thomsen (1986) parameters ε and δ describe the strength of the anisotropy.

The wavefield extrapolation is done separately for the receiver and the source wavefields and an image can be obtained by crosscorrelation of the two extrapolated wavefields. The crosscorrelation imaging technique used is similar to the one presented by Claerbout(1971) and can be expressed as

$$I(x, z) = \int \frac{U(\omega, x, z) D^*(\omega, x, z)}{(D(\omega, x, z) D^*(\omega, x, z) + \lambda)} d\omega, \qquad (2.3)$$

where $I(x, z)$ is the image at position (x, z), $U(\omega, x, z)$ represents the upgoing wavefield at depth z (the backward extrapolated receiver wavefield) and $D(\omega, x, z)$ represents the downgoing wavefield at depth z (forward extrapolated source wavefield). Superscript $*$ indicates the complex conjugate and λ is a pre-whitening factor to stabilize the deconvolution-like operation.

2.2.2 Explicit migration operators

The exact representation of the extrapolation operator may be expressed in the frequency-wavenumber domain as

$$G(\omega, k) = \exp[ik_z \Delta z]. \tag{2.4}$$

For TI media with a symmetry axis lying in the vertical plane and making an angle ϕ with the vertical axis, the phase velocities for qP- and qSV-waves can be expressed exactly as (Tsvankin (1996))

$$\begin{aligned}\frac{V^2(\theta)}{V_{P0}^2} &= 1 + \varepsilon \sin^2(\theta - \phi) - \frac{f}{2} \\ &\pm \frac{f}{2}\sqrt{\left(1 + \frac{2\varepsilon \sin^2(\theta - \phi)}{f}\right)^2 - \frac{2(\varepsilon - \delta)\sin^2 2(\theta - \phi)}{f}},\end{aligned} \tag{2.5}$$

where θ is the phase angle and $f = 1 - V_{S0}^2/V_{P0}^2$. The ± in equation (2.5) gives the phase velocities for qP- and qSV-waves, respectively.

By introducing plane waves in equation (2.5) and setting $\phi = 0$ (see Appendix 2.A) yields a dispersion equation for TIV media which becomes

$$k_z = \pm\sqrt{\frac{-a \pm \sqrt{a^2 - 4b}}{2}}, \tag{2.6}$$

where ± in front of the square-root is related to up- or down-going waves and the ± inside the square-root is related to qSV- or qP-waves, respectively. The coefficients a and b are given by (subscript TIV indicates coefficients for TIV media)

$$a_{\text{TIV}} = \frac{-2(1 + \varepsilon - f - f\delta)k_x^2 + (\frac{\omega}{V_{P0}})^2(2 - f)}{(f - 1)} \tag{2.7}$$

and

$$b_{\text{TIV}} = \frac{(2 + 2\varepsilon - f)(\frac{\omega}{V_{P0}})^2 k_x^2 - (\frac{\omega}{V_{P0}})^4 - (1 - f)(1 + 2\varepsilon)k_x^4}{(f - 1)}. \tag{2.8}$$

For TIH media (setting $\phi = 90$) we will get a similar dispersion equation as given by (2.6). The coefficients a and b are now given by (subscript TIH indicates coefficients for TIH media)

$$a_{\text{TIH}} = \frac{(-2(1 + \varepsilon - f - f\delta)k_x^2 + (\frac{\omega}{V_{P0}})^2(2 + 2\varepsilon - f))}{(f - 1)(1 + 2\varepsilon)} \tag{2.9}$$

and

$$b_{\text{TIH}} = \frac{(2-f)(\frac{\omega}{V_{P0}})^2 k_x^2 - (\frac{\omega}{V_{P0}})^4 - (1-f)k_x^4}{(f-1)(1+2\varepsilon)}. \tag{2.10}$$

The dispersion equation (2.6) will provide the exact phase-shift extrapolation operator for qP- and qSV-waves propagating in either TIV or TIH media.

The approximation of the extrapolation operator $G(\omega, k)$ can be formulated as a numerical optimization problem of finding the filter coefficients w_l (as introduced in equation (2.2)) of a finite-length filter that approximates the exact phase-shift extrapolator defined in equation (2.4) in the frequency-wavenumber domain. This is done in a least-squares sense. To ensure stability of the migration scheme, the optimization of the operators is constrained such that the evanescent energy and waves propagating at higher angles than a chosen maximum design angle are damped in the iterative downward extrapolation process. The problem of designing the filter operators is described in more detail in Appendix 2.B.

2.2.3 The implementation

The implementation of the prestack depth migration scheme is subdivided into two separate parts. One operator design program and one extrapolation and imaging program (migration algorithm). The filter operator design program is implemented as a numerical optimization problem where the phase and amplitude errors of the approximated operator are minimized compared to the exact extrapolation operator. The exact operator $G(\omega, k)$ is given equation (2.4). The vertical wavenumber k_z is given by equation (2.6) where the coefficients a and b are for TIV media given by equation (2.7) and equation (2.8), respectively. For TIH media are the coefficients a and b given by equation (2.9) and equation (2.10), respectively. The migration algorithm is implemented by direct translation of equation (2.2) which is the wavefield extrapolation step. At each depth level in the extrapolation an imaging condition given by equation (2.3) is applied. In the migration algorithm we have included a source function to represent the source wavefield. The constructed source wavefield and the input receiver wavefield (the recorded reflection data) are the two wavefields needed to perform the migration. In addition to the wavefields and the velocity models, the anisotropic parameter models and the precomputed migration operators are input to the migration algorithm.

The first step in the migration scheme is to design proper migration operators as described above. These are designed based on investigation of the velocity models and the anisotropic parameter models. The anisotropic parameter models (ε model and δ model) and the V_{S0}/V_{P0} ratio model define a combined model called media type model. A media type is defined by its ε value, δ value and V_{S0}/V_{P0} ratio. One set of operators is designed for each wave mode (qP and qSV) and media type and each set of operators is designed for a range of ω/V_{P0} ratios, stored in tables and later accessed in the wavefield extrapolation process. The next step is then to prepare the velocity models, the anisotropy models and the reflection data together with the precomputed extrapolation operators for input to the migration algorithm. In the migration, the anisotropic parameter models and the velocity models are used to determine the correct operator at each spatial grid point during the downward extrapolation of the source and receiver wavefields. The flow of processes is also illustrated in figure 2.1.

The problem of finding proper models when considering real earth experiments is often a difficult and time consuming task. This is especially true for the anisotropic models. Without dwelling upon how both velocity models and anisotropic models may be found we simply state that the way these models often are generated result in continuously varying models (as opposed to layer by layer models). Because of this the number of mediatypes (defined by its ε, δ and V_{S0}/V_{P0} ratio) for a specific real earth experiment may become extremely large. This would then result in an impractically large number of operators to be designed.

For situations where continuously varying anisotropic models are used in the migration an approximated migration scheme can be proposed. By investigation of the anisotropic parameter models and the velocity models we determine the extreme anisotropic parameters ε_{min}, ε_{max}, δ_{min} and δ_{max}, together with $(V_{P0}/V_{S0})_{min}$ and $(V_{P0}/V_{S0})_{max}$ which are the minimum and maximum anisotropic parameters and (V_{P0}/V_{S0}) ratios found in our models. We then design a set of operators for all possible combinations of the anisotropic parameters and (V_{P0}/V_{S0}) ratios within the ranges $[\varepsilon_{min}\ ;\ \Delta\varepsilon\ ;\ \varepsilon_{max}]$, $[\delta_{min}\ ;\ \Delta\delta\ ;\ \delta_{max}]$ and $[(V_{P0}/V_{S0})_{min}\ ;\ \Delta(V_{P0}/V_{S0})\ ;\ (V_{P0}/V_{S0})_{max}]$. The increments $\Delta\varepsilon$, $\Delta\delta$ and $\Delta(V_{P0}/V_{S0})$ must be chosen so they reflect a proper sampling of the parameter models. Each set of operators is designed for a range of of ω/V_{P0} ratios and operators for both qP-mode propagation and qSV-mode propagation are prepared. In the migration, the anisotropic parameter models and the velocity models are then used to determine the nearest operator to use at each spatial grid point during the downward extrapolation.

In the migration algorithm we have also included the option to input reflection data sorted either as common shot records or common receiver records. The migration scheme which we present is suitable for common shot records because we can use the same filter operator for wavefield extrapolation of individual common shot records. Depth migration is performed on all individual common shot records followed by a common image-point stacking to obtain the final depth migrated stacked section. By considering reciprocity of particle velocity (which is the physical quantity that is measured in the recording of the reflection data) and monopole sources, we may treat a common receiver gather as a common shot gather (source and receiver positions are interchanged) in the migration process, provided that the particle velocity component and the force component from the source are interchanged.

2.3 Numerical Results

The performance of the suggested migration scheme is evaluated through a study of migration impulse responses, one synthetic and one real data example. The data examples show that the migration scheme ensures correct positioning of both P-P and P-S reflection events for complex models and that it is applicable to real data provided that accurate models (velocity models and anisotropic models) are available.

The impulse responses for P-P, S-S and P-S migration in TIV and TIH media are presented in figures 2.2 to 2.7 and figures 2.8 to 2.13, respectively. Impulse responses for a weak anisotropic medium and a strong anisotropic medium are presented for both TIV and TIH symmetries. The medium parameters for the weak anisotropic medium and the strong anisotropic medium are presented in table 2.1 and are the same for both TIV and TIH symmetries. The input data to the migration is a spike at 1 second - two-way traveltime (together with the velocity models and the anisotropic models). For all impulse responses examples, 41-point (L=20) symmetric extrapolation operators are used.

To evaluate the kinematic behavior of the migration technique we project the correct depth surface in black on the P-P and S-S impulse responses. We also project the corresponding isotropic depth surface in white for comparison. The derivation of the correct depth surfaces (overlay functions) are given in Appendix 2.C. For P-P impulse responses presented in figures 2.2, 2.3, 2.8 and 2.9 we see excellent kinematic behavior for both weak and strong anisotropic medium (both TIV and TIH media) for all angles (phase angles) up to the maximum design angle, which for this case is 70 degrees. For the S-S impulse responses presented in figures 2.4, 2.5, 2.10 and 2.11 we also see excellent kinematic behavior for both weak and strong anisotropic medium (both TIV and TIH media), up to 45 degrees. Beyond this, for angles between 45 degrees and up to the maximum design angle we see a small misfit between the S-S impulse responses and the correct depth surface for both weak anisotropic media and strong anisotropic media. The error in positioning is increasing with increasing angle and is somewhat more pronounced for the strong anisotropic medium. The misfit can be related to phase errors in the approximation of the extrapolation operator. We have calculated the maximum misfit between the S-S impulse response and the correct depth surface to be 2 samples in either direction for the weak anisotropic medium (figures 2.4 and 2.10) and 4 samples in either direction for the strong anisotropic medium (figures 2.5 and 2.11). We consider this error in positioning at high angles to be small and within acceptable limits. Based on these calculations we conclude that the impulse responses (figures 2.2 to 2.13) show good kinematic behavior for both P-P migration and S-S migration, and therefore also P-S migration for both weak and strong anisotropy.

The migration algorithm is further evaluated using a synthetic data example. Typical input gathers to the migration are presented in figures 2.14 and 2.15. The P-P and P-S images from the synthetic data example are presented in figures 2.16 and 2.17. The model consist of seven layers including the water-layer (the water-bottom reflection is not being modeled). The model parameters are summarized in table 2.2 and the model interfaces are overlayed the migrated images presented in figures 2.16 and 2.17. We are here considering TIV symmetry. The synthetic data is generated using a Kirchhoff integral modeling scheme that models P-P and P-S data which are kinematically correct. The modeling is performed in the CDP-offset domain (common depth point - offset domain). A total of 340 CDP's is modeled with a CDP increment of 10 meters. The maximum offset is 1600 meters (split spread) with an offset increment of 20 meters. The temporal sampling interval is 4 milliseconds. The modeled data (sorted into common shot records) together with the velocity models and the anisotropic models are then input to the anisotropic migration algorithm. In figures 2.14 and 2.15 examples of common shot-gathers for both P-P and P-S data are displayed. After migration the migrated shot records are sorted into common image-point gathers which then are stacked to obtain the final images presented in figures 2.16 and 2.17. All operators used are 41-point (L=20) symmetric extrapolation operators.

For comparison between the exact model and the migrated images we have plotted the correct depth surfaces in white on to the P-P- and P-S images. We see that there is a very good agreement between the migrated images and the correct depth surfaces.

Finally, the migration algorithm is applied to a real data set. The multicomponent data used in the real data example was acquired over the Volve field (North Sea) in 1999. From the original $3D$ data a $2D$ line is selected for input to the migration. Pre-processing of the selected data involves summation of the pressure and vertical velocity component for multiple suppression on the P-P data and rotation analysis on the horizontal velocity components for wave mode identification on the P-S data. Both P-P and P-S data is then sorted into common receiver gathers (CRG) and input to the migration. In figures 2.18 and 2.19 examples of common receiver-gathers for both P-P and P-S data are displayed. A total of 240 CRGs with a CRG interval of 25 meters is used in the migration. Each CRG consist of 560 shots with a shot interval of 25 meters. The temporal sampling interval is 4 milliseconds. Velocity models and anisotropic models are also input to the migration. The ε model ranges from zero to 0.1, the δ model is zero and the V_{P0}/V_{S0} ratio varies from 2 to 2.6. The degree of anisotropy is therefore considered to be weak (we are however using exact equations in the operator design and migration algorithm). It should be mentioned that these models (especially the anisotropic models) are probably not the optimal models to use in the migration as these models are being refined as we speak. This will of course have an impact on the performance of the migration scheme. After migration the migrated CRGs are sorted into common image-point gathers and stacked to produce the final images presented in figures 2.20 and 2.21. For comparison, the input data is also migrated using the isotropic migration scheme where anisotrophy is not considered (the anisotropic models are set to zero), while the same velocity models are being used. The final images using isotropic migration are presented in figures 2.22 and 2.23. All operators used are 41-point (L=20) symmetric extrapolation operators.

Comparing the two P-P sections we see some small differences between the anisotropic and isotropic sections. Some of the deeper events (below 2000 meters) seem to be a bit stronger, more continuous and better focused on the anisotropic section. The overall difference however is not very pronounced and the interpretation of reflectors would probably be very much the same for both sections.

Comparing the two P-S sections on the other hand illustrates the importance in considering anisotropy when using converted wave data for imaging. Even though the quality of the P-S sections are not as good as the P-P sections we clearly see that the P-S section where anisotropy is being corrected for is of far better quality than the P-S isotropic section. We see that the characteristic event at approximately 1100 meters depth is much better focused and more continuous on the P-S anisotropic section than on the P-S isotropic section. For this event there is also a good correlation between the P-S anisotropic section and the P-P sections. Deeper down in the sections it is harder to correlate the P-S image and the P-P image. What is obvious is that also here there is a clear difference between the P-S anisotropic and the P-S isotropic sections. The anisotropic section have more continuous events than the isotropic one and is therefore more reliable. Also for this deeper part of the section the correlation between the P-S image and the P-P image is better for the anisotropic section. It should be mentioned here that the anisotropic P-S image presented here is probably not the optimal P-S image. We clearly see that the P-S data is very sensitive to the anisotropic models. These models are being refined as we speak and even small changes in these models could improve the P-S image significantly.

Another issue that also needs to be considered when we evaluate these images (both P-P and P-S) is the fact that we are here using 2D data and 2D algorithms to image an 3D earth.

2.4 Conclusions

A prestack migration scheme for converted wave data using space-variant filter (convolutional based) operators has been developed for anisotropic media. The method is valid for TIV and TIH media with arbitrary strength of the anisotropy. Impulse responses demonstrate good dip response and correct kinematic behavior and the synthetic data example illustrates the methods ability to handle complex multi-layer models with a relatively high degree of anisotropy. The real data example shows that the method is applicable to real data and that correcting for anisotropy might be a very important factor when using converted wave data for imaging.

Acknowledgment

We want to thank our colleague Anders Sollid for providing the modeled data for the synthetic data example and Statoil for permission to publish this work. H. K. H. would also like to thank Statoil for financial support.

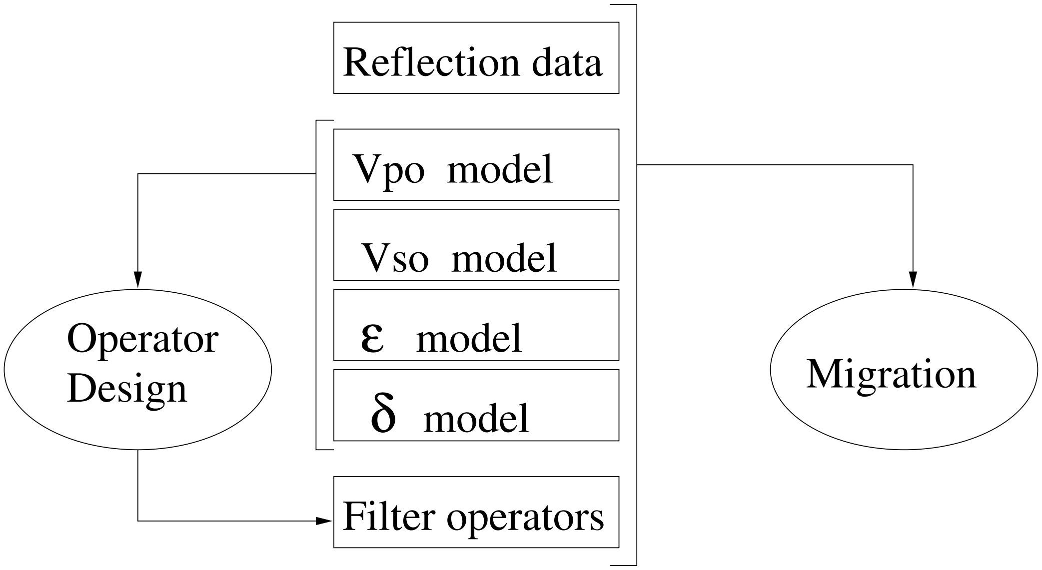

Figure 2.1: The flow of processes involves first a operator design process and then a migration process.

Medium	V_{P0} [m/s]	V_{S0} [m/s]	V_{P0}/V_{S0}	ε	δ
Weak Anisotropic	2000	1000	2.0	0.2	0.1
Strong Anisotropic	2000	1000	2.0	0.4	0.2

Table 2.1: Medium parameters for the weak anisotropic medium and the strong anisotropic medium used in the impulse response examples. The medium parameters are the same for both TIV and TIH examples.

Layer	V_{P0} [m/s]	V_{S0} [m/s]	V_{P0}/V_{S0}	ε	δ
1	1500	400	3.75	0.00	0.00
2	1800-2000	500-550	3.60	0.05	0.02
3	2200	800	2.75	0.22	0.06
4	2850-3000	1250-1350	2.23	0.16	0.08
5	3500	1800	1.94	0.03	0.00
6	3000	1500	2.00	0.12	0.03
7	2500	1250	2.00	0.10	0.00

Table 2.2: Medium parameters for the model used in the synthetic data example. We are here considering TIV symmetry. The layers are numbered from top to bottom and the water-bottom reflection has not been modeled.

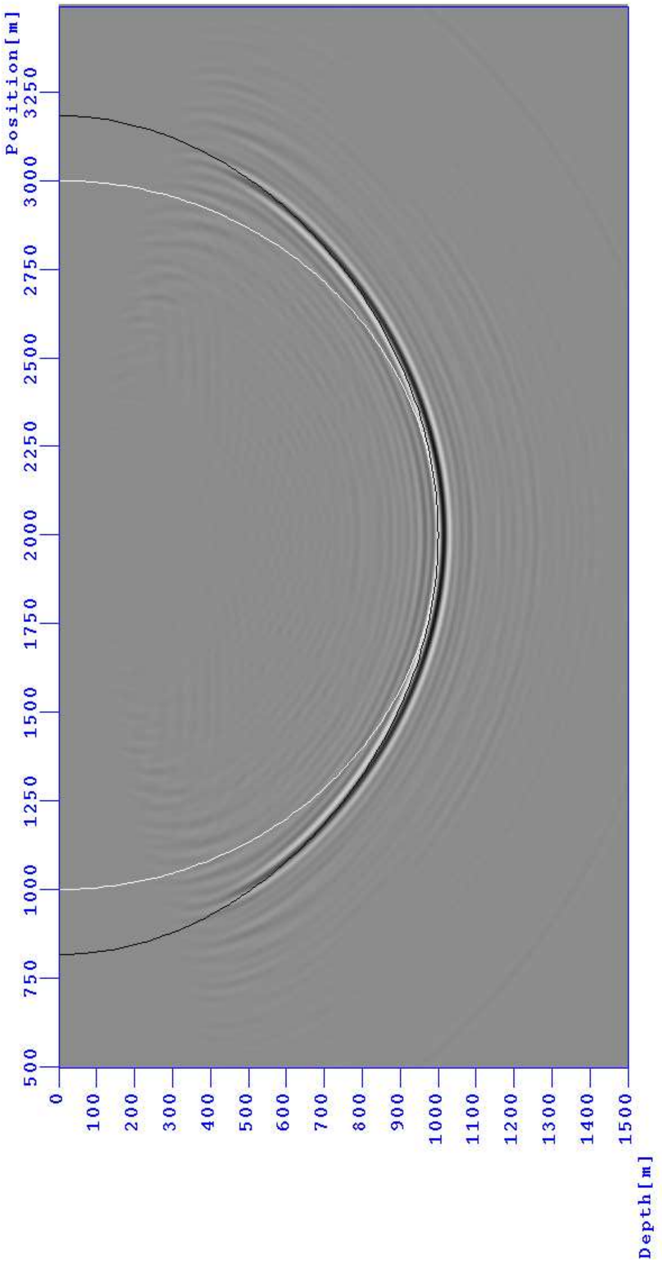

Figure 2.2: P-P Impulse response in weak anisotropic TIV medium. The black and white curves are the correct anisotropic and isotropic depth surfaces, respectively.

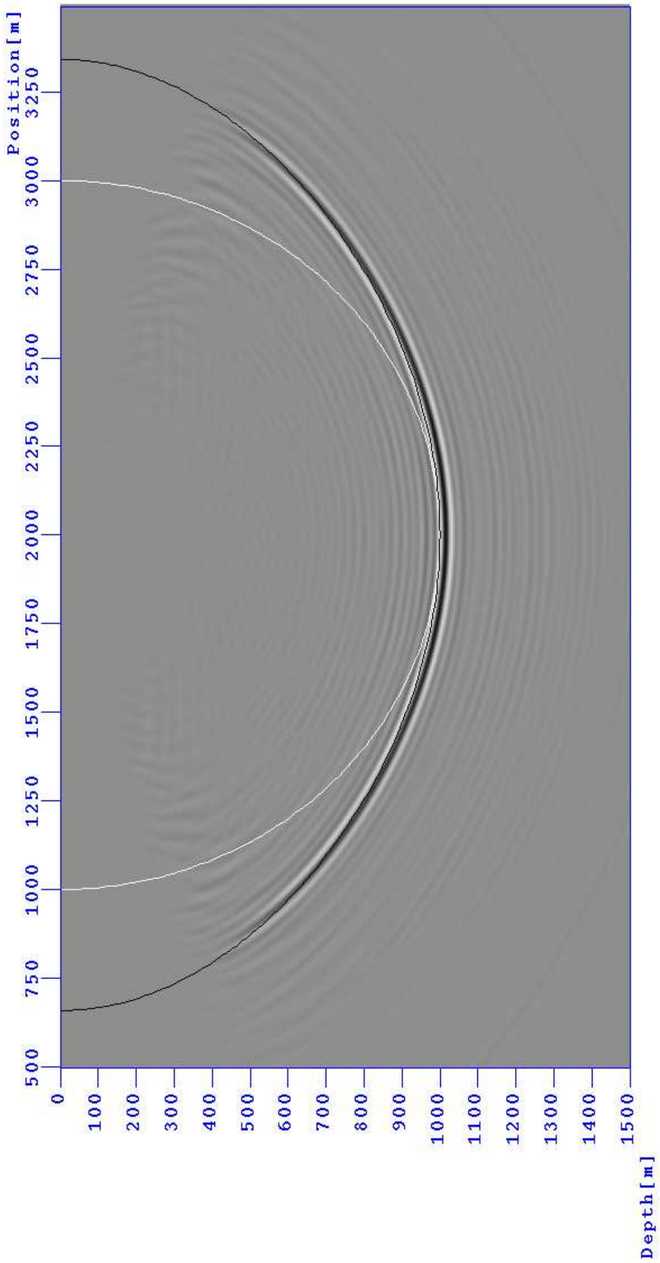

Figure 2.3: P-P Impulse response in strong anisotropic TIV medium. The black and white curves are the correct anisotropic and isotropic depth surfaces, respectively.

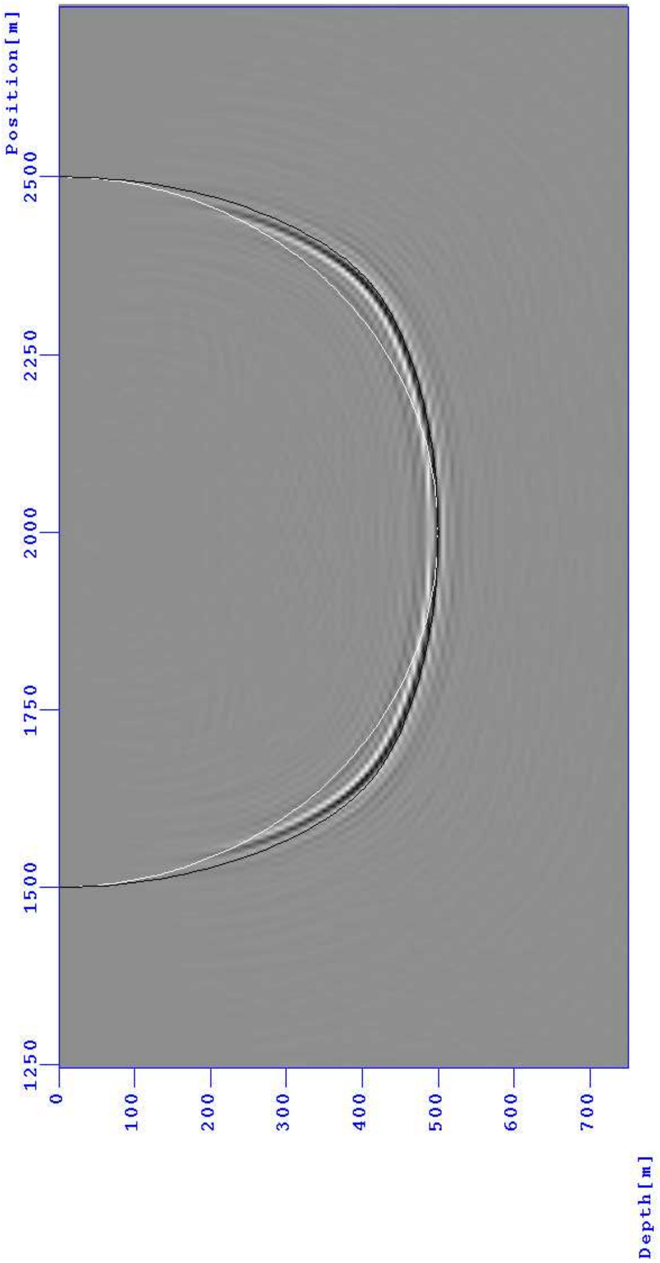

Figure 2.4: S-S Impulse response in weak anisotropic TIV medium. The black and white curves are the correct anisotropic and isotropic depth surfaces, respectively.

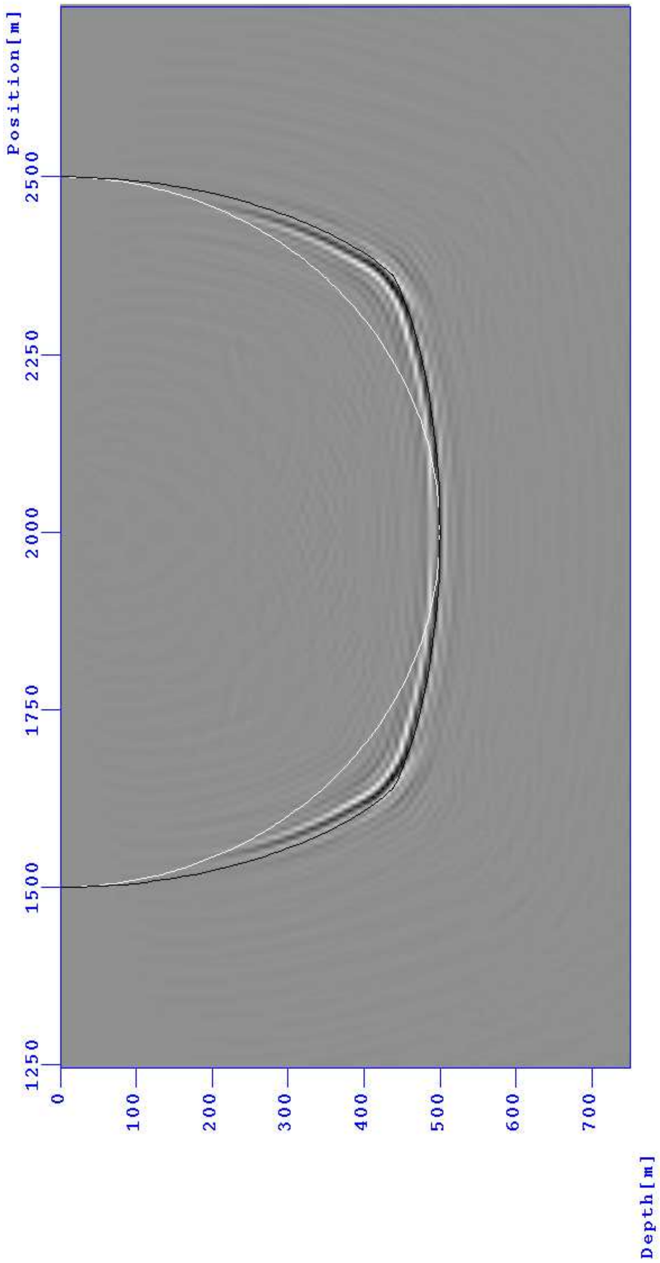

Figure 2.5: S-S Impulse response in strong anisotropic TIV medium. The black and white curves are the correct anisotropic and isotropic depth surfaces, respectively.

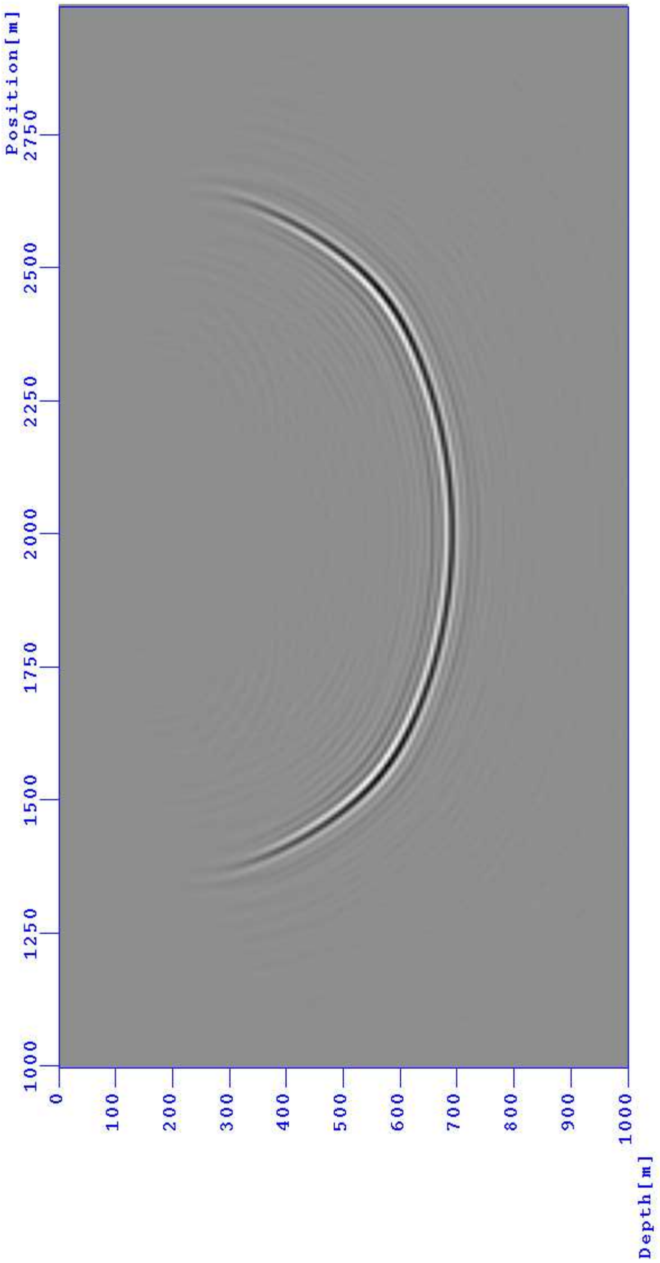

Figure 2.6: P-S Impulse response in weak anisotropic TIV medium.

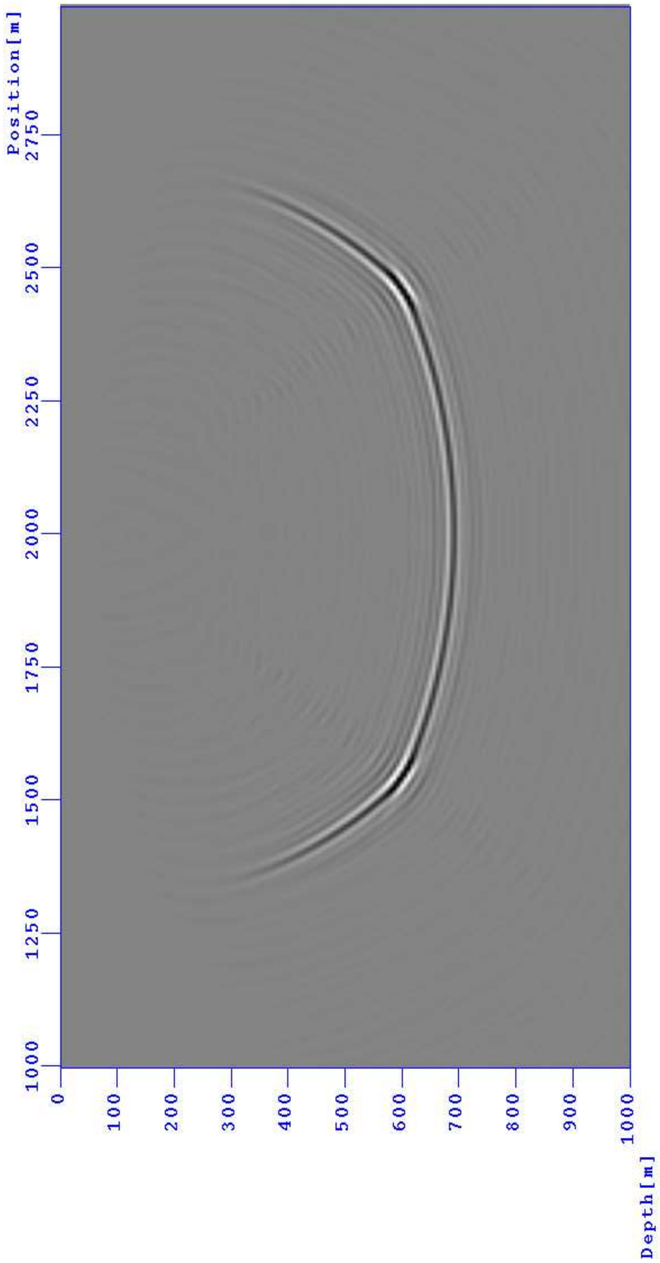

Figure 2.7: P-S Impulse response in strong anisotropic TIV medium.

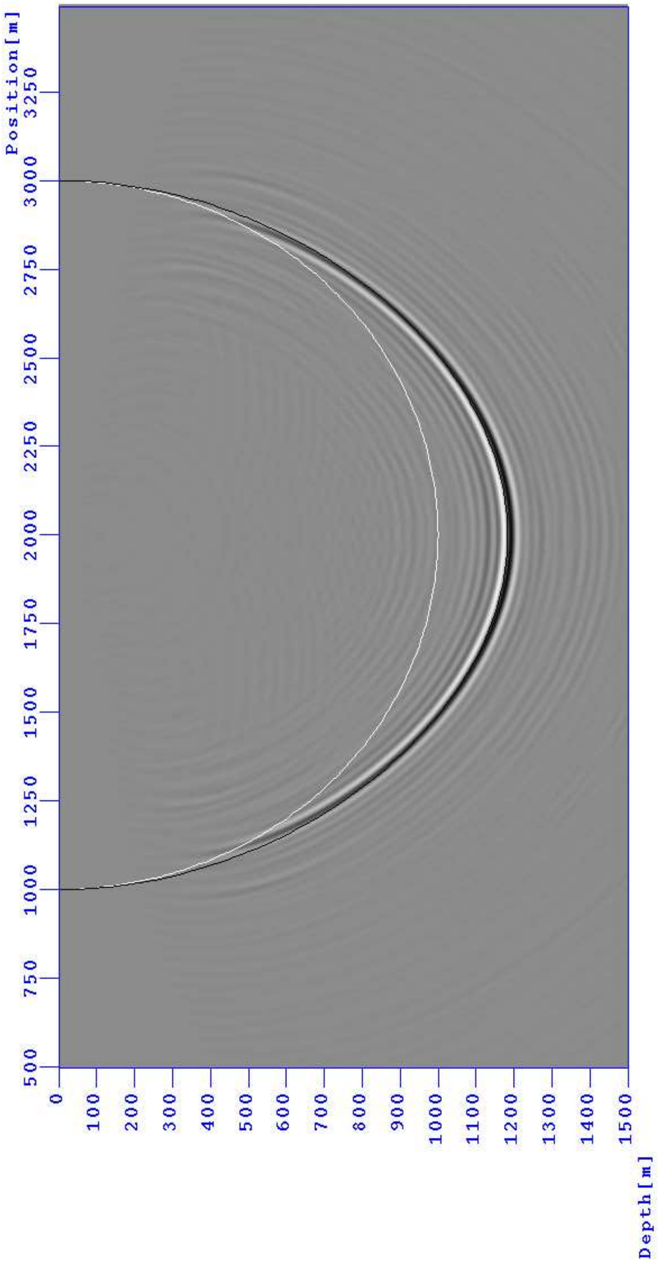

Figure 2.8: P-P Impulse response in weak anisotropic TIH medium. The black and white curves are the correct anisotropic and isotropic depth surfaces, respectively.

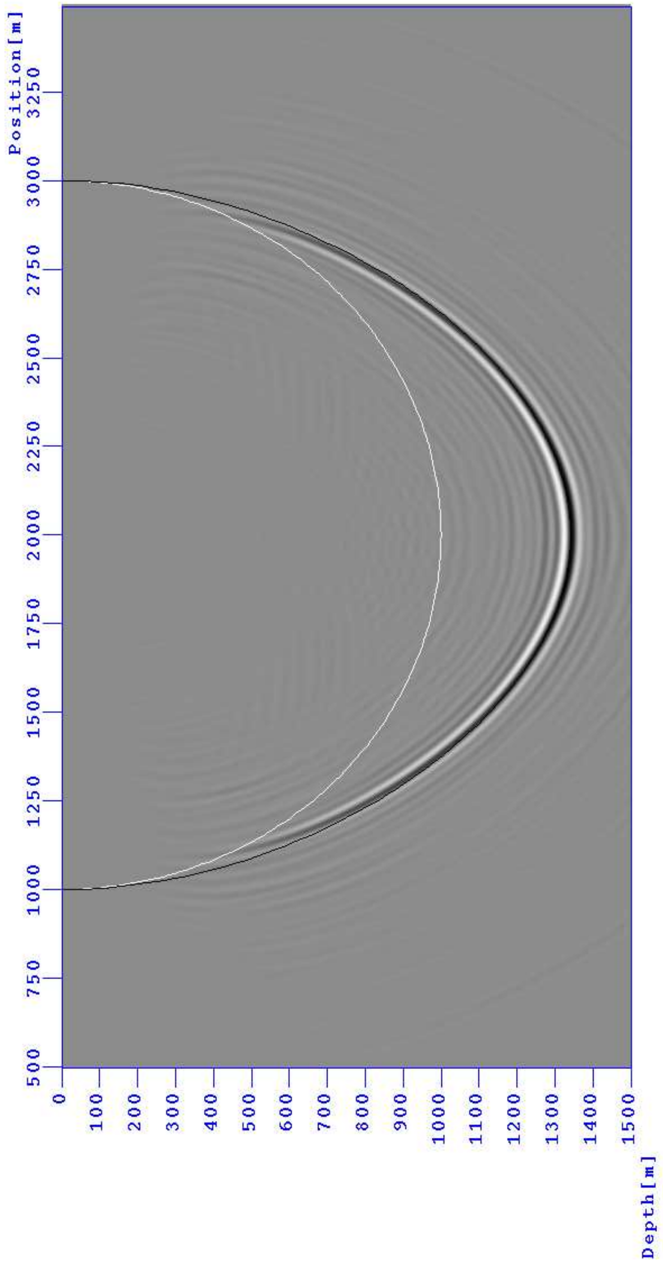

Figure 2.9: P-P Impulse response in strong anisotropic TIH medium. The black and white curves are the correct anisotropic and isotropic depth surfaces, respectively.

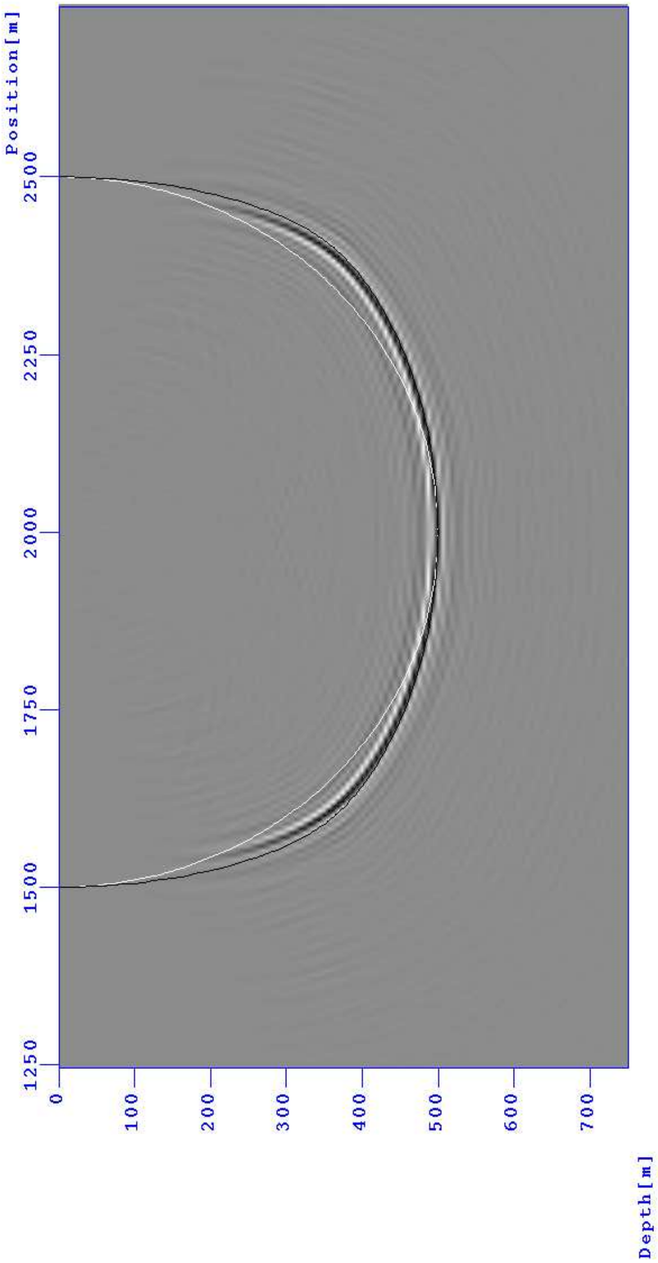

Figure 2.10: S-S Impulse response in weak anisotropic TIH medium. The black and white curves are the correct anisotropic and isotropic depth surfaces, respectively.

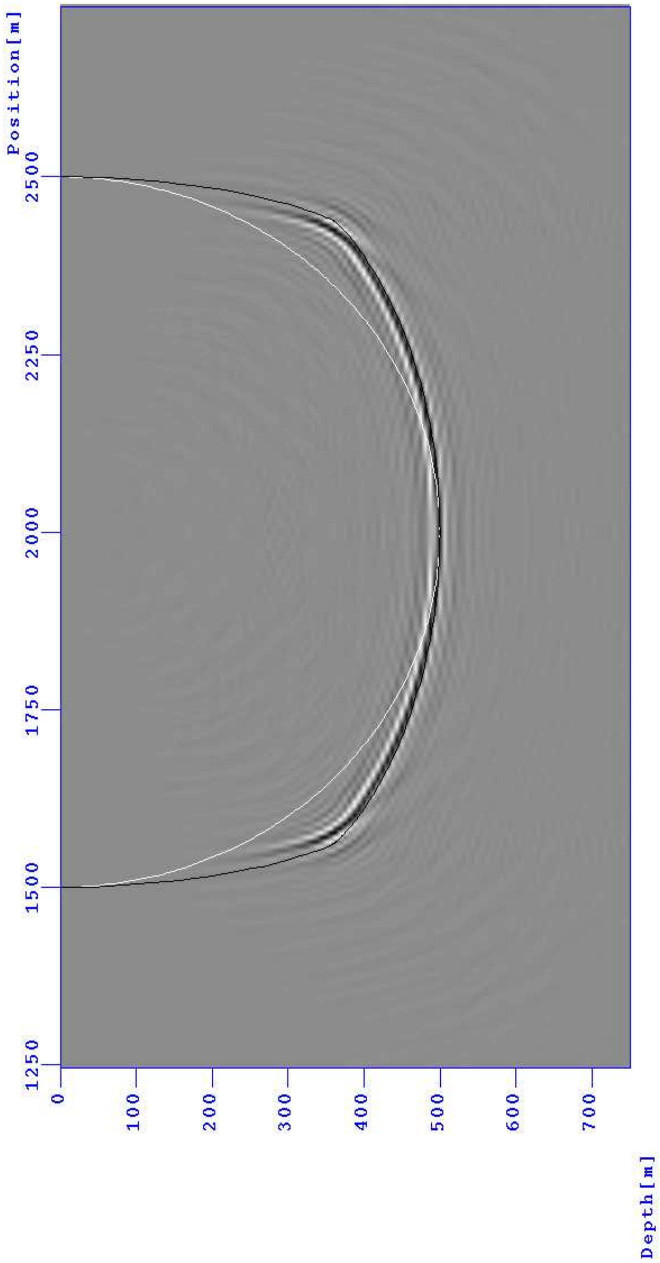

Figure 2.11: S-S Impulse response in strong anisotropic TIH medium. The black and white curves are the correct anisotropic and isotropic depth surfaces, respectively.

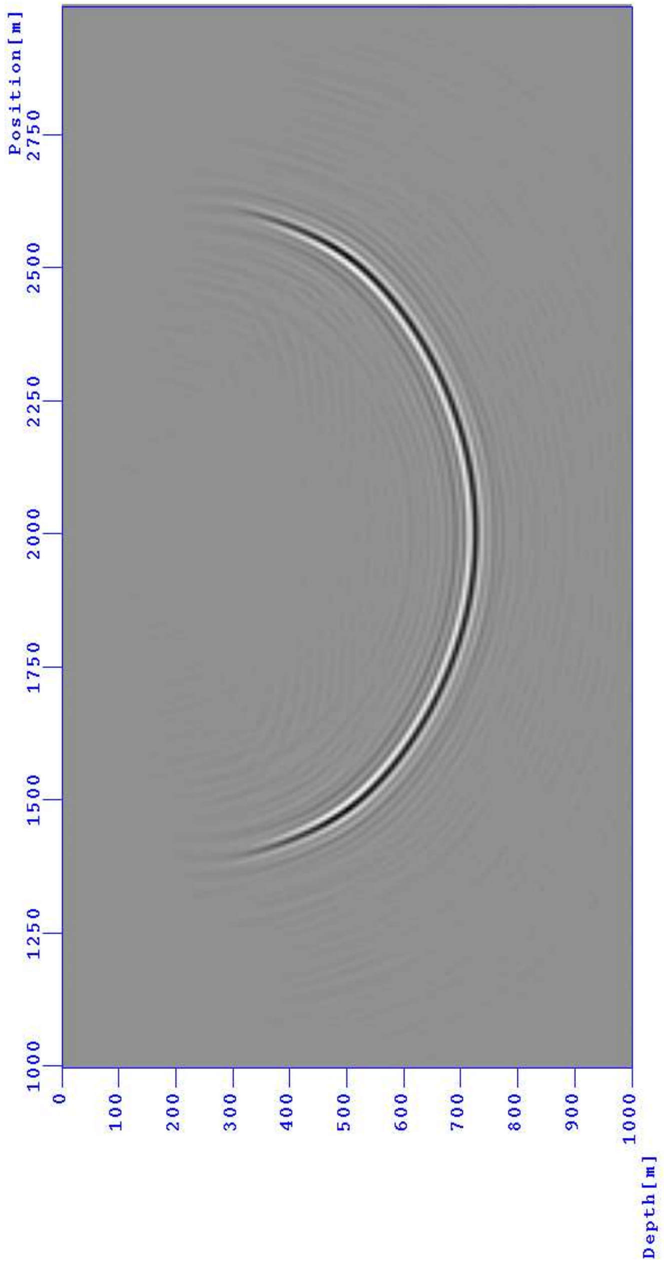

Figure 2.12: P-S Impulse response in weak anisotropic TIH medium.

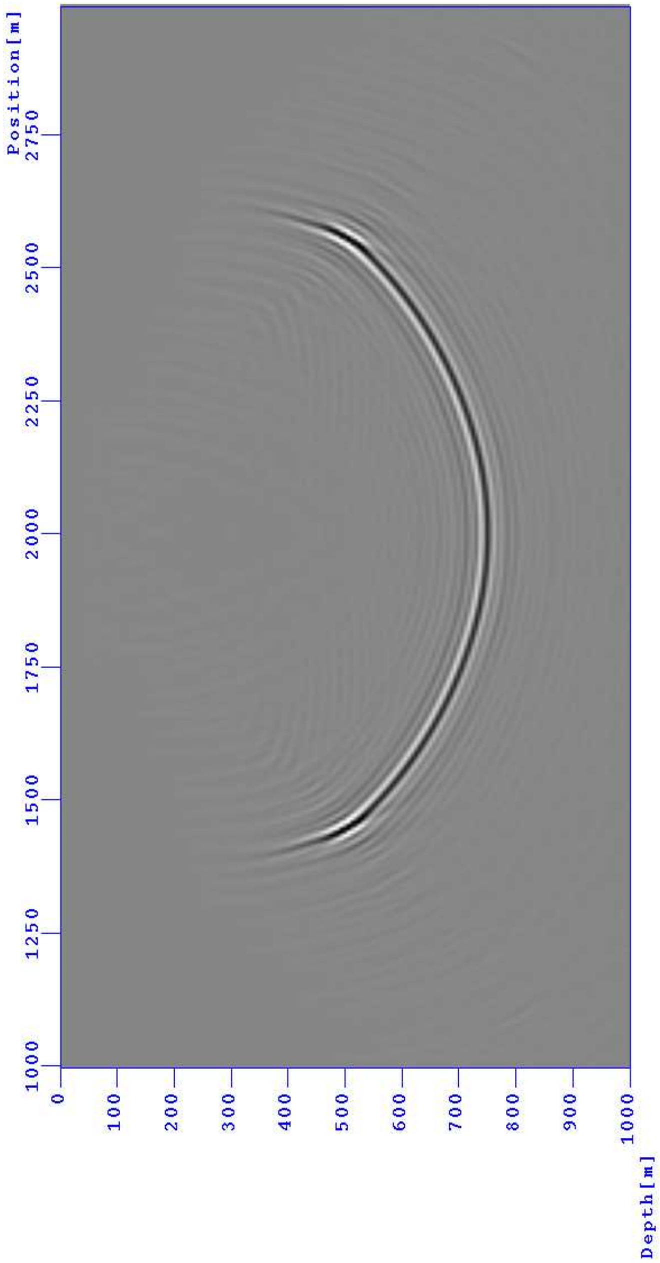

Figure 2.13: P-S Impulse response in strong anisotropic TIH medium.

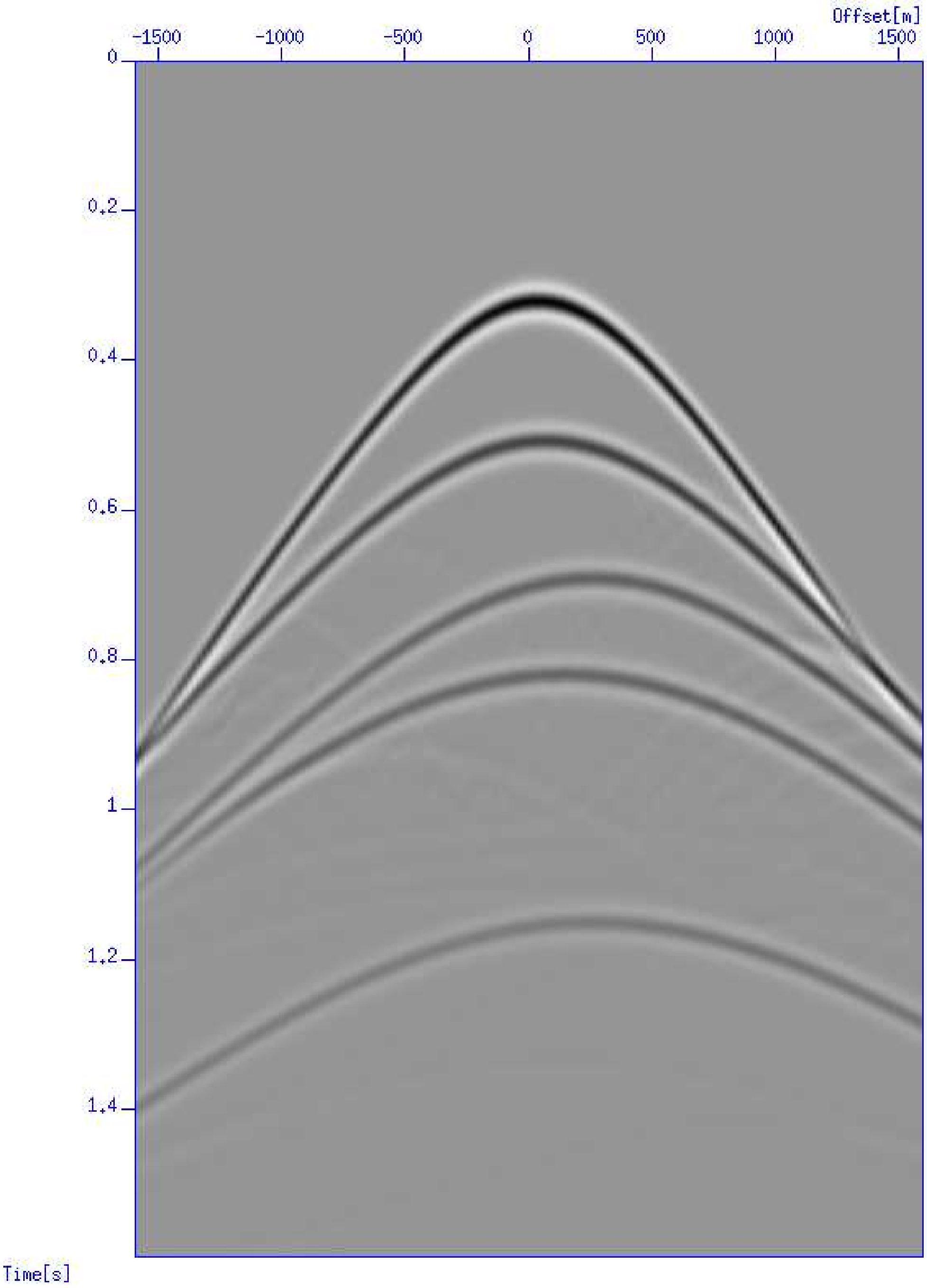

Figure 2.14: A selected P-P shot-gather (at position 1500 meters) which is input to the migration.

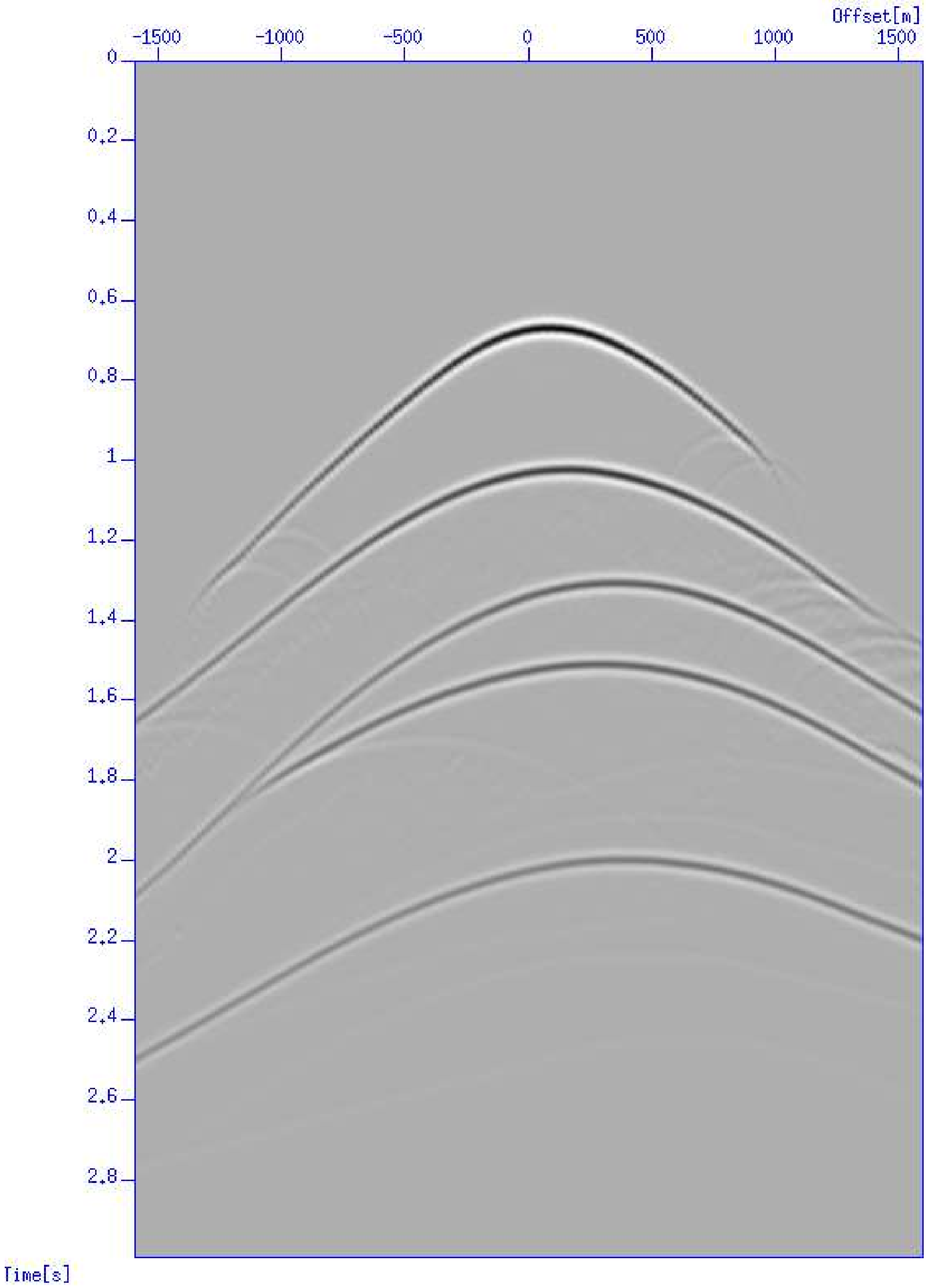

Figure 2.15: A selected P-S shot-gather (at position 1500 meters) which is input to the migration. The sudden cut-off in the first event is due to limitations set in modelling.

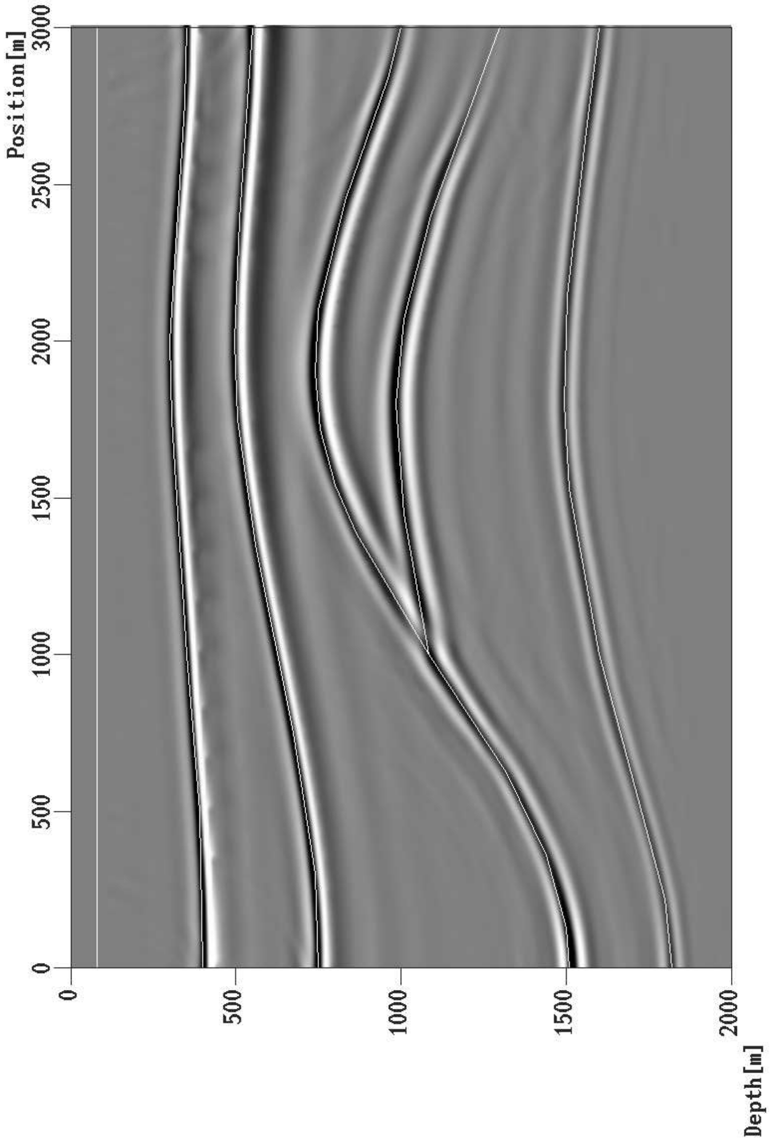

Figure 2.16: P-P image using anisotropic migration. The tiny white curves are the model interfaces. The layers are numbered from the top to bottom.

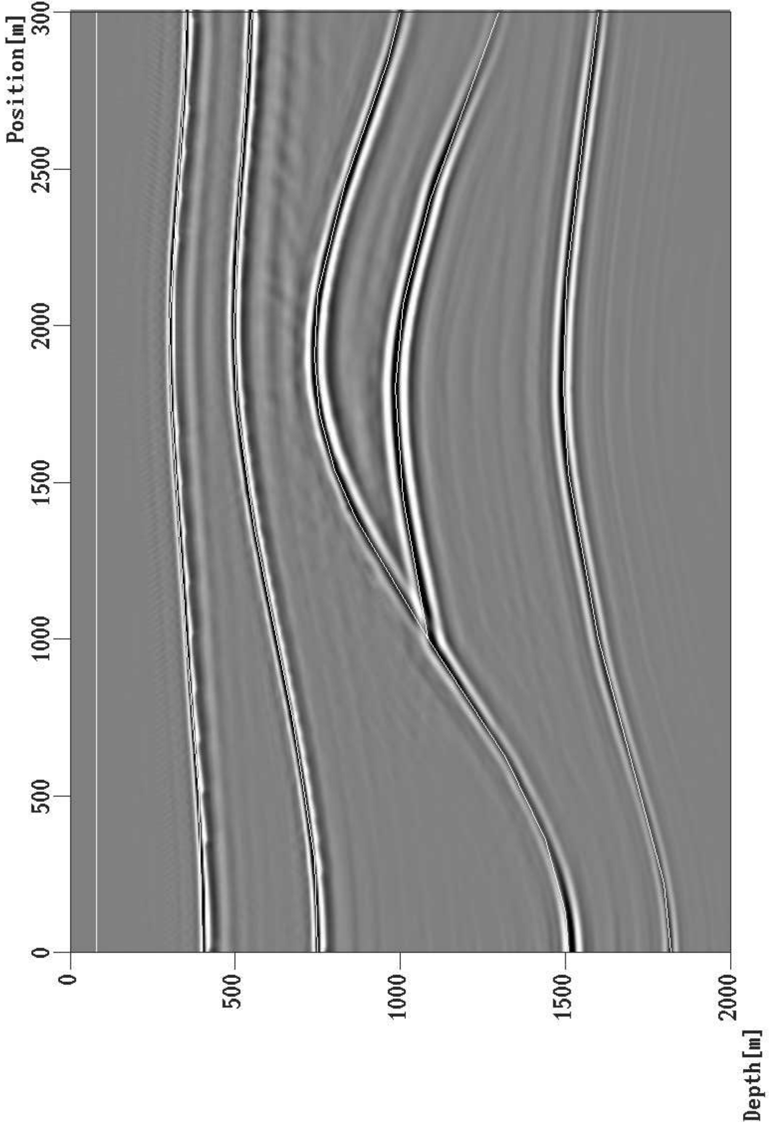

Figure 2.17: P-S image using anisotropic migration. The tiny white curves are the model interfaces. The layers are numbered from the top to bottom.

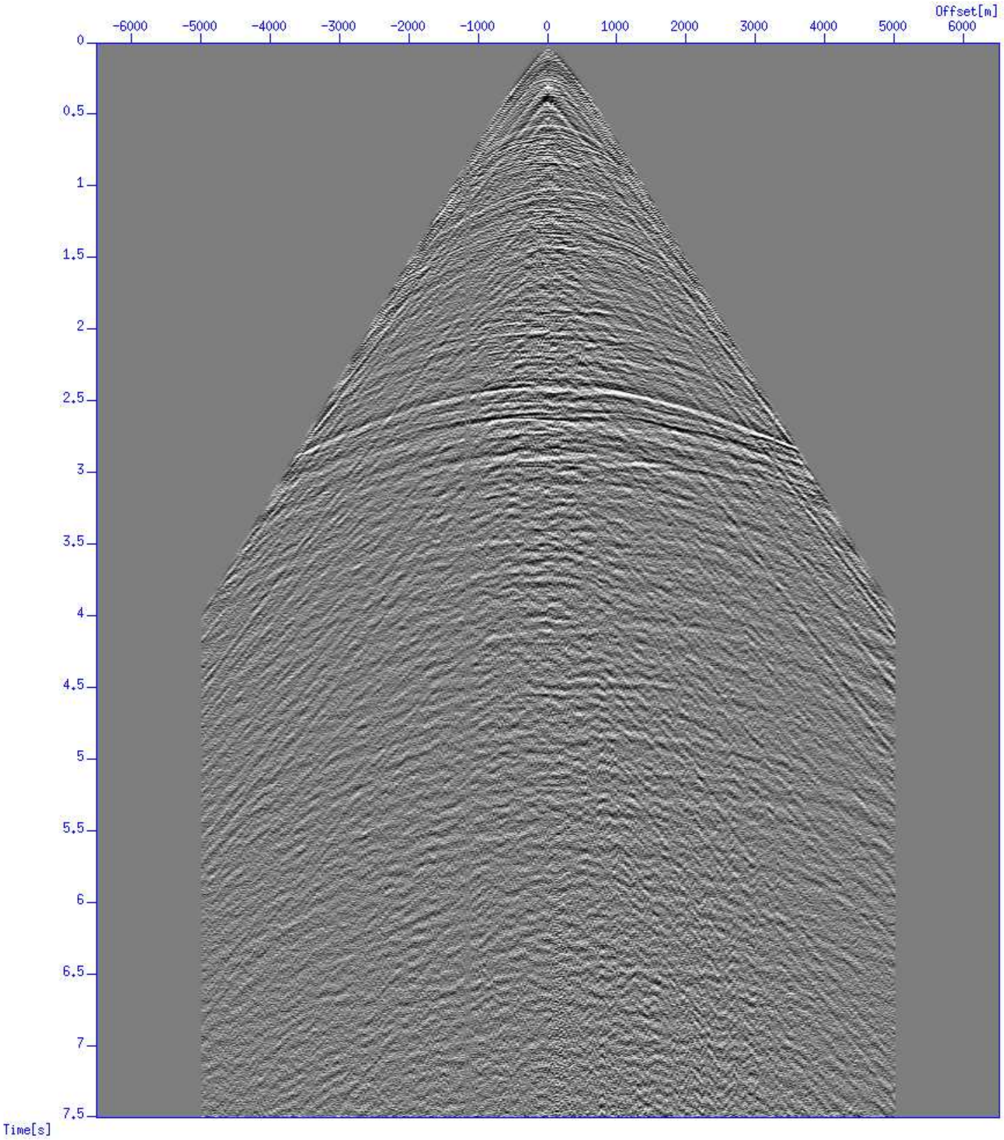

Figure 2.18: A selected P-P receiver-gather (at position 3000 meters) which is input to the migration.

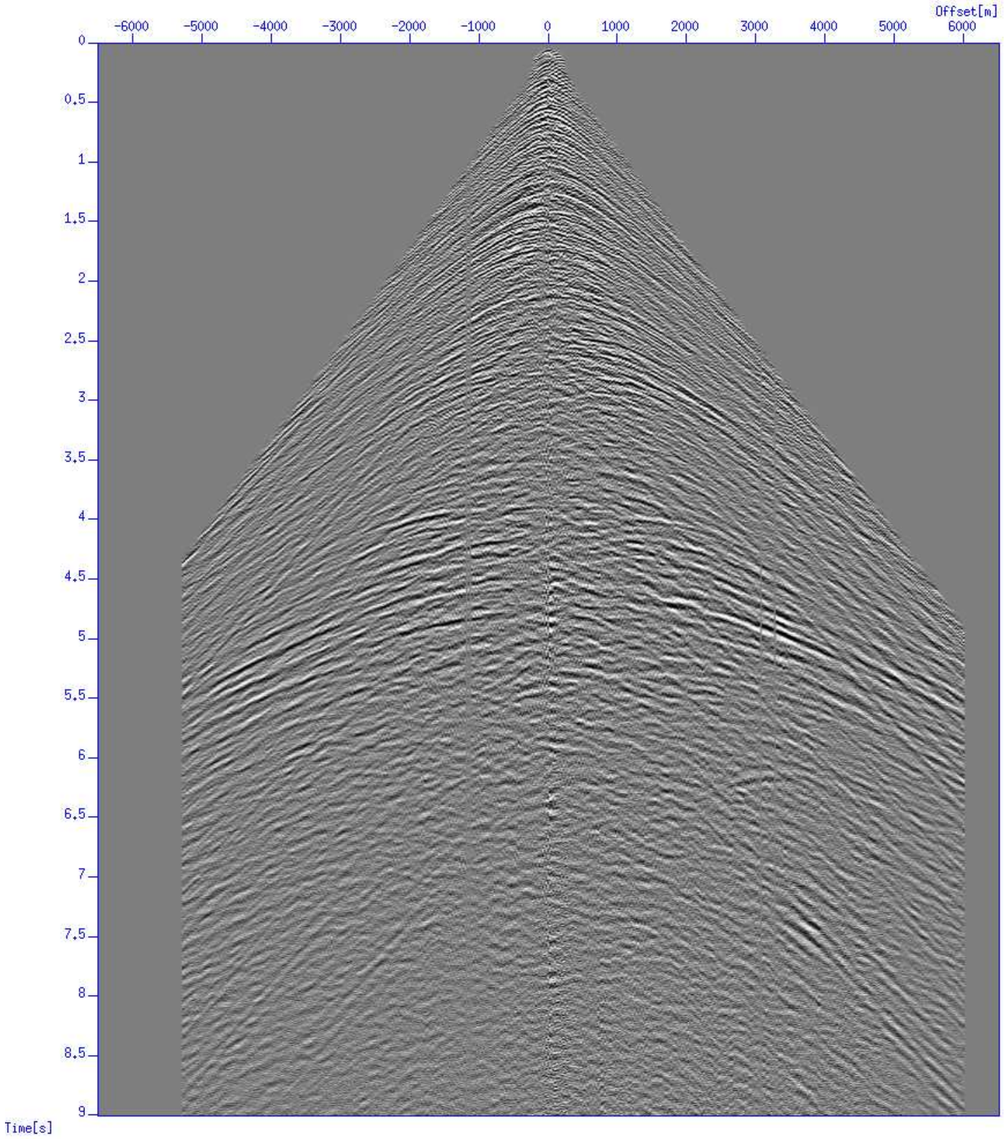

Figure 2.19: A selected P-S receiver-gather (at position 3000 meters) which is input to the migration.

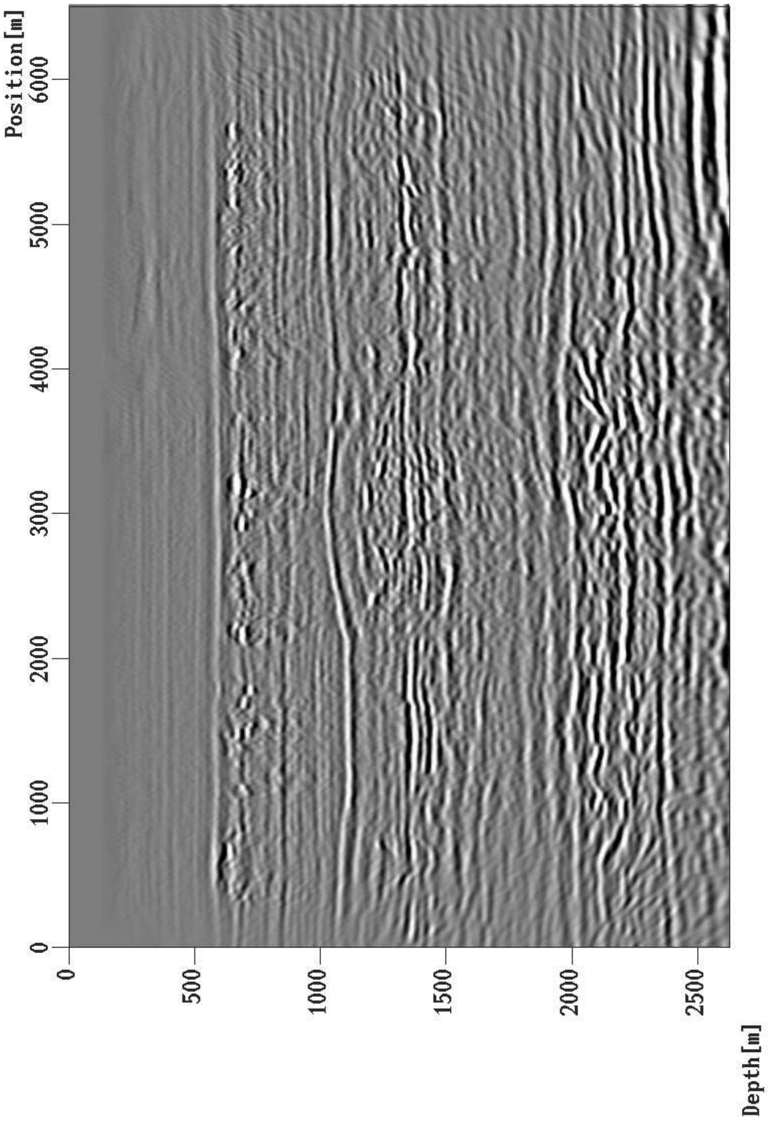

Figure 2.20: Stacked PP section using anisotropic migration.

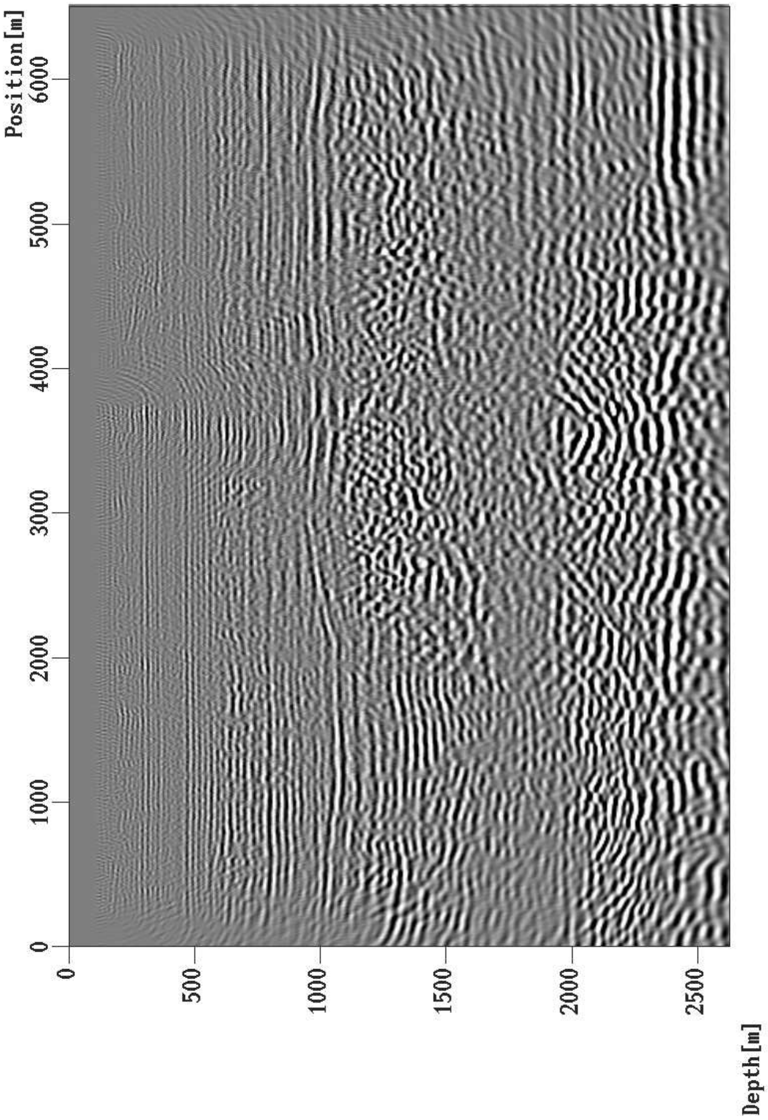

Figure 2.21: Stacked PS section using anisotropic migration.

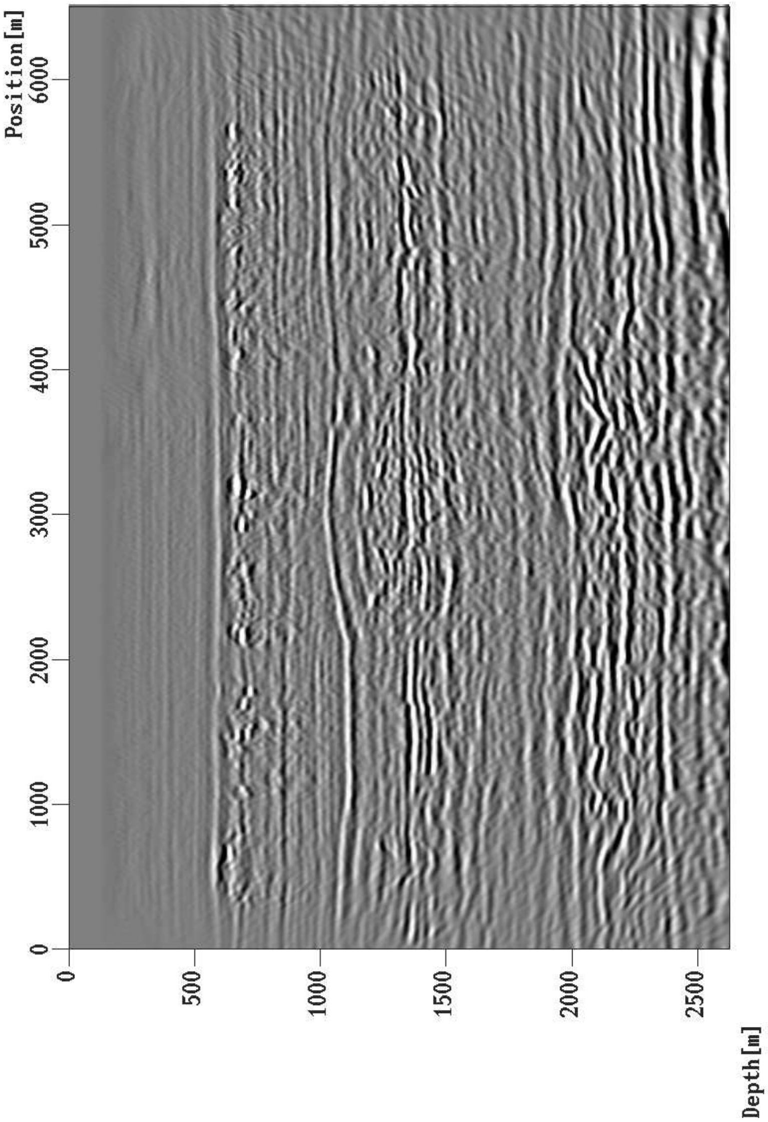

Figure 2.22: Stacked PP section using isotropic migration.

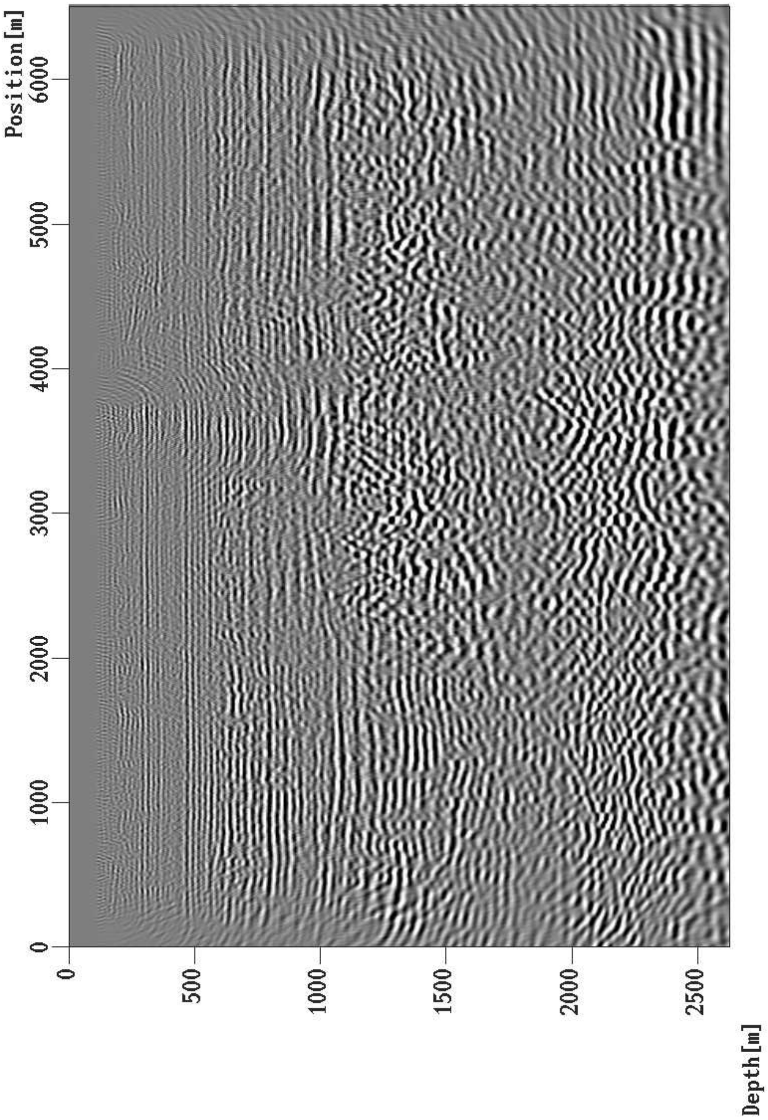

Figure 2.23: Stacked PS section using isotropic migration.

Appendix 2.A

Dispersion equation for P- and S-waves in TI media

This appendix contains the derivation of the dispersion equation for P- and S waves in TI media with an arbitrary symmetry axis. The equations is further simplified considering a vertical symmetry axis or a horizontal symmetry axis to yield dispersions equations for P- and S-waves in TIV media and TIH media, respectively. A similar derivation of the dispersion equation for TI media can be found in Zhang *et al* (2001).

The phase velocities of qP- and qSV-waves for TI media can be expressed exactly in the Thomsen (1986) notation (Tsvankin (1996)) as

$$\begin{aligned}\frac{V^2(\theta,\phi)}{V_{P0}^2} &= 1+\varepsilon\sin^2(\theta-\phi)-\frac{f}{2}\\ &\pm\frac{f}{2}\sqrt{\left(1+\frac{2\varepsilon\sin^2(\theta-\phi)}{f}\right)^2-\frac{2(\varepsilon-\delta)\sin^2 2(\theta-\phi)}{f}},\end{aligned} \qquad \text{(2-A-1)}$$

were ϕ is the angle between the vertical direction and the axis of symmetry. $f = 1 - V_{S0}^2/V_{P0}^2$. V_{P0} and V_{S0} are, respectively, the qP- and the qSV-wave velocities in the direction parallel to the symmetry axis, ε and δ are the Thomsen (1986) parameters describing anisotropy, here defined in a coordinate system rotated through the angle ϕ.

For plane waves propagating in the vertical x, z-plane, the phase angle is given by

$$\sin(\theta)=\frac{V(\theta,\phi)k_x}{\omega} \quad , \qquad \cos(\theta)=\frac{V(\theta,\phi)k_z}{\omega}. \qquad \text{(2-A-2)}$$

By rewriting equation (2-A-1) as

$$\begin{aligned}&\left[\frac{V^2(\theta,\phi)}{V_{P0}^2}-\left(1-\frac{f}{2}\right)(\sin^2\theta+\cos^2\theta)-\varepsilon\sin^2(\theta-\phi)\right]^2 =\\ &\frac{f^2}{4}\left[\left(\sin^2\theta+\cos^2\theta+\frac{2\varepsilon\sin^2(\theta-\phi)}{f}\right)^2-\frac{2(\varepsilon-\delta)\sin^2 2(\theta-\phi)}{f}\right]\end{aligned} \qquad \text{(2-A-3)}$$

and then using equation (2-A-2) and substituting for θ yields a dispersion equation for TI media.

The dispersion equation for TI media is quartic and is expressed as

$$k_4^4 + a_3 k_z^3 + a_2 k_z^2 + a_1 k_z + a_0 = 0 \tag{2-A-4}$$

where
$a_3 = [f(\varepsilon - \delta)\sin 4\phi + 2\varepsilon(1-f)\sin 2\phi]k_x/a_4$
$a_4 = f - 1 + 2\varepsilon(f-1)\sin^2\phi - \frac{f}{2}(\varepsilon - \delta)\sin^2 2\phi$
$a_2 = [b_2 k_x^2 + (\frac{\omega}{V_{P0}})^2(2 + 2\varepsilon\sin^2\phi - f)]/a_4$
$b_2 = f(\varepsilon - \delta)\sin^2 2\phi - 2(1-f)(1+\varepsilon) - 2f(\varepsilon - \delta)\cos^2 2\phi$
$a_1 = [b_1 k_x^3 - 2\varepsilon\sin 2\phi(\frac{\omega}{VP0})^2 k_x]/a_4$
$b_1 = 2\varepsilon(1-f)\sin 2\phi - f(\varepsilon - \delta)\sin 4\phi$
$a_0 = b_0/a_4$
$b_0 = (2 + 2\varepsilon\cos^2\phi - f)(\frac{\omega}{V_{P0}})^2 k_x^2 - (\frac{\omega}{V_{P0}})^4 -$
$[(1-f)(1 + 2\varepsilon\cos^2\phi) + \frac{f}{2}(\varepsilon - \delta)\sin^2 2\phi]k_x^4$

The analytical solutions of (2-A-4) can be obtained by separating the quartic equation into two quadratic equations :

$$k_z^2 + \left(a_3/2 + \sqrt{a_3^2/4 + R - a_2}\right)k_z + R/2 \pm \sqrt{R^2/4 - a_0} = 0 \tag{2-A-5}$$

$$k_z^2 + \left(a_3/2 - \sqrt{a_3^2/4 + R - a_2}\right)k_z + R/2 \mp \sqrt{R^2/4 - a_0} = 0 \tag{2-A-6}$$

where R is a real root of the cubic equation,

$$R^3 - a_2R^2 + (a_1a_3 - 4a_0)R - (a_1^2 + a_0a_3^2 - 4a_0a_2) = 0 \tag{2-A-7}$$

and should give real coefficients in the quadratic equations (2-A-5) and (2-A-6) and satisfy

$$a_3R/2 - a_1 \mp \sqrt{(a_3^2/4 + R - a_2)(R^2/4 - a_0)} = 0 \tag{2-A-8}$$

The three roots of (2-A-7) are given as follows
Let

$$s_1 = [r + (q^3 + r^2)^{\frac{1}{2}}]^{\frac{1}{3}}$$

$$s_2 = [r - (q^3 + r^2)^{\frac{1}{2}}]^{\frac{1}{3}}$$

where

$$q = \frac{1}{3}a_1 a_3 - \frac{1}{9}a_2^2 - \frac{4}{3}a_0$$

$$r = \frac{1}{27}a_2^3 + \frac{1}{2}a_1^2 + \frac{1}{2}a_0 a_3^2 - \frac{4}{3}a_0 a_2 - \frac{1}{6}a_1 a_2 a_3$$

Then

$$R_1 = (s_1 + s_2) + \frac{a_2}{3}, \tag{2-A-9}$$

$$R_2 = -\frac{1}{2}(s_1 + s_2) + \frac{a_2}{3} + \frac{i\sqrt{3}}{2}(s_1 - s_2), \tag{2-A-10}$$

$$R_3 = -\frac{1}{2}(s_1 + s_2) + \frac{a_2}{3} - \frac{i\sqrt{3}}{2}(s_1 - s_2). \tag{2-A-11}$$

When the negative sign makes (2-A-8) valid, the signs in (2-A-5) and (2-A-6) should be, respectively, + and −, otherwise the signs should be − and +. The four roots of (2-A-5) and (2-A-6) are the roots of the quartic equation (2-A-4). The four roots of the quartic dispersion equation are related to the downgoing and upgoing qP-waves and the downgoing and upgoing qSV-waves, respectively.

Considering the vertical axis as the axis of symmetry as for TIV media ($\phi = 0$) the above coefficients become

$a_3 = 0$

$a_2 = [-2(1+\varepsilon-f-f\delta)k_x^2 + (\frac{\omega}{V_{P0}})^2(2-f)]/(f-1)$

$a_1 = 0$

$a_0 = [(2+2\varepsilon-f)(\frac{\omega}{V_{P0}})^2 k_x^2 - (\frac{\omega}{V_{P0}})^4 - (1-f)(1+2\varepsilon)k_x^4]/(f-1)$

The dispersion equation for TIV media then becomes

$$k_z^4 + a_2 k_z^2 + a_0 = 0 \tag{2-A-12}$$

with solution

$$k_z = \pm\sqrt{\frac{-a_2 \pm \sqrt{a_2^2 - 4a_0}}{2}}, \tag{2-A-13}$$

where ± in front of the square-root is related to down- or up-going waves and the ± inside the square-root is related to qP- or qSV-waves, respectively.

Considering the horizontal axis as the axis of symmetry as for TIH media ($\phi = 90$) we will get a similar dispersion equation as given by (2-A-13). The coefficients a_2 and a_0 are now given by (a_3 and a_1 still become zero)

$a_2 = [-2(1+\varepsilon-f-f\delta)k_x^2 + (\frac{\omega}{V_{P0}})^2(2+2\varepsilon-f)]/(f-1)(1+2\varepsilon)$

$a_0 = [(2-f)(\frac{\omega}{V_{P0}})^2 k_x^2 - (\frac{\omega}{V_{P0}})^4 - (1-f)k_x^4]/(f-1)(1+2\varepsilon)$

In the main text of this paper the coefficient a_2 is named a_{TIV} for TIV media and a_{TIH} for TIH media. The coefficient a_0 is named b_{TIV} for TIV media and b_{TIH} for TIH media.

Appendix 2.B
The filter design problem

This appendix contains the formulation of the numerical optimization problem of finding the filter coefficients that approximates the exact phase-shift operator in the frequency-wavenumber domain. The exact phase shift operator in equation (2.1) alters the phase of a plane wave component by $k_z \Delta z$ and does not change the amplitude. We wish to approximate the desired phase shift by some operator $w(k_\omega, x)$ with spatial frequency response $W(k_\omega, k_x)$.

k_ω is here the frequency-velocity ratio ω/V_{P0}. We have here for notational convenience omitted the ϵ, δ and V_{P0}/V_{S0} dependence of the operator as these are constant for each media type (defined by one set of ϵ, δ and V_{P0}/V_{S0} values) considered.

By series expansion the exact phase shift operator in equation (2.1) can be expressed as

$$\exp[ik_z\Delta z] = \sum_{n=0}^{\infty} \frac{(ik_z\Delta z)^n}{n!} = \sum_{n=0}^{\infty} \frac{(ik_\omega \Delta z)^n (k_z/k_\omega)^n}{n!}, \tag{2-B-1}$$

with

$$k_z/k_\omega = 1 - (k_x/k_\omega)^2/2 - (k_x/k_\omega)^4/8 - (k_x/k_\omega)^6/16 - ..., \tag{2-B-2}$$

where $k_\omega = \omega/V_{P0}$. Collecting terms up to order N the phase shift operator in equation (2.1) can be expressed as

$$\exp[ik_z\Delta z] = \sum_{n=0}^{N} \gamma_n k_x^{2n}, \tag{2-B-3}$$

where the coefficients γ are functions of the temporal frequency and the velocity (V_{PO}). An inverse Fourier transform with respect to k_x of equation (2.1) using (2-B-3) now gives

$$P(\omega, x, z + \Delta z) = \sum_{n=0}^{N} (-1)^n \gamma_n (\partial^{2n}/\partial x^{2n}) P(\omega, x, z). \tag{2-B-4}$$

Approximation of the spatial derivatives in equation (2-B-4) by FIR (Finite Impulse Response) operators yields

$$\partial^{2n} P/\partial x^{2n} = \sum_{m=0}^{M} d_{m,n}[P(x + m\Delta x) + P(x - m\Delta x)]. \tag{2-B-5}$$

Inserting (2-B-5) in (2-B-4) and truncating we obtain

$$P(\omega, x, z + \Delta z) = \sum_{l=0}^{L} w_l [P(\omega, x + l\Delta x, z) + P(\omega, x - l\Delta x, z)]. \tag{2-B-6}$$

Downward wavefield extrapolation can then be expressed as a space-variant convolution in the frequency-space domain.

The equation for downward extrapolation can then be written in the $\omega - k_x$ domain as

$$\begin{aligned} P(\omega, k_x, z+\Delta z) &= W(k_\omega, k_x) P(\omega, k_x, z) \\ &= (1+\Omega)\exp\left[i(k_z \Delta z + \xi)\right] P(\omega, k_x, z) \end{aligned} \tag{2-B-7}$$

where

$$W(k_\omega, k_x) = \sum_{l=0}^{L} 2Re(w_l)\cos(k_x l \Delta x) + i\sum_{l=0}^{L} 2Im(w_l)\cos(k_x l \Delta x) \tag{2-B-8}$$

is obtained by a spatial Fourier transform of the operator w in equation (2-B-6).

$$\Omega = \Omega(k_\omega, k_x) = |W| - 1 \tag{2-B-9}$$

is the amplitude error and

$$\xi = \xi(k_\omega, k_x) = k_z \Delta z - \tan^{-1}[Im(W)/Re(W)] \tag{2-B-10}$$

is the phase error introduced in each computational step.

A detailed analysis of the effects of the amplitude error $\Omega(k_\omega, k_x)$ and phase error $\xi(k_\omega, k_x)$ in equation (2-B-7) is beyond the scope of this work. Here we are interested in a sensible criterion for the design of the wavefield extrapolators. We therefore simply state that by considering small phase and amplitude errors that are independent of each other and independent of depth, that there is no coupling between the k_ω and k_x dependency for both amplitude error and phase error and that the ω-derivatives can be approximated by first-order finite differences, we can construct a sensible design criterion for the wavefield extrapolators.

The design criterion for the wave propagator is to minimize the phase and amplitude errors and their gradients for a range of propagation-angles. To ensure stability, this optimization is constrained such that the evanescent energy and waves propagating at higher angles than a chosen maximum design angle are damped in the recursive downward extrapolation process.

The optimization problem can be summarized as follows:
For $k_\omega = 0, ..., k_{\omega,max}$ find $w_l(k_\omega)$ $, l = 0, ..., L$ such that the error

function given by

$$E(W|k_\omega) = \tag{2-B-11}$$
$$\sum_{0}^{k_{x,max}} \left[(\Omega)^2 + (\xi)^2 + s\left((\partial\Omega/\partial k_\omega)^2 + (\partial\Omega/\partial k_x)^2 + (\partial\xi/\partial k_\omega)^2 + (\partial\xi/\partial k_x)^2\right)\right]^2$$

with the constrain that

$$|W| < 1 \qquad for \qquad k_{xmax} < k_x < \pi/\Delta x \tag{2-B-12}$$

is minimum. Here is $k_{\omega,max}$ the highest k_ω ratio of interest and $k_{x,max} = k_{\omega,max} \times sin\theta_{max}$ where θ_{max} is the maximum design angle. The factor s in equation (2-B-12) allows us to balance the weight put on the amplitude and phase errors relative to their derivatives. The constrain (2-B-12) was incorporated into the least-squares problem (2-B-12) by adding to the error function in (2-B-12) a penalty function which grows large whenever the magnitude of the operator response exceeds unity.

For the minimization of the resulting error function we have used a Levenberg-Marquardt search algorithm which generally guarantees global convergence, even for starting points far from the solution.

Appendix 2.C
The coordinates for the overlay-functions

This appendix contains the derivation of the coordinates for the overlay-functions to the impulse responses in TIV media and TIH media. The derivation is based on the relationship between the phase velocity $V(\theta)$ and the group velocity $v(\psi)$, the phase angle θ and the group angle ψ.

The coordinates for the overlay-functions are given by

$$x = r\sin(\psi) \qquad z = r\cos(\psi) \tag{2-C-1}$$

where $r = v(\psi)t$ is the radius. $v(\psi)$ is the group velocity and t is the one-way travel-time for the wave in consideration. In order to calculate the coordinates for the P-P and S-S impulse responses we need to find proper expressions for the group velocity $v(\psi)$ and the group angle ψ expressed through the phase velocity $V(\theta)$ and the phase angle θ.

The relationship between group velocity and phase velocity for a medium without attenuation is given by (Berryman(1979))

$$v^2(\psi) = V^2(\theta) + \left(\frac{dV}{d\theta}\right)^2 \tag{2-C-2}$$

and the relationship between group angle ψ and phase angle θ is given by (Thomsen (1986))

$$\tan(\psi) = \frac{\left(\tan(\theta) + \frac{1}{V}\frac{dV}{d\theta}\right)}{\left(1 - \frac{\tan(\theta)}{V}\frac{dV}{d\theta}\right)}. \tag{2-C-3}$$

For TI media with a vertical axis of symmetry (TIV) can the phase velocities of qP- and qSV-waves be expressed exactly in the Thomsen (1986) notation (Tsvankin 1996) as

$$V^2_{\text{TIV}}(\theta) = V^2_{P0}\left[1 + \varepsilon\sin^2(\theta) - \frac{f}{2} \pm \frac{f}{2}D\right], \tag{2-C-4}$$

were

$$D = \sqrt{\left(1 + \frac{2\varepsilon\sin^2(\theta)}{f}\right)^2 - \frac{2(\varepsilon-\delta)\sin^2(2\theta)}{f}}$$

and $f = 1 - V^2_{S0}/V^2_{P0}$. V_{P0} and V_{S0} are, respectively, the qP- and the qSV-wave velocities in the vertical direction, ε and δ are the Thomsen (1986) parameters describing anisotropy. The ± in front of the square-root gives the qP and qSV phase velocity, respectively.

By carrying out the derivation of the above we obtain

$$\frac{dV_{\text{TIV}}}{d\theta} = \frac{V^2_{P0}}{2V_{\text{TIV}}}\left[2\epsilon\sin(\theta)\cos(\theta) \pm \frac{f}{2}D'\right], \tag{2-C-5}$$

where

$$D' = \frac{1}{2D}\left[\left(1 + \frac{2\epsilon\sin^2(\theta)}{f}\right)\left(\frac{8\epsilon\sin(\theta)\cos(\theta)}{f}\right) - \frac{8(\epsilon-\delta)\sin(2\theta)\cos(2\theta)}{f}\right].$$

The expressions for the phase velocity in TIV media and its derivative (equation (2-C-4) and (2-C-5)) can the be inserted into equation (2-C-2) to yield the group velocity for TIV media.

For TI media with a horizontal axis of symmetry (TIH) can the phase velocities of qP- and qSV-waves be expressed exactly in the Thomsen (1986) notation (Tsvankin 1996) as

$$V^2_{\text{TIH}}(\theta) = V^2_{P0}\left[1 + \varepsilon\cos^2(\theta) - \frac{f}{2} \pm \frac{f}{2}\hat{D}\right], \tag{2-C-6}$$

were

$$\hat{D} = \sqrt{\left(1 + \frac{2\varepsilon\cos^2(\theta)}{f}\right)^2 - \frac{2(\varepsilon-\delta)\sin^2(2\theta)}{f}}.$$

The ± in front of the square-root gives the qP and qSV phase velocity, respectively.

By carrying out the derivation of the above we obtain

$$\frac{dV_{\text{TIH}}}{d\theta} = \frac{V^2_{P0}}{2V_{\text{TIH}}}\left[-2\epsilon\sin(\theta)\cos(\theta) \pm \frac{f}{2}\hat{D}'\right], \tag{2-C-7}$$

where

$$\hat{D}' = \frac{1}{2\hat{D}}\left[-\left(1 + \frac{2\epsilon\cos^2(\theta)}{f}\right)\left(\frac{8\epsilon\sin(\theta)\cos(\theta)}{f}\right) - \frac{8(\epsilon-\delta)\sin(2\theta)\cos(2\theta)}{f}\right].$$

The expressions for the phase velocity in TIH media and its derivative (equation (2-C-6) and (2-C-7)) can the be inserted into equation (2-C-2) to yield the group velocity for TIH media.

References

Arntsen B and Røsten T 2002 Wave equation versus Kirchhoff prestack depth migration of OBC data *Expanded Abstracts, 72nd Ann. Internat. Mtg., Soc. Expl.*

Berryman J G 1979 Long wave elastic anisotropy in transversly isotropic media *Geophysics* **44** 896-917

Claerbout J F 1971 Towards a unified theory of reflector mapping *Geophysics* **36** 467-481

Hale D 1991 Stable explicit depth extrapolation of seismic wavefields *Geophysics* **56** 1770-1777

Hoffe B H and Lines L 1990 Depth imaging by elastic waves - where P meets S *The Leading Edge* **18** 370-372

Holberg O 1988 Towards optimal one-way wave propagation *Geophys. Prosp.* **36** 99-114

Jin S, Mosher C C and Wu R 2002 Offset-domain pseudoscreen prestack depth migration *Geophysics* **67** 1895-1902

Kendall R R, Gray S H and Murphy G E 1998 Subsalt imaging using prestack depth migration of converted waves: Mahogany field, Gulf of Mexico *Expanded Abstracts, 68th Ann. Internat. Mtg., Soc. Expl.*

Rousseau J L, Calandra H and De Hoop M V 2003 Three-dimensional depth imaging with generalized screens: A salt body case study *Geophysics* **68** 1132-1139

Sollid A and Arntsen B 1993 Cost-effective 3D one-pass depth migration *Geophys. Prosp.* **42** 755-776

Soubaras R 2002 Comparison of Kirchhoff and wave-equation pre-stack migration of OBC data *Expanded Abstracts, 72nd Ann. Internat. Mtg., Soc. Expl.*

Thomsen L 1986 Weak elastic anisotrophy *Geophysics* **51** 1954-1966

Tsvankin I 1996 P-wave signatures and notation for transversely isotropic media: an overview *Geophysics* **61** 467-483

Uzcatequi O 1995 2D depth migration in transversely isotropic media using explicit operators *Geophysics* **60** 1819-1829

Zhang J, Verschuur D and Wapenaar C 2001 Depth migration of shot records in heterogeneous, transversely isotropic media using optimum explicit operators *Geophys. Prosp.* **49** 287-299

Zhu X, Langhammer J, King D, Madtson E, Helgesen H K and Brzostowski M 1999 Converted-wave prestack depth migration of North Sea salt domes *Expanded Abstracts, 69th Ann. Internat. Mtg., Soc. Expl.*

Chapter 3

Estimation of seafloor wave velocities and density from multicomponent data by AVA analysis

Abstract

This paper describes estimation of density and P-wave and S-wave velocities at the seafloor. The parameters are estimated by inversion of the acoustic-elastic reflection coefficient calculated from point-source measurements of pressure and vertical component of particle velocity recorded at the seafloor.

A “triangle”-Fourier transform (T-FT) is used to transform the pressure and particle velocity recordings from time-space domain to frequency-radial slowness domain. The reflection coefficient is then calculated by spectral division of the transformed two-component recordings. By performing the spectral division in the frequency-radial slowness domain we obtain a calculated reflection coefficient that is directly comparable to the theoretical reflection coefficient.

3.1 Introduction

Seabottom properties play an important role in fields as diverse as underwater acoustics, earthquake and geotechnical engineering, and marine geophysics. Water-column acousticians study shear and interface waves in the near bottom sediments with the aim of inferring seabed geo-acoustic parameters for predicting reflection and absorption of waves at the seafloor. Geotechnical engineers, working on design and siting of offshore structures focus on these waves to characterize soil and rock properties. In the field of geophysics, seabottom parameters are of interest for several reasons. In conventional marine acquisition these parameters determine the partitioning of the incident P-wave energy from the source into transmitted P-waves and mode-converted S-waves (Tatham and Goolsbee (1984), Kim and Seriff (1992)). Seafloor P- and S-wave velocities and density are also necessary inputs for decomposing multicomponent seafloor data into P- and S-waves (Amundsen and Reitan (1995a, 1995b)), as well as in the numerical study of wave propagation phenomena.

In this paper we present a method for inferring density and P- and S-wave velocity at the seabottom. The technique is based on estimating these parameters from the acoustic-elastic reflection coefficient calculated from point-source measurements of pressure and vertical component of particle velocity recorded at the seafloor. By spectral division of the two-component recordings transformed to the frequency-radial slowness domain, we obtain an estimate of the slowness-dependent reflection coefficient, containing AVA (amplitude versus angle) information. The reflection coefficient is then inverted with respect to wave velocities and density using an iterative least-squares inversion scheme.

The method presented here is similar to the method presented by Amundsen and Reitan (1995c). The major difference between the two methods is the domain in which the reflection coefficient is estimated. In Amundsen and Reitan (1995c) the reflection coefficient is estimated by spectral division of the two-component recordings in the frequency-radial wavenumber domain. Here we perform the spectral division in the frequency-radial slowness domain after applying a newly developed method that exactly transforms data from time-space domain to frequency-radial slowness domain.

Other seafloor parameter estimation techniques based on inversion of acoustic reflection amplitude data have been presented by, e.g., Chapman and Oldenburg (1986), Schmidt and Jensen (1986) and Chapman and Rohr (1991). The experimental geometry and the data measurements considered by these authors were, however, somewhat different. Their data base consists of seafloor reflected pressure seismograms measured by a series of hydrophones in the water layer. Furthermore, under conditions valid for ray theory they determine the plane-wave reflection coefficient from the ratio of the peak amplitudes of the reflected and the direct path signals, or by dividing the frequency spectrum of the reflected signal by that of the direct signal. More recent references on seafloor parameter estimation are Allnor *et al* (1997), Muyzert (2000), Schalkwijk *et al* (2003) and Muijs *et al* (2003,2004). Allnor *et al* (1997) and Muyzert (2000) estimated elastic properties of the seafloor using dispersion analysis of interface waves. Muijs *et al* (2003) estimated seafloor properties from multicomponent data in a similar fashion as Amundsen and Reitan (1995c), but using all four recorded data components. Schalkwijk *et al* (2003) and Muijs *et al* (2004) estimated elastic parameters at the seafloor in conjunction with decomposition of the recorded wavefield into upgoing and downgoing wavefields.

In the following the theoretical framework with related inversion procedure is briefly outlined. The viability of the inversion method is demonstrated through a synthetic data example.

3.2 Theory

In the experiment we assume that the water sound velocity α_1 and density ρ_1 are known, and that the seafloor at depth z_1 is flat. From a point source explosion in the water layer the resulting wavefield is measured along a line of hydrophones and vertical component geophones deployed at the seabottom. We assume that the dominant recorded energy is the direct wave and the primary reflection at the seafloor, and that these events are well separated in time from strong, reflected events from subsurface structures. These latter events can then be muted. This strategy is a reasonable approximation when the near-seabottom layers do not produce any significant scattered energy. The ideal medium is, of course, a medium with a thick nonscattering sediment column below the seafloor.

A “triangle”-Fourier transform (T-FT) is used to transform the pressure and particle velocity data from time-space $t - x$ domain to frequency-radial slowness $\omega - p$ domain.

3.2.1 Calculation of the reflection coefficient

In an acoustic medium the upgoing U and downgoing D pressure component can be computed from the transformed fields P and V_z by (Amundsen and

Reitan (1995a))

$$U(z_1) = P(z_1) - (\rho_1/q_{\alpha_1})\, V_z(z_1), \tag{3.1}$$

and

$$D(z_1) = P(z_1) + (\rho_1/q_{\alpha_1})\, V_z(z_1), \tag{3.2}$$

where $q_{\alpha_1} = \sqrt{\alpha_1^{-2} - p^2}$ is the vertical slowness. The radial slowness p is related to the radial wavenumber k and P-wave angle of incidence θ as $p = k/\omega = \sin\theta/\alpha_1$. The radial wavenumber k is related to the horizontal wavenumbers k_x and k_y through $k^2 = k_x^2 + k_y^2$.

The reflection coefficient for the fluid-solid boundary can be calculated from the transformed fields P and V_z as the ratio between the upgoing and the downgoing pressure component by

$$R^{calc}(z_1) = \frac{P(z_1) - (\rho_1/q_{\alpha_1})\, V_z(z_1)}{P(z_1) + (\rho_1/q_{\alpha_1})\, V_z(z_1)}. \tag{3.3}$$

The theoretical plane-wave reflection coefficient for a seafloor with constant P- and S-wave velocities α_2 and β_2, respectively, and density ρ_2 is (Berkhout (1987))

$$R^{theo}(z_1) = \frac{A_1\rho_2 q_{\alpha_1} + A_2 q_{\alpha_1} q_{\alpha_2} - \rho_1 q_{\alpha_2}}{A_1\rho_2 q_{\alpha_1} + A_2 q_{\alpha_1} q_{\alpha_2} + \rho_1 q_{\alpha_2}}, \tag{3.4}$$

where A_1 and A_2 are shear coefficients, $A_1 = (1 - 2p^2\beta_2^2)^2$, $A_2 = 4p^2\rho_2\beta_2^4 q_{\beta_2}$, and q_{α_2} and q_{β_2} are, respectively vertical P-wave and S-wave slownesses in the solid. Note that R^{theo} is a function of radial slowness p.

Given a calculated reflection coefficient for various slownesses, we may estimate the three unknown parameters $(\alpha_2, \beta_2, \rho_2)$ by inversion. Since this inverse problem is nonlinear we apply a classical iterative least-squares Gauss-Newton scheme which minimizes the misfit between the theoretical reflection coefficient R^{theo} and the calculated reflection coefficient R^{calc}. From the estimated values $\alpha_2^{est}, \beta_2^{est}$ and ρ_2^{est} we may calculate a predicted reflection coefficient from equation (3.4).

Real data measurements will most likely be contaminated by noise from a number of sources with varying degrees of dominance. Also poor and variable geophone planting can seriously distort the seismic signals. Depending on the noise characteristics, other optimization criteria with more robust statistical properties than the least-squares criterion can of course be used in the parameter estimation problem.

3.2.2 The triangle-Fourier transform

The triangle-Fourier transform (see Ikelle and Amundsen (2005)) which is also described in Appendix 3.A is a modified version of the Fourier transform that outputs data on regular lines of radial slowness p in the Fourier domain.

Consider the sampled space-time data $u(n_x\Delta x, n_t\Delta t)$ for $n_x = 1, 2, ..., N_X$ and $n_t = 0, 2, ..., N_T - 1$, where Δx and Δt are spatial and temporal sampling intervals, respectively. In the following, suppress the sampling intervals of the data. The discrete 2D FT from space-time domain to frequency-wavenumber domain is achieved in two operations. First, FT the space-time data $u(n_x, n_t)$ to frequency domain, $\tilde{U}(n_x, n_\omega)$. The FT formula is defined as

$$\tilde{U}(n_x, n_\omega) = \sum_{n_t=0}^{N_T-1} u(n_x, n_t) \exp\left(i\frac{2\pi n_\omega \cdot n_t}{N_T}\right) \tag{3.5}$$

for $n_\omega = 0, ..., N_T/2$. Then, apply the FT to $U(n_x, n_\omega)$ from space to wavenumber,

$$U(n_{k_x}, n_\omega) = \sum_{n_x=-N_X/2+1}^{N_X/2} \tilde{U}(n_x, n_\omega) \exp\left(-i\frac{2\pi n_{k_x} \cdot n_x}{N_X}\right) \tag{3.6}$$

for $n_{k_x} = -N_X/2 + 1, ..., N_X/2$. Here figure 3.1 shows the $\omega - k_x$-grid for $N_T = 32$ and $N_X = 16$. In this case, $N_W = 16$ and $N_{K_X} = 16$.

The grid in figure 3.1, however, is not optimal for calculating the slowness dependent reflection coefficient. In numerical computations, since the 2-D FT of $u(n_x, n_t)$ gives data on a regular grid as function of frequency ω and wavenumber k_x, interpolation on the $\omega - k_x$-grid to the lines $k_x = p\omega$ (for varying p) is required.

On the other hand, the use of the so-called pseudo-polar, or triangle, Fourier transform eliminates the interpolation problem. The triangle-Fourier transform (T-FT) combines the conventional FT (3.5) over temporal samples with a modified FT over spatial samples. In the spatial FT (3.6), letting

$$n_x \to 2n_x \cdot n_\omega / N_T, \quad n_\omega = 0, ..., N_T/2, \tag{3.7}$$

outputs transformed data on a non-Cartesian point-set, as illustrated in figure 3.2. This grid, a subset of the pseudo-polar grid, we call the triangle grid. The T-FT outputs the Fourier transformed data on the required lines $k_x = p\omega$.

How can we implement the T-FT to make it computationally fast? We here present one possible solution based on the fast fractional Fourier transform (Bailey and Swarztrauber, 1991). Equation (3.6) gives the conventional FT from space to wavenumber:

$$U(n_{k_x}) = \sum_{n_x=-N_X/2+1}^{N_X/2} \tilde{U}(n_x) \exp\left(-i\frac{2\pi n_{k_x} \cdot n_x}{N_X}\right), \tag{3.8}$$

for $n_{k_x} = -N_X/2+1, ..., N_X/2$. Here we have suppressed the n_ω-dependency. For the T-FT, n_x appearing in the exponential function above must be replaced according to equation (3.7) by $n_x \cdot \alpha$, where $\alpha = 2n_\omega/N_T$. Inserting into (3.8) yields

$$U(n_{k_x}) = \sum_{n_x=-N_X/2+1}^{N_X/2} \tilde{U}(n_x) \exp\left(-i\frac{2\pi n_{k_x} \cdot n_x}{N_X} \cdot \alpha\right), \tag{3.9}$$

for $n_{k_x} = -N_X/2 + 1, ..., N_X/2$. This expression is known as the fractional Fourier transform. Noting that

$$-2n_{k_x} \cdot n_x = (n_{k_x} - n_x)^2 - (n_{k_x})^2 - (n_x)^2 \tag{3.10}$$

the expression for the fractional Fourier transform becomes

$$\begin{aligned} U(n_{k_x}) &= \exp\left(-i\frac{\pi(n_{k_x})^2}{N_X} \cdot \alpha\right) \qquad (3.11) \\ &\sum_{n_x=-N_X/2+1}^{N_X/2} \left\{\tilde{U}(n_x) \exp\left(-i\frac{\pi(n_x)^2}{N_X} \cdot \alpha\right)\right\} \exp\left(i\frac{\pi(n_{k_x} - n_x)^2}{N_X} \cdot \alpha\right), \end{aligned}$$

for $n_{k_x} = -N_X/2 + 1, ..., N_X/2$. The sum is recognized as a convolution between two functions: the one inside the curly brackets and the exponential function. The convolution most efficiently is implemented by Fourier transforming the two functions, multiplying their Fourier transforms, before applying an inverse Fourier transform. Then the convolution expression is multiplied by the exponential function in front of the sum sign to obtain the triangle Fourier transform of the seismic data. All Fourier transforms are computed, of course, by FFTs.

3.3 Numerical results

In this section the viability of the inversion method is demonstrated through a synthetic data example. The pressure and vertical component of particle velocity recordings at the seafloor are modeled using the modeling package OSIRIS^{TM}. The model consist of a 300 meters thick water layer overlaying an acoustic half-space. The seafloor parameters at the seabed used in the modeling are density $\rho_2 = 2000$ kg/m^3 and wave velocities $\alpha_2 = 1880$ m/s and $\beta_2 = 550$ m/s. The fluid parameters were $\rho_1 = 1040$ kg/m^3 and $\alpha_1 = 1480$ m/s.

3.3.1 Parameter sensitivity of reflection coefficients

Before the inversion process is run we want to show the sensitivity of the acoustic-elastic reflection coefficient to variations in P- and S-wave velocities and density from the above model. We show amplitude behavior of the resulting reflection coefficients.

In figure 3.4a the amplitude dependence of R is shown for two P-wave velocities differing from $\alpha_2 = 1880$ m/s with ± 100 m/s. The S-wave velocity and density are kept constant. We observe a very strong sensitivity in amplitude to the P-wave velocity near the critical angle for onset of evanescent P-waves, $\theta_c = \arcsin(\alpha_1/\alpha_2)$. Hence, the P-wave velocity should be well determined when near- and postcritically reflected data are included in the inversion process.

In figure 3.4b the amplitude dependence of R are displayed for two S-wave velocities differing from $\beta_2 = 550$ m/s with ± 100 m/s. P-wave velocity and density are held constant. For our model the amplitude sensitivity are significant for P-wave postcritical angles of incidence. The reflection coefficient shows, however, a small amplitude sensitivity also to variations in S-wave velocity for angles below the P-wave critical angle. In this region R is real. Increasing S-wave velocities lead to decreasing reflection coefficient near the P-wave critical angle, and hence, a decrease in the reflected amplitude.

In figure 3.4c the amplitude dependence of R is shown for two densities differing from $\rho_2 = 2000$ kg/m^3 with ± 200 kg/m^3. Wave velocities were kept constant. The most significant variation is in this case in the precritical region of the amplitude spectrum. The zero-offset reflection coefficient is known to determine the product of density and P-wave speed, that is, $\rho_2\alpha_2$. Since the P-wave velocity strongly depends on the critical reflection angle we may deduce that the density will be determined from the strength of the reflection coefficient at small angles of incidence, provided that P-wave critical angle reflection data are included in the parameter estimation.

Our observations are consistent with what is typically observed when considering parameter estimation from real multicomponent data. Muijs *et al* (2004), for instance, showed that the best determined parameters are P-wave velocity and density while S-wave velocity is more difficult to determine with confidence.

3.3.2 Parameter estimation

Following the strategy outlined in the previous section we calculate the reflection coefficient from the pressure and vertical component of particle velocity at the seafloor. The modeled data are displayed in figures 3.5 and 3.6. The data window considered in the estimation of the reflection coefficient is 0.5 seconds in time and 750 meters in offset. In the frequency domain we use data between $25 - 60$ Hz for estimating the reflection coefficient.

We have for comparison also included the results from calculating the reflection coefficient by spectral division of the pressure and vertical component of particle velocity transformed to the frequency-radial wavenumber $\omega - k$ domain as presented by Amundsen and Reitan (1995c).

In figures 3.7a and 3.7b the amplitude spectra of the calculated reflection coefficient is presented. The reflection coefficient in figure 3.7a is calculated based on spectral division of the two-component recordings transformed to the frequency-radial wavenumber $\omega - k$. The reflection coefficient in figure 3.7b is calculated based on spectral division in the frequency-radial slowness $\omega - p$ domain. In figure 3.7c we show the mean and median values (mean and median values of the reflection coefficient for each slowness p) for the data in figure 3.7b. On all figures 3.7a, 3.7b and 3.7c we have for comparison also plotted the theoretical reflection coefficient together with the estimated reflection coefficients.

Applying the inversion scheme with input data shown in figures 3.7a, 3.7b and 3.7c we obtain the estimated parameters presented in table 3.1. We see that calculation of the reflection coefficient in the frequency-radial slowness $\omega - p$ domain gives slightly better estimates for the inverted parameters than the method presented by Amundsen and Reitan (1995c) where the reflection coefficient is calculated in the frequency-radial wavenumber $\omega - k$ domain. The maximum angle of incidence considered by the algorithm was $\theta_{max} = 60$

degrees (corresponding to the maximum radial slowness $p_{max} = \sin\theta_{max}/\alpha_1$). If the inversion algorithm is constrained to process lower maximum incidence angles, the estimates of P-wave velocity and density still become the same, but the S-wave velocity turns out to be less well determined. This result is in good agreement with the sensitivity analysis, where we predicted that P-wave postcritical angles would be important for confidently determining the S-wave velocity. The P-wave critical angle is $\theta_c \approx 52$ degrees.

3.4 Conclusions

A simple inversion method has been described for estimating the seafloor wave velocities and density. The method is based on determining the PP reflection coefficient in the frequency-slowness domain from seafloor measurements of the pressure and the vertical component of the particle velocity. Frequency-slowness domain analysis lends itself naturally to the exploitation of median or mean values for every slowness as input to least-squares inversion.

The algorithm gives estimates of seafloor parameters in good agreement with the true model parameters. The two best determined parameters are the P-wave velocity and density, provided that P-wave critical angle reflections are included in the AVA analysis. The reflection amplitude depends strongly on the P-wave critical angle of incidence, which determines the P-wave velocity. The density is then determined by the strength of the reflection coefficient in the P-wave precritical region down to zero-offset. The S-wave velocity is more difficult to determine with confidence. This is related to the fact that the PP reflection coefficient is rather insensitive to the S-wave velocity at precritical angles of incidence.

Acknowledgments

We thank Statoil for permission to publish this work. H.K.H. would also like to thank Statoil for financial support.

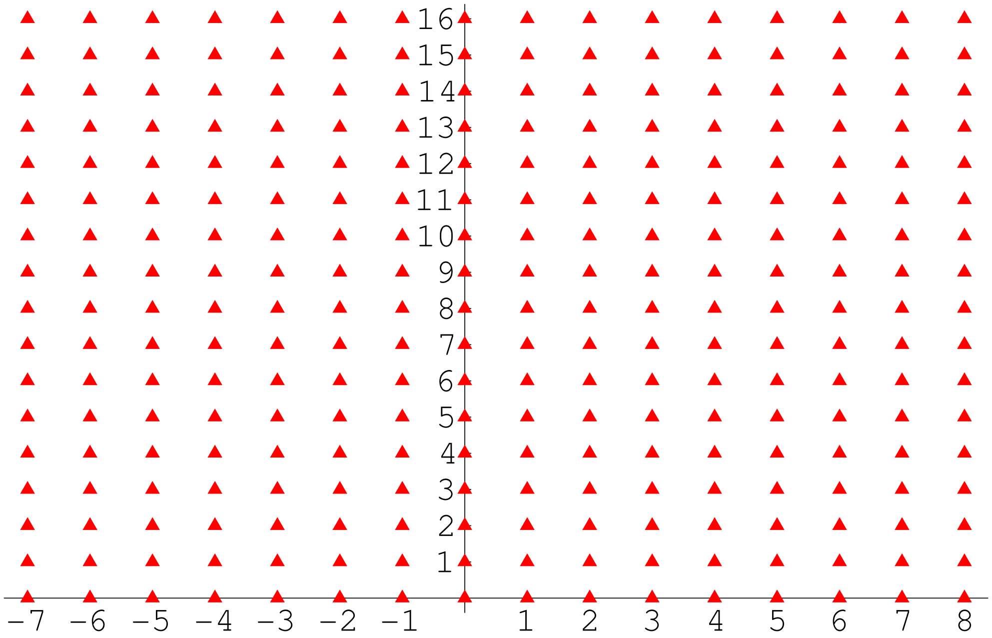

Figure 3.1: Time-space data have $N_T = 32$ and $N_X = 16$ samples. The red triangles show the related Cartesian $k_x - \omega$-grid with $n_{k_x} = -N_X/2 + 1, ..., N_X/2$ along the horizontal axis and $n_\omega = 0, N_T/2$ along the vertical axis.

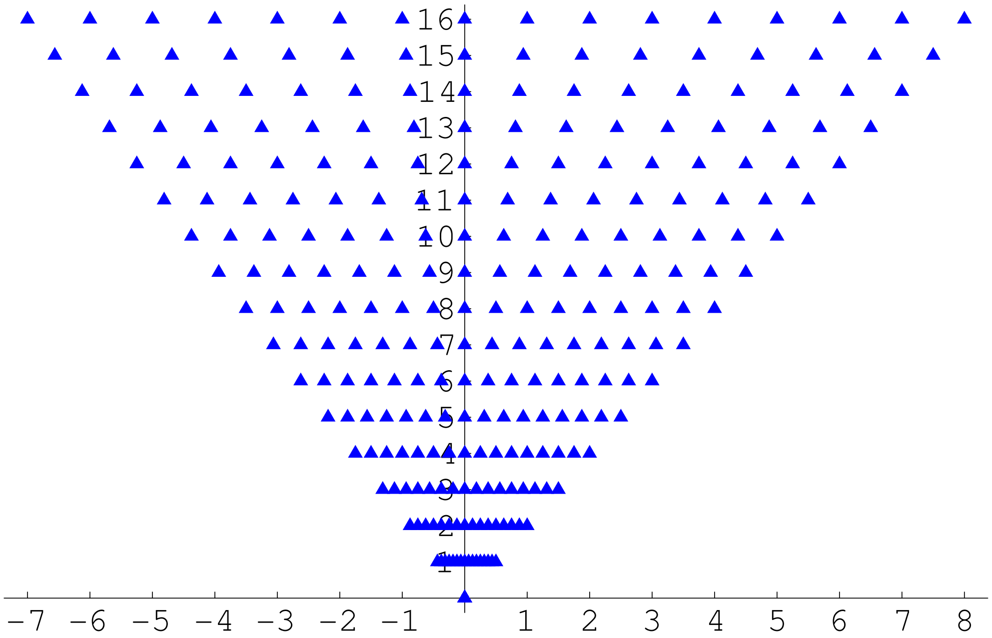

Figure 3.2: Time-space data has $N_T = 32$ and $N_X = 16$ samples. The blue triangles show the related triangle (pseudo-polar) grid with $n_{k_x} = -N_X/2 + 1, ..., N_X/2$ along the horizontal axis and $n_\omega = 0, N_T/2$ along the vertical axis.

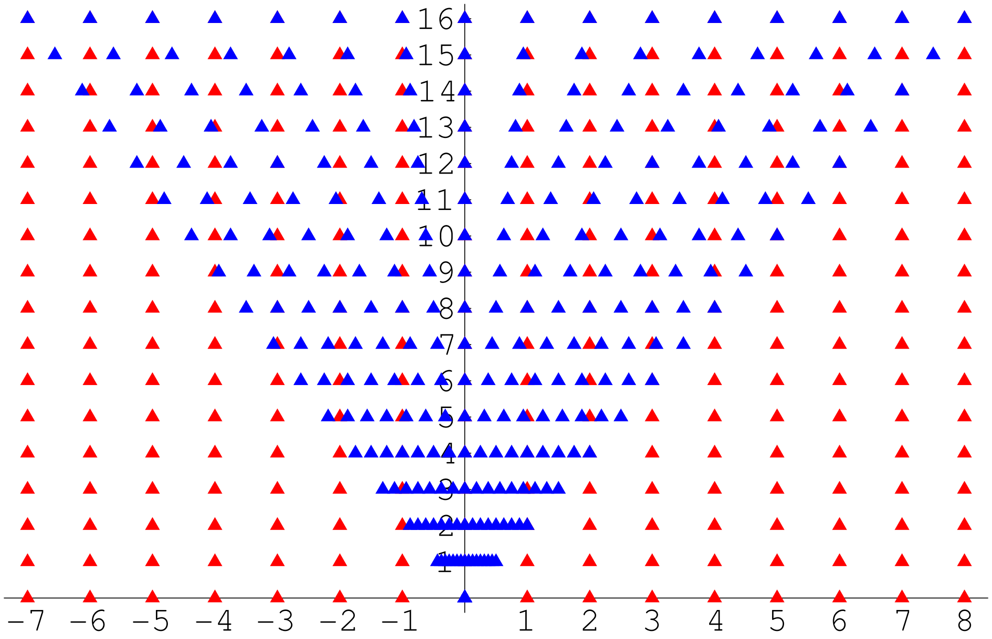

Figure 3.3: The Cartesian (red) and triangle (blue) grids in figures 3.1 and 3.2, respectively, plotted on top of each other.

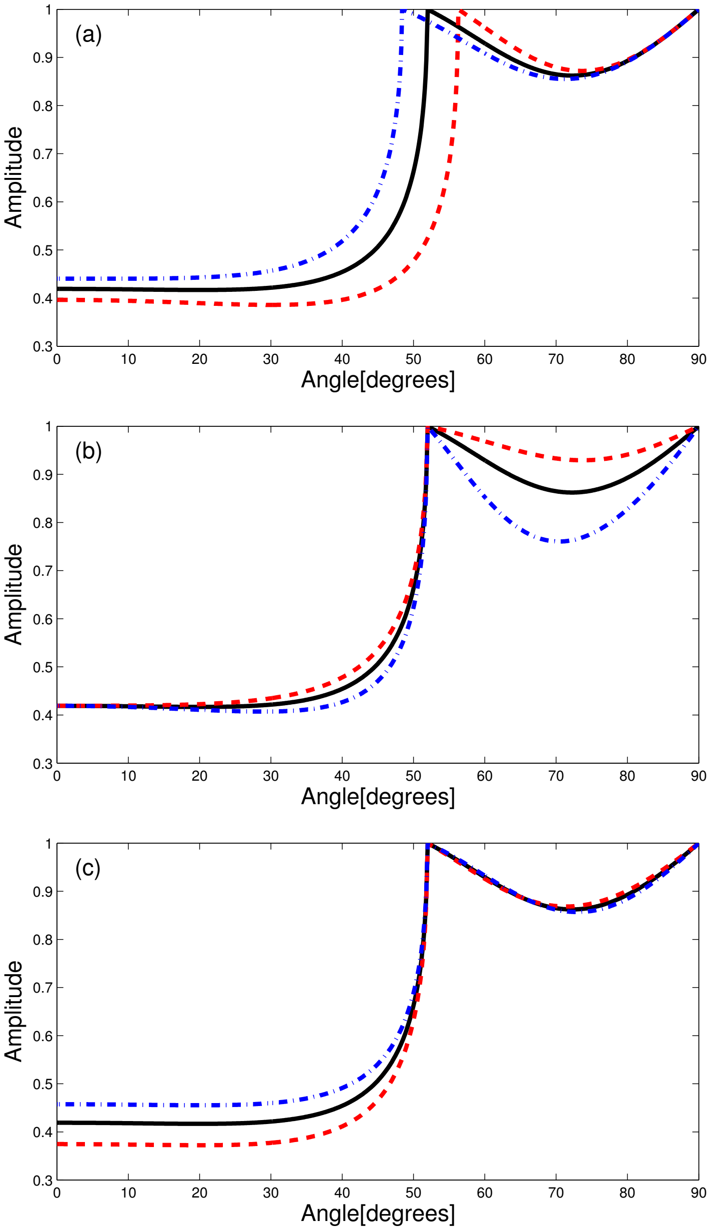

Figure 3.4: Dependence of plane wave reflection coefficient (amplitude spectra) on (a) P-wave velocity: α_2 =1880 m/s (solid black line); α_2 =1780 m/s (broken red line); α_2 =1980 m/s (dotted blue line), (b) S-wave velocity: β_2 =550 m/s (solid black line); β_2 =450 m/s (broken red line); β_2 =650 m/s (dotted blue line), and (c) density: ρ_2 =2000 kg/m^3 (solid black line); ρ_2 =1800 kg/m^3 (broken red line); ρ_2 =2200 kg/m^3 (dotted blue line).

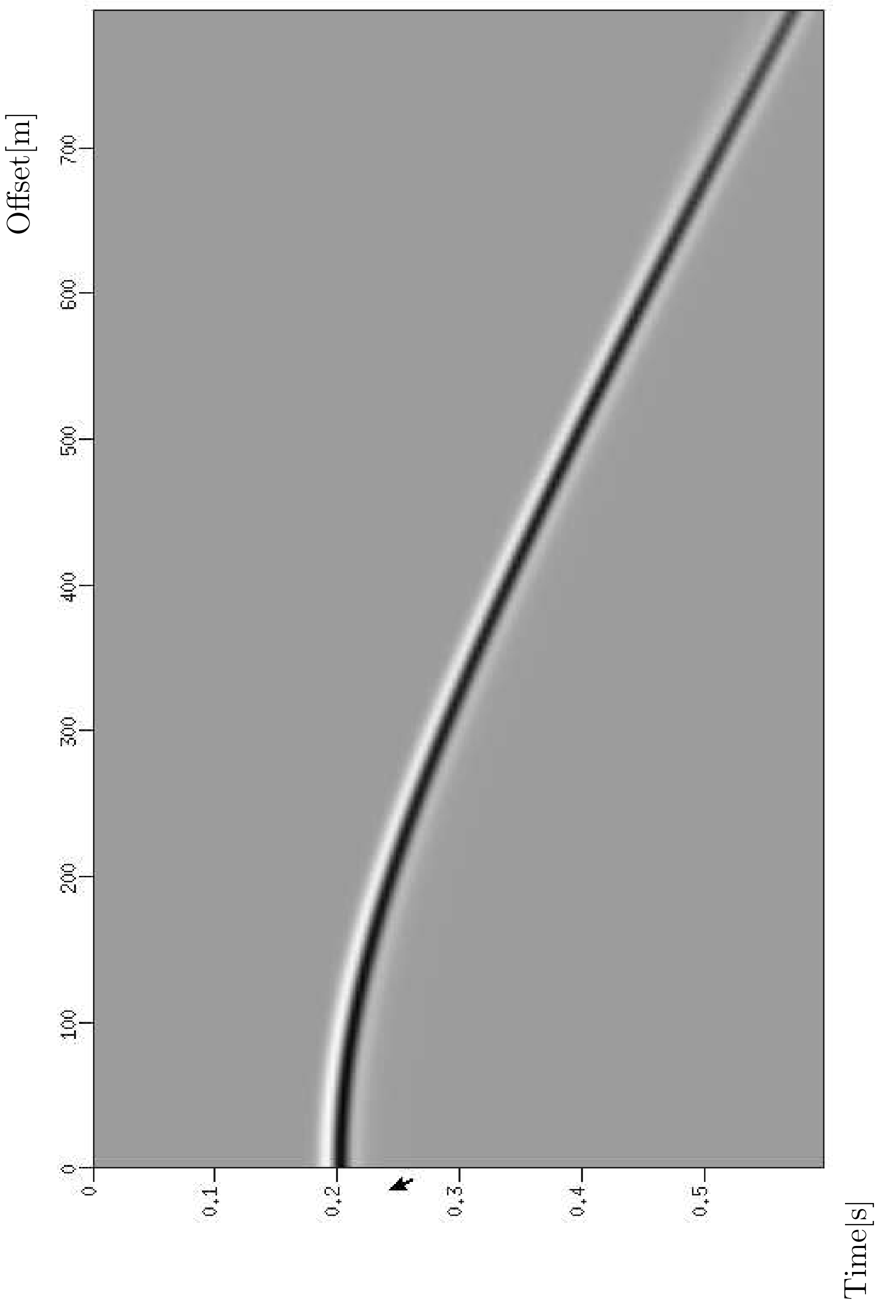

Figure 3.5: Modeled pressure recordings at the seafloor.

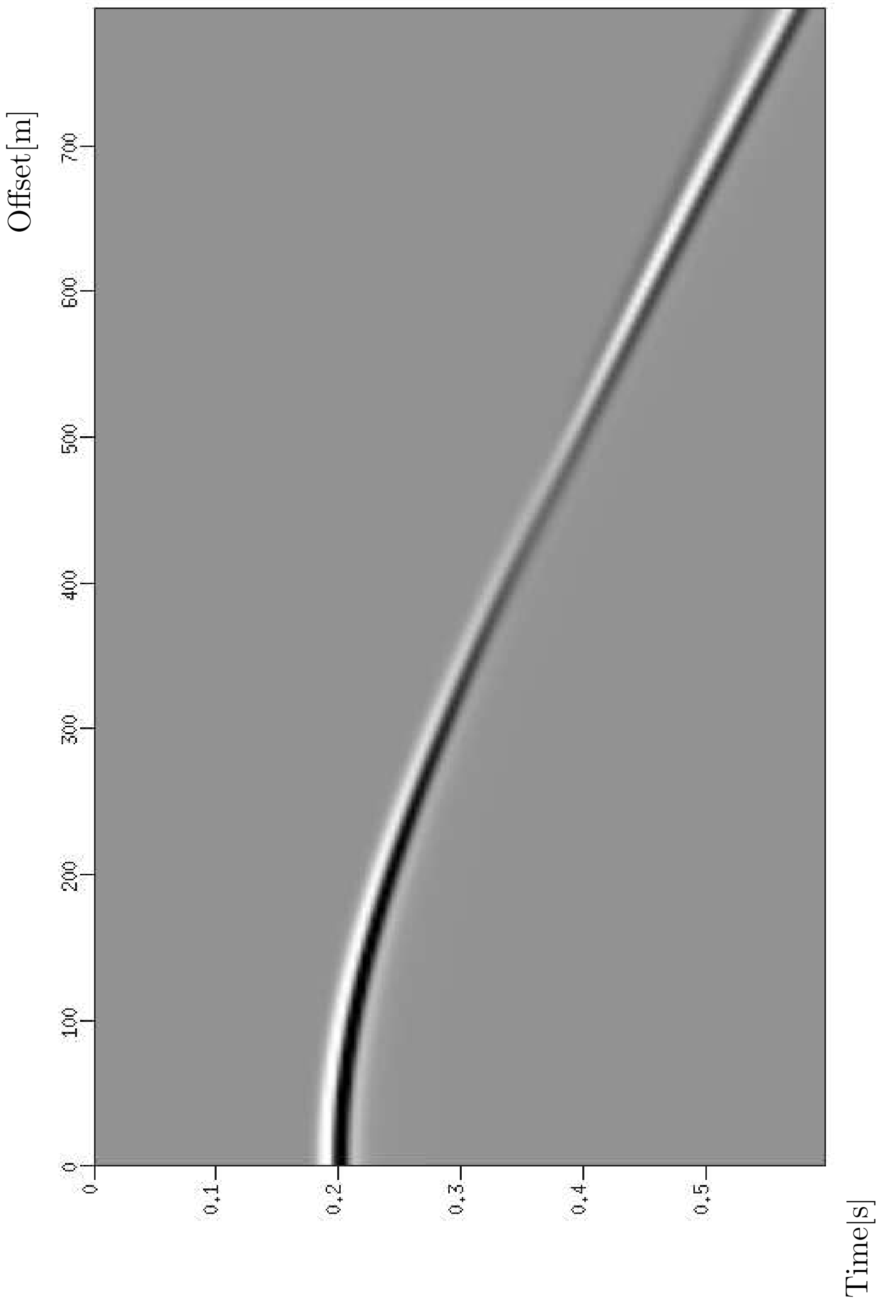

Figure 3.6: Modeled vertical velocity component recordings at the seafloor.

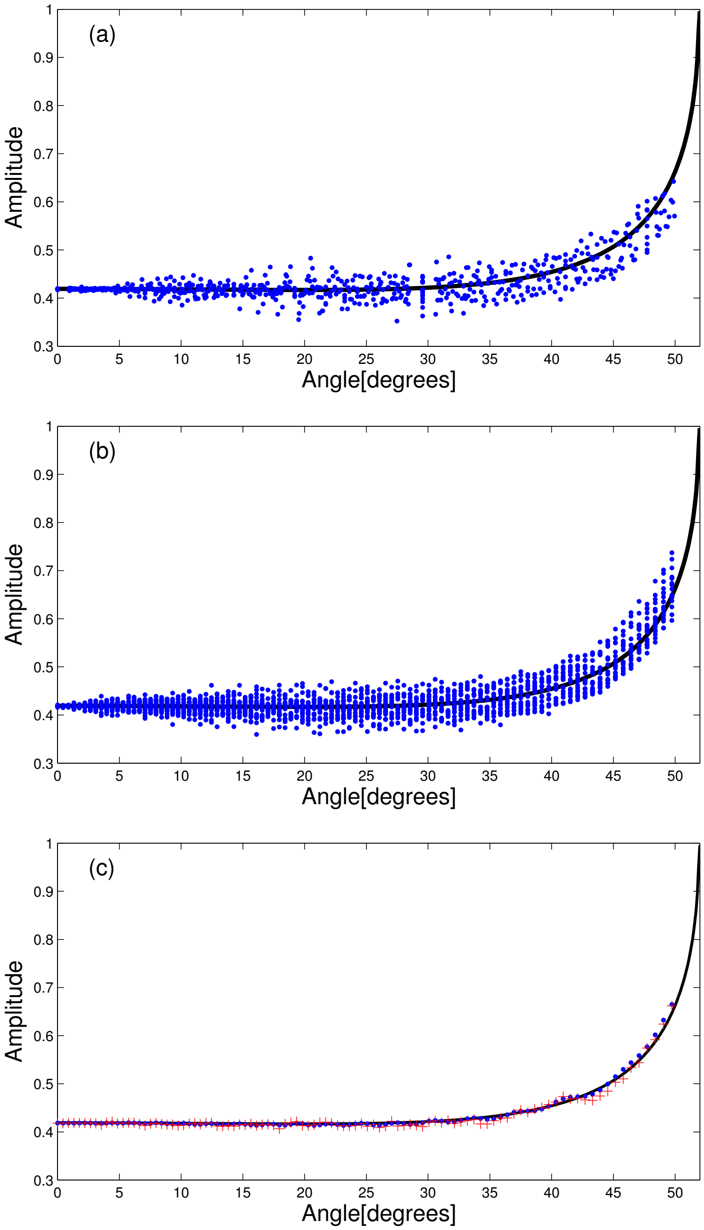

Figure 3.7: (a) Estimated reflection coefficient using regular FFT, (b) Estimated reflection coefficient using fractional FFT and (c) Mean (crosses) and median (dots) values of data in (b). On all figures a, b and c we have for comparison also plotted the theoretical reflection coefficient as a solid black line.

Parameter	Exact	a) using FT	b) using T-FT	c) using mean values	d) using median values
α_2 $[m/s]$	1880	1856	1890	1891	1890
β_2 $[m/s]$	550	536	562	562	579
ρ_2 $[kg/m^3]$	2000	2020	1983	1983	1984

Table 3.1: The estimated wave velocities and density based on inversion of the calculated reflection coefficient. The tabular shows the estimated parameters based on using a) FT and b) T-FT when calculating the reflection coefficient. The estimated parameters using c) mean and d) median values from the estimated reflection coefficient using T-FT are also presented.

Appendix 3.A
The Radon transform in geophysics

In this appendix we will consider the relation between the Radon transform, the Fourier ransform and the triangle Fourier transform (see Ikelle and Amundsen (2005)).

Let $u(x,t)$ represent a seismogram (seismic section) at the surface, $z=0$. The Radon transform is

$$\breve{u}(p,\tau) \;=\; \int\int dxdt\delta(t-px-\tau)u(x,t), \tag{3-A-1}$$

The relation between the Radon transform and the Fourier transform (FT) is straightforward:

$$U(\omega p,\omega) = \int d\tau \exp(i\omega\tau)\breve{u}(p,\tau) \ . \tag{3-A-2}$$

Symbolically,

$$\mathcal{F}_2 u = \mathcal{F}_1 \breve{u} \ , \tag{3-A-3}$$

where $\mathcal{F}_2$ and $\mathcal{F}_1$ denotes 2D and 1D, respectively, Fourier transforms. Thus, the Fourier transform of the Radon transform with respect to the intercept variable τ is equal to the 2D Fourier transform of $u(x,t)$ evaluated on the line $k_x = p\omega$.

The inverse Radon transform can be represented in many ways; for instance,

$$u(x,t) = -\frac{1}{2\pi^2}\int\int dpd\tau \frac{\partial\breve{u}(p,\tau-px)/\partial\tau}{\tau-t} \ . \tag{3-A-4}$$

The Radon transformed function $\breve{u}(p,\tau)$ is also referred to as the slowness representation, plane-wave decomposition, or slant stack. The latter expression is quite obvious: one stacks all the values of the wavefield on each "slant" line. The Radon transform thus takes a line of slope p_0 and intercept τ_0 in xt-space and transforms it into a point (p_0,τ_0) in the new domain. That is, the Radon transform takes a line into a point. The inverse Radon transform takes the point back to the original line.

In contrast, the 2D Fourier transform takes a line in the $t-x$ domain into a line in the $f-k$ domain, and the inverse Fourier transform takes it back to the original line. For instance, the Fourier transform of the line $t = px + \tau$ is

$$\int_{-\infty}^{\infty}\int_{-\infty}^{\infty} dxdt \exp[i(\omega t - k_x x)]\delta(t - px - \tau) =$$
$$\int_{-\infty}^{\infty} dx \exp\{i\left[\omega(px + \tau) - k_x x\right]\} =$$
$$2\pi \exp(i\omega\tau)\delta(p\omega - k_x) \ .$$

Thus, the Fourier transform has a magnitude given by a delta function along the line $\omega = k_x/p$ and has a phase given by $\omega\tau$. Note that the line goes through the origin (intercept zero), has a reciprocal slope of the xt-line. In addition, the phase spectrum contains information about the intercept τ. The inverse Fourier transform regains the original line

$$\frac{1}{(2\pi)^2}\int_{-\infty}^{\infty}\int_{-\infty}^{\infty} dk_x d\omega \exp[-i(\omega t - k_x x)] \exp(i\omega\tau)\delta(p\omega - k_x) = \delta(t - px - \tau) \ .$$

On the Discrete Fast Radon Transform

We have briefly discussed the Radon transform in continuous terms. For many modern seismic applications, like multiple-elimination in $(\tau - p)$-domain[1], it is important to find a fast, digital Radon transform for sampled seismic data. Over the last twenty years, in seismic as well as other disciplines, attention to this problem has been given. Mersereau and Oppenheim (1974) introduced a non-Cartesian grid in the 2D Fourier plane, called the concentric squares grid. Recently, Averbuch *et al* (2003) have proposed a discrete Radon transform that is rapidly computable and invertible by means of fast Fourier transforms (FFTs). Its basis is the concentric squares grid, which

---

[1] Multiple suppression by predictive deconvolution builds on the periodicity of multiples. However, on time-distance gathers, like common shot gathers, common midpoint gathers, or common receiver gathers, multiples are not periodic in time for non-zero offsets. Multiples in layered media are periodic along radial traces (fixed p). The time separation is different from one radial trace to another. Therefore, a predictive deconvolution operator can be designed from the autocorrelogram of each p-trace and applied to attenuate multiples in (τ, p)-domain, where the primary and subsequent multiples are ellipses.

they call the pseudo-polar grid. In this appendix, we take advantage of the idea of the concentric squares grid, or the pseudo-polar grid, as introduced by these authors, to transform data to the 2D Fourier space. For most seismic applications, it is sufficient to transform data to a triangle sub-domain of the concentric squares grid. Therefore, we call for short the transform the triangle-Fourier transform (T-FT). The T-FT is also discussed in Ikelle and Amundsen (2005).

Before we consider the triangle-Fourier transform, it is instructive to discuss the use of the projection-slice theorem as a basis for the Radon transform. The projection-slice theorem says that the Radon transform can be obtained by

(a) performing a 2D Fourier transform of (x, t) data,

(b) obtaining a radial slice of the 2D Fourier transform, and

(c) applying a 1D inverse Fourier transform to the radial slice.

The projection-slice theorem can be exploited for discrete data by replacing steps (a) and (c) by 2D and 1D FTs on data in Cartesian grids. However, step (b) then requires interpolation since the radial slices of the Fourier domain generally do not intersect the Cartesian grid outputted by the 2D FT.

Let us look into this in more detail by considering the sampled space-time data $u(n_x\Delta x, n_t\Delta t)$ for $n_x = 1, 2, ..., N_X$ and $n_t = 0, 2, ..., N_T - 1$, where Δx and Δt are spatial and temporal sampling intervals, respectively. A 2D Fourier transform over time and space gives the corresponding data in frequency-wavenumber domain. The Nyquist frequency and Nyquist wavenumber are $\omega^{(N)} = \pi/\Delta t$ and $k_x^{(N)} = \pi/\Delta x$, respectively. Since u is real, we need only consider the zero and positive frequencies. The zero'th and positive frequencies up to Nyquist take values $n_\omega = 0, 2, ..., N_W$, where $N_W = N_T/2$. The frequency sampling interval is

$$\Delta\omega = 2\omega^{(N)}/N_T. \tag{3-A-5}$$

Both positive and negative wavenumbers must be considered, $n_{k_x} = -N_X/2 + 1, -N_X/2 + 2, ..., -1, 0, 1, ..., N_X/2 - 1, N_X/2$. The number of wavenumbers N_{K_X} equals the number of spatial samples N_X. The wavenumber sampling interval is

$$\Delta k_x = 2k_x^{(N)}/N_X. \tag{3-A-6}$$

The sampled 2D Fourier transform thus is $U(n_{k_x}\Delta k_x, n_\omega \Delta\omega)$. In the following, suppress the sampling intervals of the data.

The 2D FT from space-time domain to frequency-wavenumber domain is achieved in two operations. First, FT the temporal data $u(n_x, n_t)$ to frequency domain, $\tilde{U}(n_x, n_\omega)$. The FT formula is defined as

$$\tilde{U}(n_x, n_\omega) = \sum_{n_t=0}^{N_T-1} u(n_x, n_t) \exp\left(i\frac{2\pi n_\omega \cdot n_t}{N_T}\right), \tag{3-A-7}$$

for $n_\omega = 0, ..., N_T/2$. Then, apply the FT to $U(n_x, n_\omega)$ from space to wavenumber,

$$U(n_{k_x}, n_\omega) = \sum_{n_x=-N_X/2+1}^{N_X/2} \tilde{U}(n_x, n_\omega) \exp\left(-i\frac{2\pi n_{k_x} \cdot n_x}{N_X}\right), \tag{3-A-8}$$

for $n_{k_x} = -N_X/2+1, ..., N_X/2$. It is common practice to plot the wavenumbers along the horizontal axis and the positive frequencies along the vertical axis in upward direction. Figure (3.1) shows the $\omega - k_x$-grid for $N_T = 32$ and $N_X = 16$. In this case, $N_W = 16$ and $N_{K_X} = 16$.

The grid in Figure (3.1), however, is not suitable for the discrete Radon transform. The Fourier slice theorem shows that the Fourier transform of the Radon transform with respect to the intercept variable τ is equal to the 2D Fourier transform of $u(x, t)$ evaluated on the line $k_x = p\omega$. In numerical computations, however, since the 2D FT of $u(n_x, n_t)$ gives data on a regular grid as function of frequency ω and wavenumber k_x, that is, $U(n_{k_x}, n_\omega)$, generally, interpolation on the $\omega - k_x$-grid to the lines $k_x = p\omega$ (for varying p) is required.

On the other hand, the use of the so-called pseudo-polar, or triangle, Fourier transform eliminates the interpolation problem. The triangle-Fourier transform (T-FT) combines the conventional FT (3-A-7) over temporal samples with a modified FT over spatial samples. In the spatial FT (3-A-8), letting

$$n_x \rightarrow 2n_x \cdot n_\omega / N_T, \quad n_\omega = 0, ..., N_T/2, \tag{3-A-9}$$

outputs transformed data on a non-Cartesian point-set, as illustrated in Figure (3.2). This grid, a subset of the pseudo-polar grid, we call the triangle grid. This type of grid, which enables fast Fourier computations, has been considered by many scientists since the 1970s and until recently. The pioneers in this field are Mersereau and Oppenheim (1974) who proposed the so-called Linogram grid. Recently, the pseudo-polar grid was proposed as the base for fast slant-stack (Averbuch *et al* (2003)).

The T-FT outputs the Fourier transformed data on the required lines $k_x = p\omega$. The sampled lines are $n_{p_x} = -N_{P_X}/2+1, -N_{P_X}/2+2, ..., N_{P_X}/2-1, N_{P_X}/2$. The number of lines N_{P_X} equals the number of wavenumbers N_{K_X} which equals the number of spatial samples N_X. For $k_x \geq 0$, the p-lines are given as

$$\begin{aligned} p_0 &= 0 \\ p_1 &= \Delta k_x/\omega^{(N)} = \frac{1}{(N_X/2)}\frac{\Delta t}{\Delta x} \\ &. \\ p_{n_{p_x}} &= n_{p_x}\Delta k_x/\omega^{(N)} = \frac{n_{p_x}}{(N_X/2)}\frac{\Delta t}{\Delta x} \\ &. \\ p_{N_{P_X}/2} &= k_x^{(N)}/\omega^{(N)} = \frac{\Delta t}{\Delta x} \end{aligned}$$

Observe that the lines are equispaced in slope, with slowness sampling interval

$$\Delta p = \frac{1}{(N_X/2)}\frac{\Delta t}{\Delta x}, \qquad (3\text{-A-}10)$$

but have different lengths (radius). Furthermore, as shown in Figure (3.3), any signal information in frequency-wavenumber domain that is outside the blue triangle will not be present after the application of the T-FT. Therefore, the T-FT implicitly produces a velocity filtering of the seismic data. For example, for $\Delta t = 0.008$ ms and $\Delta x = 12.5$ m, line $N_{P_X}/2$ corresponds to the apparent velocity $p^{-1}_{N_{P_X}/2} = 1562.5$ m/s. Any signal with lower apparent velocity will be filtered.

Applying a 1D inverse Fourier transform for every p-trace now gives the Radon transformed data. The discrete Radon transform is exact, invertible, and rapid to compute. In this appendix, we have shown how to compute the Radon transform for 2D seismic data. It is straightforward to generalize the procedure to compute the 3D Radon transform, or $\tau - p_x - p_y$ transform, of 3D sampled seismic data $u(n_x, n_y, n_t)$, where $n_y = 1, .., N_Y$, and N_Y is the number of traces in the crossline direction. Basically, in the spatial FFT from y-coordinate to k_y-wavenumber, one merely has to substitute $n_y \rightarrow 2n_y \cdot n_\omega/N_T$.

On the numerical implementation of the triangle Fourier transform

How can we implement the T-FT to make it computationally fast? We here present one possible solution based on the fast fractional Fourier transform (Bailey and Swarztrauber, 1991). Equation (3-A-8) gives the conventional FT from space to wavenumber:

$$U(n_{k_x}) = \sum_{n_x=-N_X/2+1}^{N_X/2} \tilde{U}(n_x) \exp\left(-i\frac{2\pi n_{k_x} \cdot n_x}{N_X}\right), \tag{3-A-11}$$

for $n_{k_x} = -N_X/2+1, ..., N_X/2$. Here we have suppressed the n_ω-dependency. For the T-FT, n_x appearing in the exponential function above must be replaced according to equation (3-A-9) by $n_x \cdot \alpha$, where $\alpha = 2n_\omega/N_T$. Inserting into (3-A-11) yields

$$U(n_{k_x}) = \sum_{n_x=-N_X/2+1}^{N_X/2} \tilde{U}(n_x) \exp\left(-i\frac{2\pi n_{k_x} \cdot n_x}{N_X} \cdot \alpha\right), \tag{3-A-12}$$

for $n_{k_x} = -N_X/2+1, ..., N_X/2$. This expression is known as the fractional Fourier transform. Noting that

$$-2n_{k_x} \cdot n_x = (n_{k_x} - n_x)^2 - (n_{k_x})^2 - (n_x)^2 \tag{3-A-13}$$

the expression for the fractional Fourier transform becomes

$$U(n_{k_x}) = \exp\left(-i\frac{\pi (n_{k_x})^2}{N_X} \cdot \alpha\right) \tag{3-A-14}$$

$$\sum_{n_x=-N_X/2+1}^{N_X/2} \left\{\tilde{U}(n_x) \exp\left(-i\frac{\pi (n_x)^2}{N_X} \cdot \alpha\right)\right\} \exp\left(i\frac{\pi (n_{k_x} - n_x)^2}{N_X} \cdot \alpha\right),$$

for $n_{k_x} = -N_X/2+1, ..., N_X/2$. The sum is recognized as a convolution between two functions: the one inside the curly brackets and the exponential function. The convolution most efficiently is implemented by Fourier transforming the two functions, multiplying their Fourier transforms, before applying an inverse Fourier transform. Then the convolution expression is multiplied by the exponential function in front of the sum sign to obtain the triangle Fourier transform of the seismic data. All Fourier transforms are computed, of course, by FFTs.

References

Allnor R, Caiti A and Arntsen B 1997 Inversion of seismic surface waves for shear wave velocities *Expanded Abstracts, 67th Ann. Internat. Mtg., Soc. Expl.*

Amundsen L and Reitan A 1995a Decomposition of multicomponent seafloor data into upgoing and downgoing P- and S-waves *Geophysics* **60** 563-572

Amundsen L and Reitan A 1995b Extraction of P- and S-waves from the vertical component of particle velocity at the seafloor *Geophysics* **60** 231-240

Amundsen L and Reitan A 1995c Short Note: Estimation of seafloor wave velocities and density from pressure and particle velocity by AVO analysis *Geophysics* **60** 1575-1578

Averbuch A, Coifman R, Donoho D L and Israeli M 2003 Fast slant stack: a notion of Radon transform for data in a Cartesian grid which is rapidly computible, algebraically exact, geometrically faithful and invertible *http://students.som.yale.edu/phd/jpw29/fastradon042001.pdf*

Bailey D H and Swarztrauber P N 1991 The fractional Fourier transforms and applications *SIAM Review*

Berkhout A J 1987 Applied seismic wave theory *Elesvier Science Publ. Co. Inc.*

Chapman N R, Levy S, Cabrera J, Stinson K, and Oldenburg D W 1986 The estimation of the density, P-wave, and S-wave speeds of the topmost layer of sediments, from water bottom reflection arrivals *Akal T and Berkson J M, Eds, Ocean seismo-acoustics: Plenum Press* 703-710

Chapman N R and Rohr K 1991 Measurement of the elastic properties of the ocean bottom by inversion of reflection amplitude data *Hovem J M, Richardson M D and Stoll R D, Eds, Shear Waves in Marine Sediments: Kluwer Acad. Publ.* 537-544

Ikelle L T and Amundsen L 2005 *Introduction to petroleum seismology* (Society of Exploration Geophysics)

Kim N W and Seriff A J 1992 Marine P-S-S-P reflections with a bottom velocity transition zone *Geophysics* **57** 161-170

Mersereau R M and Oppenheim A V 1974 Digital reconstruction of multidimensional signals from their projections *Proc. IEEE* **62** 1319-1338

Muijs R, Robertsson J O A, Curtis A and Holliger K 2003 Near-surface seismic properties for elastic wavefield decomposition: Estimates based on multicomponent land and seabed recordings *Geophysics* **68** 2073-2081

Muijs R, Robertsson J O A and Holliger K 2004 Data-drived adaptive decomposition of multicomponent seabed recordings *Geophysics* **69** 1329-1337

Muyzert E 2000 Scholte wave velocity inversion for a near surface S-velocity model and p-s statics *Expanded Abstracts, 70th Ann. Internat. Mtg., Soc. Expl.*

Schalkwijk K M, Wapenaar C P A and Verschuur D J 2003 Adaptive decomposition of multicomponent ocean-bottom seismic into downgoing and upgoing P- and S-waves *Geophysics* **68** 1091-1102

Schmidt H and Jensen F B 1986 Evaluation of experimental techniques for determining the plane wave reflection coefficient at the sea floor *Akal T and Berkson J M, Eds, Ocean seismo-acoustics: Plenum Press* 721-730

Tatham R H and Goolsbee D V 1984 Separation of S-wave and P-wave reflections offshore Western Florida *Geophysics* **49** 493-508

Chapter 4

Data-driven inversion/depth imaging derived from approximations to one-dimensional inverse acoustic scattering

Abstract

This paper presents a new mathematical framework based on inverse scattering for the estimation of the scattering potential and its nature of a one-dimensional acoustic layered medium from single scattering data. Given the Born potential associated with constant-velocity imaging of the single scattering data, a closed-form, implicit expression for the scattering potential is derived in the WKBJ and eikonal approximations. Adding physical insight, the WKBJ and eikonal solutions can be adjusted so that they conform to the geometrically-derived precise solutions of the one-dimensional scattering problem recently suggested by the authors.

In a layered medium the WKBJ and eikonal approximations, in addition to providing an implicit solution for the scattering potential, provide an explicit estimate of the potential, not within the actual potential discontinuities (layer interfaces), but within the Born potential discontinuities derived by the constant velocity imaging. This estimate of the potential is

called the “squeezed” potential since it mimics the actual potential when the depth axis is squeezed so that the discontinuities of the actual potential match those of the Born potential. It is shown that the squeezed potential can be estimated by amplitude-scaling the Born potential by an amplitude function of the Born potential. The accessibility of the squeezed potential makes the inverse acoustic scattering problem explicit and non-iterative since the estimated squeezed potential can non-linearly be stretched with respect to the depth axis so that the potential discontinuities are moved towards their correct depth location. The non-linear stretch function is a function of the Born potential. The solution is fully data-driven in the respect that no information of the medium other than the Born potential is required.

4.1 Introduction

Scattering is an important tool in studying the structure and dynamics of matter and is used in many disciplines of the physical, mathematical and engineering sciences as an investigative probe. The fields of application are numerous, and diverse as quantum physics, nuclear physics, classical physics like elasticity, acoustics, electromagnetics, geophysics, to electrical engineering and medical imaging. In all these fields scattering theory is used in one form or another to extract information about the system under investigation. Forward scattering involves determining the scattered field when the scattering potential is known. The inverse scattering problem, on the other hand, is the reverse: from the measured scattered field satisfying certain boundary conditions, determine the scattering potential. Whereas forward scattering is quite well understood, the inverse scattering problem still attracts attention in many major branches of science and engineering. The common thread underlying every inverse scattering problem, irrespective of the field of application, is the requirement of a *procedure* that identifies from the scattering data the properties of the scattering potential.

Scattering of acoustic waves has undergone a long development. The literature on acoustic scattering is extensive, and reference is made to Morse and Ingard (1968) and Gladwell (1993) and references therein. The problems in the field of acoustics are closely allied to those in elasticity and seismology, in particular. The research on inverse acoustic back scattering (reflection seismic) reached a new height when Weglein and coworkers in a series of papers [Weglein *et al* (2000, 2002, 2003), Innanen (2003), Innanen and Weglein (2003), Shaw *et al* (2004), Shaw (2005), Zhang *et al* (2005), and Liu *et al* (2005)] described a general approach to the problem of inversely reconstructing the potential. The potential to be recovered is expanded in a series, each term of which is determined in terms of the scattering data and a reference Green's function. The approach requires no prior information about the subsurface medium parameters. Further, Weglein and coworkers show the validity of the concept of "subseries" within the expansion of the potential, where each subseries is associated with a specific inversion task that can be carried out separately. The four subseries associated with the inversion process are: (1) Free-surface related multiple removal, (2) internal multiple attenuation or elimination, (3) spatial location of reflectors in the subsurface (depth imaging), and (4) identification of changes in medium properties across reflectors (inversion). The two last subseries work on primaries, that is, those events in the data that have experienced a single upward reflection in the subsurface. When all multiples, which is seismic energy which has been reflected more than once, have been eliminated from the reflection data, one is left with primaries. The primaries are those reflection events that are used to determine the locations and properties (contrast in wave velocities) of the reflector that caused their observation (recording at the surface).

The inverse scattering problem to be analyzed in the present paper is limited to that of processing primaries, or equivalently, single scattering events. As any data from a layered medium will contain both primaries and multiples, data have to go through a preprocessing step to remove all types of multiples before applying the proposed inversion/depth imaging steps to be presented. The preprocessing is in agreement with the standard practice to seek to attenuate all multiples from seismic data before using primaries for imaging changes in the medium's properties. [see, e.g., Claerbout (1971), Berkhout (1982), Weglein (1985), Stolt and Benson (1986), and Ikelle and Amundsen (2005)]. The historical evolution and development of seismic processing and inversion explain the motivation for addressing the inverse acoustic scattering problem as that of inverting primaries. On its own, the single scattering model in a layered medium is an idealization realized only when the incident wave from the distant source is scattered only once at each interface in the medium. One therefore could be lead to think that the single scattering model should only be used when the medium changes slowly with depth with no strong discontinuities of the medium parameters. However, the realization is within practical reach with the use of new methods which have been developed to attenuate and eliminate internal multiples (Weglein *et al* (1997), and Ramirez and Weglein (2005)).

The inverse scattering series is exact (Weglein *et al* (2003)). Although all developments based on the inverse scattering series have been very useful for the processing and interpretation of seismic data, it turns out nevertheless to be extremely challenging to identify all high-order terms related to the subseries for imaging primaries at depth, also for the case of an one-dimensional (1D) layered medium. Even though work is in progress to extend the depth imaging and inversion capability of the inverse scattering series (see, e.g., Innanen, 2003; Innanen and Weglein, 2003), the current depth imaging scheme is based on what is called leading-order inverse scattering. As a response to this challenge, influenced by the leading-order closed-form 1D depth imaging/inversion algorithms described by Shaw *et al* (2003) and Innanen (2003), Amundsen *et al* (2005) suggested a closed-form solution of the 1D inverse scattering problem that is precise when the product of reflection coefficients from any three interfaces of the medium is negligible compared to the reflection coefficients themselves. The solution was found from physical intuition and geometrical observations of the relationship between the actual potential and the "Born potential" associated with constant-velocity imaging of the single scattering data. The solution, however, was not founded on a firm mathematical-physics framework, which is essential and required for extending the solution for the 1D acoustic medium to multidimensional acoustic and elastic stratified media. It is our objective in the present paper to give the mathematical-physics framework for 1D inverse acoustic (or seismic) scattering problem for layered media where velocities are generally discontinuous at layer interfaces. Once the framework is established for 1D acoustic scattering, it will be the fundament required for extension to multidimensional stratified media.

It is well appreciated in physics that approximations play an important role in the understanding of processes that cannot analytically be solved exactly. Depth imaging derived from the inverse scattering series, for 1D media, contains an infinite number of terms of which many, based on physical insight, are neglected to give useful and practical algorithms for imaging (Innanen 2003, and Shaw *et al* 2004). Realizing that approximations are inevitable at some stage in the inverse scattering series, one is lead to ask: building on the tremendous achievements already obtained by inverse scattering series analysis, can we achieve added understanding of the inverse scattering problem if approximations are introduced into the forward scattering model instead of the inverse scattering series? This is the line of action we take in the present work to investigate what kind of inverse solutions can be obtained. We remark that our mathematical-physics framework for the inverse scattering problem does not make explicit use of the inverse scattering series introduced in exploration seismology by Weglein *et al* (2003). Instead, our approach is to attempt a direct inversion of the forward scattering formula.

The approximations we invoke in the forward scattering model are the WKBJ, eikonal, and Born approximations. The WKBJ approximation has its name after Wentzel, Kramers and Brillouin, who independently introduced it in quantum mechanics in 1926, and Jeffreys, who contributed to its development in 1923. The WKBJ approximation is also known as the WKB approximation or the BWK approximation, depending on the number of contributors that are mentioned in which order, or also as the *classical approximation* or the *phase integral method*. For example, this approximation has been widely used in atomic physics. We refer to the textbook by Schiff (1955 and later editions) for a description of the physical basis and applications of this method. Other general references on the WKBJ approximation are Morse and Feshbach (1953), Fröman and Fröman (1965), Bender and Orszag (1978), and Bransden and Joachain (1989). Some references related to geophysical applications of the WKBJ approximation are Bremmer (1951), Aki and Richards (1980), Clayton and Stolt (1981), Robinson (1982, 1986), Bleistein (1984), Ursin (1984, 1987), and Amundsen (1994). To the eikonal approximation (from $\epsilon\iota\kappa\omega\nu$ = image) there is, in our opinion, no better introduction than that of Glauber (1959) in his 1958 Boulder lectures. By an extension of the method to scattering problems beyond those that are described by a potential, the so-called Glauber approximation or assumption of phase additivity, this method was used extensively in the 1960's and 1970's for elementary particle scattering on nuclei, and also for electron scattering on atoms. In fact, one of the present authors contributed to these developments, see *e.g.* Reitan (1979).

The Born approximation is, of course, so widely used in many branches of the sciences that it need here only be mentioned for the sake of completeness. In inverse scattering the Born approximation is recognized as an important practical tool as long as all scattering involves a single interaction of the probe wavefield with the target. In the nomenclature of reflection seismic, the Born approximation accounts for primary reflections from the subsurface. In scattering studies, the actual medium is divided into a reference medium and a scattering potential that characterizes the difference between the actual and reference media. In a general sense, the Born approximation is known to be good as long as the product of the range of the scattering potential and its average strength is small.

Even though it is well known that the key to a successful application of the Born approximation is that the reference medium must be selected or estimated accurately enough to capture all the long-wavelength information contained in the actual medium, a convenient choice of reference medium is, still, that of a homogeneous one. One reason for the latter choice is that the reference response of a homogeneous medium is known analytically. However, inverse scattering imaging based on a homogeneous reference medium is known to produce incorrect results. The related Born image potential can be far from the actual potential, both in amplitude and positioning of discontinuities. In this paper, where we consider single scattering, it turns out, nevertheless, very convenient as a first step towards the inverse solution to express the imaging of the primaries through the Born potential.

The full inverse scattering problem of seismic, viewed as a three-dimensional (3D) problem, is one of the most challenging problems of geophysics and mathematical physics. In this paper, therefore, we shall be concerned with 1D inverse acoustic single scattering from layered media. One-dimensional models, although they severely restrict or idealize the system under consideration, when treated rigorously they are rich, intricate and involve many deep results from pure mathematics, and need to be understood before dealing with the general 3D models.

The literature on the 1D inverse problem is extensive. Some of the important work in geophysical inversion from the early literature is Goupillaud (1961), Claerbout (1968), Ware and Aki (1968), Razavy (1975), Gjevik *et al* (1976), Koehler and Taner (1977), Nilsen and Gjevik (1978), Berryman and Greene (1980), Burridge (1980), Carroll and Santosa (1981), Coen (1981), Symes (1981), Santosa (1982), Santosa and Schwetlick (1982), Bube and Burridge (1983), and Bruckstein *et al* (1985). The reader may also want to consult the reviews by Newton (1981) and Ursin and Berteussen (1986).

The paper is organized as follows: First, we give a brief review of the forward models for acoustic single scattering in the WKBJ, eikonal and Born approximations. This is used as a mathematical framework for relating the Born potential to the primary reflection response of a layered acoustic medium. In a constant-velocity reference medium, the Born potential is simply obtained by data trace integration, by which the primary reflection events are placed at depths computed linearly only using the constant reference velocity and the travel times of primaries. Next, we derive a closed-form implicit relationship between the Born potential and the potential of the medium in the WKBJ and eikonal approximations. Then we show how the relationship can be made more accurate by conforming it to the geometrical relationship between the Born and WKBJ (eikonal) solutions found by Amundsen *et al* (2005). Instead of embarking on developing an iterative scheme for the estimation of the potential, we develop a closed-form direct solution approach that is data-driven and non-iterative. The data-driven method is split into two steps. From the Born potential itself, we estimate within its layer boundaries what the actual potential would be. In 4.6.2 we show that the estimate is precise for those media where the product of any three reflection coefficients is small compared to the reflection coefficients themselves. Since the layer boundaries are mislocated in the Born potential, this first step obtains good estimates of the amplitude of the actual potential but at wrong depths. What the first step achieves is to provide an amplitude-adjusted, scaled Born potential, which we denote the “squeezed” potential since it mimics the actual potential when the depth axis is squeezed. The second step focuses on the mispositioning in depth of the reflectors. From the estimated squeezed potential we show in the WKBJ approximation that the reflectors can be moved with high precision towards their correct spatial location. Finally, we construct a simple example to show how the procedures introduced in this paper can be applied to obtain the potential in the WKBJ and eikonal approximations from the Born potential.

4.2 Forward scattering models

We consider a 1D acoustic medium, where the velocity is a function of depth, $c = c(z)$, that is embedded in a homogeneous reference medium with wave velocity c_0. The 1D wave equation for scattering of pressure waves P with angular frequency ω and corresponding wave number $k = \omega/c_0$ in a velocity potential

$$\alpha(z) = 1 - \left(\frac{c_0}{c(z)}\right)^2 \tag{4.1}$$

that characterizes the difference between the reference and actual media, is described by the equation

$$\left[\frac{\mathrm{d}^2}{\mathrm{d}z^2} + k^2 - k^2\alpha(z)\right] P(k, z, z_0) = -s(k)\delta(z - z_0)\,. \tag{4.2}$$

The z-axis is pointing vertically downwards, and the source with strength $s(k)$ is located at $z = z_0$. The forward problem associated with equation (4.2) is stated as follows: Given the potential α, find the solution P that satisfies prescribed boundary conditions. In this section, the forward problem is stated in the WKBJ, eikonal and Born approximations. As is usual in scattering theory, the potential α is assumed to vanish asymptotically, i.e., $\alpha \to 0$ as $z \to \pm\infty$, at which limit the wave function P is merely a plane propagating wave described by $\exp(\pm \mathrm{i}kz)$. We write the solution of equation (4.2) as the sum of a term $P_0(k, z, z_0)$ which is the solution of the wave equation in the homogeneous reference medium, i.e., with no potential, and an additional term $\delta P(k, z, z_0)$ caused by the potential $\alpha(z)$, i.e.,

$$P(k, z, z_0) = P_0(k, z, z_0) + \delta P(k, z, z_0)\,, \tag{4.3}$$

where

$$\left[\frac{\mathrm{d}^2}{\mathrm{d}z^2} + k^2\right] P_0(k, z, z_0) = -s(k)\delta(z - z_0)\,, \tag{4.4}$$

and where the additional pressure δP obeys the differential equation

$$\left[\frac{\mathrm{d}^2}{\mathrm{d}z^2} + k^2\right] \delta P(k, z, z_0) = k^2\alpha(z)P(k, z, z_0)\,. \tag{4.5}$$

Formally, the solution of the differential equation (4.5) for the additional pressure δP can be expressed as the integral equation

$$\delta P(k, z, z_0) = -k^2 \int_{-\infty}^{\infty} \mathrm{d}z'\, g(k, z, z')\alpha(z')P(k, z', z_0)\,, \tag{4.6}$$

where the causal Green function in free space

$$g(k, z, z') = -\frac{1}{2\mathrm{i}k}\exp(\mathrm{i}k|z' - z|) \tag{4.7}$$

is a solution of the scattering-free problem

$$\left[\frac{\mathrm{d}^2}{\mathrm{d}z^2} + k^2\right] g(k, z, z') = -\delta(z - z')\,. \tag{4.8}$$

The incident wave due to the point source at z_0 is

$$P_0(k, z, z_0) = s(k)g(k, z, z_0) = S(k)\exp(\mathrm{i}k|z_0 - z|)\,, \tag{4.9}$$

where $S(k) = (\mathrm{i}/2k)s(k)$ is the initial wavefield from the source. When the source is located at $z_0 = 0$ the incident wave becomes

$$P_0(k, z, 0) \equiv P_0(k, z) = S(k)\exp(\mathrm{i}kz)\,. \tag{4.10}$$

The Green function entering the expression (4.6) for the additional pressure $\delta P(k, z) \equiv \delta P(k, z, 0)$ is $g(k, z, z')$ with $z' > z$, so that

$$\delta P(k, z) = F(k)\exp(-\mathrm{i}kz)\,, \tag{4.11}$$

where $F(k)$ is the scattering amplitude. We have

$$F(k) = -\frac{\mathrm{i}k}{2}\int_{-\infty}^{\infty} \mathrm{d}z'\, \exp(\mathrm{i}kz')\alpha(z')P(k, z')\,, \tag{4.12}$$

where $P(k, z) \equiv P(k, z, 0)$. When the receiver is located at $z = 0$ the scattering amplitude is identical to the scattered data,

$$F(k) = \delta P(k, z = 0)\,. \tag{4.13}$$

4.2.1 The scattering amplitude

It is convenient to introduce the dimensionless scattering amplitude

$$\Phi(k) = \frac{F(k)}{S(k)}\,, \tag{4.14}$$

and write the expression for $\Phi(k)$ in a form reminiscent of a quantum mechanical matrix element,

$$\Phi(k) = -\frac{\mathrm{i}k}{2}\int_{-\infty}^{\infty} \mathrm{d}z\, \psi_{\mathrm{f}}^{*}(z)\alpha(z)\psi_{\mathrm{i}}(z)\,, \tag{4.15}$$

where

$$\psi_{\mathrm{i}}(z) = \frac{P(k, z)}{S(k)}\,. \tag{4.16}$$

In the absence of the potential α the initial and final states ψ_{i} and ψ_{f} are given by the expressions

$$\psi_{\mathrm{i}0}(z) = \psi_{\mathrm{f}0}^{\star}(z) = \exp(\mathrm{i}kz)\,. \tag{4.17}$$

Introducing the so-called complex phase shift function $\chi(z)$ we write the actual states as

$$\psi_{\mathrm{i}}(z) = \psi_{\mathrm{f}}^{\star}(z) = \psi_{\mathrm{i}0}(z)\exp[\mathrm{i}\chi(z)]\,, \tag{4.18}$$

and equation (4.15) becomes

$$\Phi(k) = -\frac{\mathrm{i}k}{2}\int_{-\infty}^{\infty}\mathrm{d}z\,\exp(2\mathrm{i}kz)\alpha(z)\exp[2\mathrm{i}\chi(z)]\,. \tag{4.19}$$

The influence of the potential $\alpha(z)$ on the wave functions $\psi_{\mathrm{i}}(z)$ and $\psi_{\mathrm{f}}(z)$ is thus contained in the phase shift function $\chi(z)$. Since the scattered wave ψ_{f} travels through the same potential $\alpha(z)$ as the incident wave ψ_{i} the phase shift function is the same for both cases. Writing ψ_{i} and $\psi_{\mathrm{f}}^{\star}$ in the form (4.18) is, so far, just a matter of convenience. The physical basis for this choice and various approximations to the phase shift function χ are considered in the next section.

4.2.2 The phase shift function

In this section we present three different approximations to the phase shift function $\chi(z)$ which appears in the expressions (4.18) for the wave functions $\psi_{\mathrm{i}}(z)$ and $\psi_{\mathrm{f}}(z)$. These are the Born, WKBJ and eikonal approximation, respectively.

Differential equations

In accordance with (4.2) the wave function (4.18) for the initial state obeys the differential equation

$$\left[\frac{\mathrm{d}^2}{\mathrm{d}z^2} + k^2 - k^2\alpha(z)\right]\psi_{\mathrm{i}}(z) = 0\,. \tag{4.20}$$

Factorizing ψ_{i} in the form

$$\psi_{\mathrm{i}}(z) = \psi_{\mathrm{i}0}(z)\phi(z) = \exp(\mathrm{i}kz)\phi(z) \tag{4.21}$$

we get the differential equation

$$\left[\frac{\mathrm{d}^2}{\mathrm{d}z^2} + 2\mathrm{i}k\frac{\mathrm{d}}{\mathrm{d}z} - k^2\alpha(z)\right]\phi(z) = 0 \tag{4.22}$$

for the function $\phi(z)$.

In terms of the phase shift function $\chi(z)$ we write

$$\phi(z) = \exp[\mathrm{i}\chi(z)]\,, \tag{4.23}$$

where the differential equation for $\chi(z)$ becomes

$$\mathrm{i}\frac{\mathrm{d}^2\chi\mathrm{x}(z)}{\mathrm{d}z^2} - 2k\frac{\mathrm{d}\chi\mathrm{x}(z)}{\mathrm{d}z} - \left(\frac{\mathrm{d}\chi\mathrm{x}(z)}{\mathrm{d}z}\right)^2 - k^2\alpha(z) = 0\,. \tag{4.24}$$

The Born approximation

In the Born approximation the exact pressure wave (4.17) is replaced by the incident wave (4.18) in the expression (4.15) for the scattering amplitude, which means that the function $\phi(z)$ defined in equation (4.21) is

$$\phi_{\mathrm{B}}(z) \equiv 1\,, \tag{4.25}$$

the corresponding phase shift function being

$$\chi_{\mathrm{B}}(z) \equiv 0\,. \tag{4.26}$$

The WKBJ approximation

We separate the real and imaginary part of $\chi(z)$,

$$\chi(z) = \chi_{\mathrm{R}}(z) + \mathrm{i}\chi_{\mathrm{I}}(z)\,. \tag{4.27}$$

According to equation (4.24) we then, for a real potential $\alpha(z)$, obtain the coupled differential equations

$$\begin{aligned} \chi_{\mathrm{I}}'' + 2k\chi_{\mathrm{R}}' + (\chi_{\mathrm{R}}')^2 - (\chi_{\mathrm{I}}')^2 + k^2\alpha = 0\,, \\ \chi_{\mathrm{R}}'' - 2k\chi_{\mathrm{I}}' - 2\chi_{\mathrm{R}}'\chi_{\mathrm{I}}' = 0\,, \end{aligned} \tag{4.28}$$

where the primes denote differentiation with respect to z. On the assumption that the phase shift function varies slowly over a wavelength we can disregard the second derivatives in the equations (4.28) and put $\chi_{\mathrm{I}}(z) \equiv 0$. The first equation (4.28) becomes

$$2k\chi_{\mathrm{R}}' + (\chi_{\mathrm{R}}')^2 + k^2\alpha = 0\,, \tag{4.29}$$

where the physically acceptable root for the derivative $\chi'_{\mathrm{R}} \equiv \chi'_{\mathrm{W}}$ of the phase shift function is

$$\chi'_{\mathrm{W}}(z) = k \left\{ [1 - \alpha(z)]^{\frac{1}{2}} - 1 \right\} . \tag{4.30}$$

In the WKBJ approximation the phase shift function is thus

$$\chi_{\mathrm{W}}(z) = k \int_{-\infty}^{z} \mathrm{d}z' \left\{ [1 - \alpha(z')]^{\frac{1}{2}} - 1 \right\} , \tag{4.31}$$

where it is assumed that $\alpha(z') < 1$ for all $z' < z$.

Alternatively, we can base the present approximation upon the concept of a local wavenumber $k_{\mathrm{local}}(z)$, where in accordance with equation (4.20),

$$k^2_{\mathrm{local}}(z) = k^2 - k^2\,\alpha(z) . \tag{4.32}$$

It is convenient to express the WKBJ phase shift function χ_{W} in equation (4.31) in terms of the WKBJ shift function ξ_{W} in the following way:

$$\chi_{\mathrm{W}}(k, z) = -k\xi_{\mathrm{W}}(z). \tag{4.33}$$

The WKBJ shift function obeys

$$\xi''_{\mathrm{W}} = 0 \quad , \quad -2\xi'_{\mathrm{W}} + (\xi'_{\mathrm{W}})^2 + \alpha = 0 , \tag{4.34}$$

so that

$$\xi_{\mathrm{W}}(z) = \int_{-\infty}^{z} \mathrm{d}z' \left[1 - (1 - \alpha(z'))^{\frac{1}{2}} \right] . \tag{4.35}$$

The eikonal approximation

The eikonal approximation is based upon an expansion of the square root in equation (4.31) to first order in the dimensionless potential α. The corresponding phase shift function is then

$$\chi_{\mathrm{E}}(z) = -\frac{k}{2} \int_{-\infty}^{z} \mathrm{d}z'\,\alpha(z') . \tag{4.36}$$

Another way of arriving at the expression (4.36) is to use the differential equation (4.22) for $\phi(z)$ as a starting point. Assuming again a slowly varying deviation from plane-wave behavior, or, equivalently, a weak potential

$\alpha(z)$, we disregard the second derivative and obtain the first-order differential equation

$$\frac{\mathrm{d}\phi(z)}{\mathrm{d}z} = -\frac{\mathrm{i}k}{2}\alpha(z)\phi(z)\,. \tag{4.37}$$

The solution of this is then $\phi(z) = \exp[\mathrm{i}\chi_{\mathrm{E}}(z)]$, with a phase shift function $\chi_{\mathrm{E}}(z)$ as given by (4.36).

As for the WKBJ approximation, it is convenient to express the phase shift function χ_{E} in equation (4.36) in terms of the eikonal shift function ξ_{E} according to

$$\chi_{\mathrm{E}}(k, z) = -k\xi_{\mathrm{E}}(z)\,, \tag{4.38}$$

so that

$$\xi_{\mathrm{E}}(z) = \frac{1}{2}\int_{-\infty}^{z} \mathrm{d}z'\,\alpha(z')\,. \tag{4.39}$$

4.2.3 The single scattering forward model

Equation (4.19) is a non-linear forward model for computing the dimensionless single scattering amplitude $\Phi(k)$ from the potential α. Replacing the phase shift function by the shift function, $\chi = -k\xi$, gives the forward single scattering model

$$\Phi(k) = -\frac{\mathrm{i}k}{2}\int_{-\infty}^{\infty} \mathrm{d}z\,\alpha(z)\exp[2\mathrm{i}k(z - \xi(z))]\,. \tag{4.40}$$

The WKBJ, eikonal and Born approximations are obtained by choosing $\xi = \xi_{\mathrm{W}}$, $\xi = \xi_{\mathrm{E}}$, and $\xi = 0$, respectively.

We make the following remarks. The single scattering amplitude is found by performing an integral over depth over the product of an amplitude function and a delay function. The amplitude function is the scattering potential. The delay function consist of the product of two functions, where the first $\exp(2\mathrm{i}kz)$ accounts for two-way wave propagation in the reference medium, whereas the second $\exp[-2\mathrm{i}k\xi(z)]$ accounts for the influence of the potential. For a piecewise-constant layered medium the delay function in the WKBJ approximation predicts the exact traveltimes of single scattering events. However, performing the integral over depth, the predicted amplitudes of the single scattering events will not be exact for the piecewise-constant layered medium unless the boundary conditions of continuity of the pressure and the displacement at the interfaces are explicitly introduced. For the sake of forward modeling, the boundary conditions easily can be accounted for. Interfaces or discontinuities in the potential are then treated by correctly coupling the incident wave to the scattered waves. However, for the inverse problem, where the location of interfaces is not known, it would be cumbersome to account for the continuity conditions in an explicit manner. Therefore, we choose to neglect these conditions at the expense of using a forward model that predicts slightly incorrect amplitudes of the single scattering events.

When we later simulate data to test the inverse scattering algorithm to be described in the next section, we do not base the simulation on the single scattering forward model (4.40), but on an exact forward model for primary reflections in a piecewise-constant layered medium. This model is described in Appendix 4.A. The relationship of the forward model (4.40) and that developed in Appendix 4.A with respect to amplitude handling is not discussed further in the present paper. We would like to indicate, however, the WKBJ forward model (4.40) converges to the exact forward model when reflection coefficients of the medium are “small” in the sense that the product of any three of the reflection coefficients is vanishingly small compared to the reflection coefficients.

4.3 Inverse scattering

The inverse scattering problem consists of reconstructing the potential α from the dimensionless scattering amplitude $\Phi(k)$ (the single scattering data measured at depth $z = 0$). In this section we develop a procedure for reconstructing the potential α from the scattering amplitude. The solution is obtained in two steps. First, the Born potential is computed from the scattered field using a constant reference medium. Second, a relationship between the Born potential and the actual potential obtained in the WKBJ approximation is derived. This relationship is used as a basis for introducing a data-driven estimation approach for the potential, requiring no other information than the Born potential itself. The data-driven approach is divided into two computational steps. First, the Born amplitude is adjusted by scaling the Born amplitude by a WKBJ correction amplitude function that is a function of the Born amplitude. We denote this potential the “squeezed” potential since it mimics the actual potential when the depth axis is squeezed. Second, the estimated squeezed potential is non-linearly shifted with respect to the depth axis. The non-linear shift function is a function of the Born potential. Thus, the solution for the potential can be considered obtained by amplitude and shift adjusting the Born potential. No information other than the Born potential is required.

As shown in Appendix 4.F, the inverse Fourier transform over frequency of equation (4.40) yields

$$4\int_{-\infty}^{2z/c_0} dt'\Phi(t') = \sum_{n=0}^{\infty} \frac{1}{n!}\frac{d^n}{\mathrm{d}z^n}\alpha(z)\xi^n(z)\,, \tag{4.41}$$

where $z = c_0 t/2$. Recall that in the Born approximation, the shift function is zero. By considering $\xi = 0$ in the forward model (4.40), and inverse Fourier transforming over frequency, the Born potential, per definition, is obtained:

$$\alpha_{\mathrm{B}}(z) \equiv 4\int_{-\infty}^{2z/c_0} dt'\Phi(t')\,. \tag{4.42}$$

Equation (4.42), which amounts to data trace integration of single scattering events, is known as linear migration-inversion. The primary events are placed at depths computed linearly using their traveltimes together with the constant reference velocity. Thus, the trace integration yields the Born approximation of the scattering potential. Equation (4.41) therefore can be written

$$\alpha_{\mathrm{B}}(z) = \sum_{n=0}^{\infty} \frac{1}{n!}\frac{\mathrm{d}^n}{\mathrm{d}z^n}\alpha(z)\xi^n(z)\,. \tag{4.43}$$

Given the Born potential $\alpha_{\mathrm{B}}(z)$ associated with constant-velocity imaging of single scattering data, our goal is now to use equation (4.43) as the basis for solving the inverse scattering problem in the WKBJ and eikonal approximations.

Observe that equation (4.43), on the left side, contains the Born potential, and on the right side, involves the actual potential. For a layered medium where velocities are generally discontinuous at layer interfaces but constant or slowly varying functions of depth between layer interfaces, any physical solution for the actual potential should not contain more discontinuities (layer interfaces) than the number of discontinuities (layer interfaces) in the Born potential. Before embarking on the inverse solution of equation (4.43) we will use this requirement to guide us towards the form of the inverse acoustic scattering solution in the WKBJ and eikonal approximations.

4.3.1 The form of the inverse solution

To this end, it is instructive to consider plane-wave propagation through a medium with $N + 1$ homogeneous layers with constant layer velocities c_n and thicknesses h_n as shown in figure 4.1. To illustrate the concepts to be introduced, we use the high-velocity contrast piecewise-constant ten-layer ($N = 9$) acoustic 1D medium with velocity $c(z)$ shown in figure 4.2a. The layer depths $z_n = \sum_{j=0}^{n-1} h_j$ and velocities are also listed in table 4.1. The source and receiver are both located at depth $z = 0$ in the zero'th layer which is the reference medium with known velocity c_0. The scattering potential is plotted in figure 4.2b. From equation (4.1) it follows that the potential in layer n is

$$\alpha_n = 1 - \left(\frac{c_0}{c_n}\right)^2 . \tag{4.44}$$

The primary pressure data for this example consist of N reflections. As shown in Appendix 4.A the normalized primary reflection response can be represented as

$$\Phi(t) = \sum_{n=1}^{N} \hat{R}_n \delta(t - t_n) , \tag{4.45}$$

where $\hat{R}_n$, defined in equation (4-A-3), is the amplitude of the reflection event from interface n measured at $z = 0$ at time $t_n = 2 \sum_{j=0}^{n-1} h_j/c_j$, and $\delta(t)$ is the Dirac delta-function. The primary data corresponding to the ten-layer model is shown in figure 4.3.

In imaging in the Born approximation, the first reflector is located at its correct depth, $z_{1\mathrm{B}} = z_1$ since $\alpha(z) = 0$ for $z < z_1$. Using that the Born-estimated thickness of layer n is $h_{n\mathrm{B}} = (c_0/c_n)h_n$, it follows that the depth at which the reference velocity images the nth reflector is $z_{n\mathrm{B}} = c_0 \sum_{j=0}^{n-1} h_j/c_j$.

The depth model that would be obtained from constant-velocity Born imaging is shown in figure 4.4. The Born solution for α is found by substituting the primary reflection response (4.45) into equation (4.19), yielding the Born potential

$$\alpha_{\mathrm{B}}(z) = 4\sum_{n=1}^{N} \hat{R}_n H(z - z_{n\mathrm{B}})\,, \tag{4.46}$$

where $H(z)$ is the Heaviside function. Thus, the Born potential in layer n becomes

$$\alpha_{n\mathrm{B}} = 4\sum_{j=1}^{n} \hat{R}_j = 4\left(R_1 + \sum_{j=2}^{n} R_j \prod_{i=1}^{j-1}(1 - R_i^2)\right)\,. \tag{4.47}$$

For the ten-layer model, the Born potential $\alpha_{\mathrm{B}}(z)$ is shown by the dashed line in figure 4.2c.

Amundsen *et al* (2005) observed that it is possible to non-linearly shift the interfaces of the actual potential $\alpha(z)$ onto the interfaces of the Born potential $\alpha_{\mathrm{B}}(z)$ by the transformation

$$\alpha(z) = \hat{\alpha}\left(z - \int_{-\infty}^{z} \mathrm{d}z' \left[1 - (1 - \alpha(z'))^{\frac{1}{2}}\right]\right)\,. \tag{4.48}$$

Equation (4.48) shows that traversing along the depth axis of the actual potential α, say from depth z_{n-1} to z_n, corresponds to traversing along the depth axis of the shifted potential $\hat{\alpha}$ from depth $z_{n-1,\mathrm{B}}$ to $z_{n\mathrm{B}}$. The depth geometry of $\hat{\alpha}$ is sketched in figure 4.5. Thus, the actual potential α can be shifted in such a way that its layer interfaces coincide with the layer interfaces of the Born potential α_{B}. The shifted potential $\hat{\alpha}$ is called the "squeezed" potential since it appears like the actual velocity potential when the depth axis is squeezed. Note that it is only the layer interfaces that are affected by the squeeze operation. For the ten-layer medium, the squeezed potential $\hat{\alpha}(z)$ is displayed in figure 4.2c together with the Born potential. Observe that the interfaces of $\hat{\alpha}(z)$ and α_{B} match. Inside layer n, the amplitude of $\hat{\alpha}$ equals that of α. The number of interfaces is preserved.

On the other hand, the layer interfaces of the squeezed potential $\hat{\alpha}$ now coinciding with the layer interfaces of the Born potential α_{B} can be restored, that is, "stretched" onto the layer interfaces of the actual potential α, by the transformation

$$\hat{\alpha}(z) = \alpha\left(z + \int_{-\infty}^{z} \mathrm{d}z' \left[(1 - \hat{\alpha}(z'))^{-\frac{1}{2}} - 1\right]\right)\,. \tag{4.49}$$

Figure 4.2d shows that the stretch procedure (4.49) restores the actual potential. The number of interfaces is unaffected. Stated differently, equation (4.49) shows that traversing along the depth axis of $\hat{\alpha}$, say from depth $z_{n-1,\mathrm{B}}$ to $z_{n\mathrm{B}}$, corresponds to traversing along the depth axis of α from depth z_{n-1} to z_n.

In the inverse acoustic scattering problem, however, we have at our disposal the scattering amplitude $\Phi(t)$ from which the Born potential $\alpha_{\mathrm{B}}(z)$ can be computed by trace integration. We have argued that any physical solution for the potential should not contain more discontinuities than the number of discontinuities in the Born potential. Furthermore, we have observed that equation (4.43) on its left side contains the Born potential, and on its right side involves the actual potential. First, consider the Born depth profile (left side of equation (4.43)). When moving from one discontinuity to the next, say from $z_{n-1,\mathrm{B}}$ to $z_{n\mathrm{B}}$ in the Born depth profile, for the number of interfaces to be constant one must move between the corresponding discontinuities z_{n-1} to z_n in the actual depth profile (right side of equation (4.43)). With reference to equation (4.49), this requirement is fulfilled when the Born potential is proportional to

$$\alpha_{\mathrm{B}}(z) \propto \alpha\left(z + \int_{-\infty}^{z} \mathrm{d}z' \left[(1-\hat{\alpha}(z'))^{-\frac{1}{2}} - 1\right]\right) . \tag{4.50}$$

On the right side of equation (4.50), the innermost α-function is the actual potential depth profile squeezed so that its discontinuities coincide with those of the Born depth profile on the left side. While moving along the Born depth profile from discontinuity $z_{n-1,\mathrm{B}}$ to $z_{n\mathrm{B}}$, the integral on the right side stretches the once squeezed potential back to its original position. In this way, the number of discontinuities is preserved. Considering once more equation (4.43), it is obvious that the left and right sides must have equal (or approximately equal, if the WKBJ approximation is invoked) amplitudes. This can be achieved if equation (4.43) involves on its right side an amplitude correction factor A that adjusts the Born potential amplitude to the actual potential amplitude. Since the exact amplitude correction factor must depend on the actual potential, the form of A must contain that of the squeezed potential since the Born potential and the squeezed potential both have discontinuities at the same depths. Thus, with respect to amplitude the Born potential should behave as

$$\alpha_{\mathrm{B}}(z) \propto A^{-1}\left[\hat{\alpha}(z)\right] . \tag{4.51}$$

This form of A ensures that whenever there is a discontinuity of α_{B}, say at depth $z_{n\mathrm{B}}$, there is a discontinuity in A at $z_{n\mathrm{B}}$. The now obvious, but bold guess suggests that the solution of the inverse scattering problem for the layered model should have the form

$$\alpha_{\mathrm{B}}(z) = A^{-1}\left[\hat{\alpha}(z)\right]\alpha\left(z + \int_{-\infty}^{z} \mathrm{d}z' \left[\left(1-\hat{\alpha}(z')\right)^{-\frac{1}{2}} - 1\right]\right) . \qquad (4.52)$$

Thus, knowing $\alpha_{\mathrm{B}}(z)$, the actual potential can be found by stretching the depth axis of the Born potential solution while at the same time applying an amplitude scaling function A that corrects the Born amplitude onto the actual potential amplitude.

The non-trivial challenge is now first to investigate if wave theory in the WKBJ approximation leads to a similar form as that suggested in equation (4.52) for the solution of the potential, and secondly to determine the amplitude function A in the WKBJ approximation. The eikonal approximation follows as a special case by an expansion of the square root in equation (4.52) to first order in the potential α.

4.3.2 WKBJ approximation: implicit solution for potential

We show in Appendix 4.D that by neglecting terms $\mathrm{d}^n\xi/\mathrm{d}z^n$ for $n = 2, ..., \infty$, we can write equation (4.43) as an infinite sum where the nth term is proportional to the nth power of the derivative of the shift function,

$$\alpha_{\mathrm{B}}(z) \approx \sum_{n=0}^{\infty}\left(\frac{\mathrm{d}\xi(z)}{\mathrm{d}z}\right)^{n}\sum_{m=n}^{\infty}\frac{1}{(m-n)!}\left(\begin{array}{c} m \\ n \end{array}\right)\xi^{m-n}(z)\frac{\mathrm{d}^{m-n}\alpha(z)}{\mathrm{d}z^{m-n}} . \qquad (4.53)$$

Equation (4.53) is a basis for deriving a closed-form solution for α as shown in Appendix 4.E. To this end, the Fourier representation of $\alpha(z)$ is introduced, which gives

$$\alpha_{\mathrm{B}}(z) \quad \approx \quad \sum_{n=0}^{\infty}\left(\frac{\mathrm{d}\xi(z)}{\mathrm{d}z}\right)^{n}\frac{1}{2\pi}\int_{-\infty}^{\infty}\mathrm{d}k D_n(k\xi)\exp(-\mathrm{i}kz)\alpha(k) , \qquad (4.54)$$

where

$$D_n(k\xi) = \sum_{m=n}^{\infty}\frac{1}{(m-n)!}\left(\begin{array}{c} m \\ n \end{array}\right)\left[-\mathrm{i}k\xi(z)\right]^{m-n} . \qquad (4.55)$$

The sum D_n can be written

$$D_n(k\xi) = \exp[-\mathrm{i}k\xi(z)] \sum_{m=0}^{n} \frac{1}{m!} \left(\begin{array}{c} n \\ m \end{array} \right) [-\mathrm{i}k\xi(z)]^{n-m} \,, \tag{4.56}$$

and the expression for the Born potential then becomes

$$\alpha_{\mathrm{B}}(z) \approx \\ \frac{1}{2\pi} \int_{-\infty}^{\infty} \mathrm{d}k \left\{ \sum_{n=0}^{\infty} \left(\frac{\mathrm{d}\xi(z)}{\mathrm{d}z} \right)^n \sum_{m=0}^{n} \frac{1}{m!} \left(\begin{array}{c} n \\ m \end{array} \right) [-\mathrm{i}k\xi(z)]^{n-m} \right\} \exp[-\mathrm{i}k(z+\xi(z))]\alpha(k) \,. \tag{4.57}$$

In equation (4.57) the double sum can be written as a single sum that is recognized as an expression for the exponential function,

$$\begin{aligned} \sum_{n=0}^{\infty} \left(\frac{\mathrm{d}\xi(z)}{\mathrm{d}z} \right)^n \sum_{m=0}^{n} \frac{1}{m!} \left(\begin{array}{c} n \\ m \end{array} \right) [-\mathrm{i}k\xi(z)]^{n-m} = \\ \frac{1}{1-\xi'(z)} \sum_{n=0}^{\infty} \frac{(-1)^n}{n!} \left(\frac{\mathrm{i}k\xi(z)\xi'(z)}{1-\xi'(z)} \right)^n \\ = \frac{1}{1-\xi'(z)} \exp\left(-\frac{\mathrm{i}k\xi(z)\xi'(z)}{1-\xi'(z)} \right) \,. \end{aligned} \tag{4.58}$$

The Born potential in equation (4.57) now reads

$$\alpha_{\mathrm{B}}(z) \approx \left(1 - \frac{\mathrm{d}\xi(z)}{\mathrm{d}z} \right)^{-1} \frac{1}{2\pi} \int_{-\infty}^{\infty} \mathrm{d}k \exp\left[-\mathrm{i}k \left(z + \frac{\xi(z)}{1-\xi'(z)} \right) \right] \alpha(k) \,. \tag{4.59}$$

Using the translation property of the Fourier transform, we obtain a closed-form expression for the Born potential,

$$\alpha_{\mathrm{B}}(z) \approx \left(1 - \frac{\mathrm{d}\xi(z)}{\mathrm{d}z} \right)^{-1} \alpha \left(z + \frac{\xi(z)}{1 - \frac{\mathrm{d}\xi(z)}{\mathrm{d}z}} \right) \,. \tag{4.60}$$

However, although close, equation (4.60) is not exactly of the form proposed by equation (4.52). We therefore introduce two new approximations, both which are valid in the WKBJ approximation. First, as shown in Appendix

4.B [see equation (4-B-5)], under the WKBJ assumption that $\xi''(z)$ is negligible, the replacement

$$\frac{\xi(z)}{1-\frac{\mathrm{d}\xi(z)}{\mathrm{d}z}} \to \int_{-\infty}^{z} \mathrm{d}z' \, \frac{\frac{\mathrm{d}\xi(z')}{\mathrm{d}z'}}{1-\frac{\mathrm{d}\xi(z')}{\mathrm{d}z'}} \quad , \quad \xi''(z) = 0 \, , \tag{4.61}$$

is justified. Second, as shown in Appendix 4.B [see equation (4-B-11)], when $\xi''(z)$ and all higher-order derivatives are disregarded, the following replacement is justified:

$$[1-\alpha(z)]^{-\frac{1}{2}} \to [1-\hat{\alpha}(z)]^{-\frac{1}{2}} \quad , \quad \frac{\mathrm{d}^n\xi(z)}{\mathrm{d}z^n} = 0 \quad , \quad n \geq 2 \, . \tag{4.62}$$

Here, $\hat{\alpha}\,(z)$, defined in equation (4.48), represents the actual potential which has layer boundaries at z_n squeezed to new layer boundaries $z_{n\mathrm{B}}$ coinciding with the Born layer boundaries. Inserting the two approximations into equation (4.60) and recalling equation (4.35) give the result

$$\alpha_{\mathrm{B}}(z) \;\; \approx \;\; [1-\hat{\alpha}(z)]^{-\frac{1}{2}} \, \alpha \left(z + \int_{-\infty}^{z} \mathrm{d}z' \, \left[(1-\hat{\alpha}(z'))^{-\frac{1}{2}} - 1 \right] \right) \, , \tag{4.63}$$

which is consistent with the solution form proposed in equation (4.52). Observe that WKBJ theory has provided the form of the amplitude scaling function A that corrects the Born potential amplitude onto the actual potential amplitude:

$$A(z) \;\; \approx \;\; [1-\hat{\alpha}(z)]^{\frac{1}{2}} \, . \tag{4.64}$$

Equation (4.63) is thus the desired inverse scattering solution for the potential α. Since $\hat{\alpha}$ is a function of α (cfr. equation (4.48)), equation (4.63) is an implicit equation for α that can be solved, in principle, by iteration as a data-fitting problem with known α_{B}.

Note that equations (4.42) and (4.63) represent a two-step procedure for obtaining the scattering potential. First, the Born potential α_{B} is computed from the dimensionless scattering amplitude according to equation (4.42). Second, the potential α is solved from equation (4.63). In this paper, we will not embark on the problem of developing an iterative estimation scheme. Instead, we illustrate the difference between equations (4.60) and (4.63), which both are expressions for the Born potential, by computing the Born potential from the actual potential. The results shown in figure 4.6 are in agreement with the discussion above. Observe that α_{B} computed from equation (4.60) gives a reasonable estimate of α_{B} but that the number of interfaces is wrong. On the other hand, equation (4.63) produces an α_{B}-estimate that is quite precise.

4.3.3 WKBJ approximation: data-driven, direct solution for potential

The form of equation (4.63) suggests another possible approach valid for the case that we can predict from WKBJ theory what the actual layer potentials are, not as function of their true depth, but as function of the interface depths provided by the Born potential. Thus, the question we ask is: can we predict $\hat{\alpha}$ from α_{B} by means of WKBJ theory? As stated earlier, the function $\hat{\alpha}(z)$ represents a mapping of layers of the actual potential onto the layers of the Born potential. The amplitudes of this squeezed potential $\hat{\alpha}$ and the actual potential α are the same, and generally different from the Born amplitudes. On the other hand, the locations of discontinuities (layer boundaries) of the squeezed potential $\hat{\alpha}$ and the Born potential α_{B} are the same. Inside a layer, velocities are assumed to vary smoothly with depth. It is then reasonable to disregard all derivatives of α, and the WKBJ approximation, it turns out, leads to an approximate relationship between $\hat{\alpha}$ and α_{B}. The non-zero terms in equation (4.53) arrive for all $n = m$, giving

$$\alpha_{\mathrm{B}}(z) \approx \hat{\alpha}(z) \sum_{n=0}^{\infty} \left[1 - (1 - \hat{\alpha}(z))^{\frac{1}{2}}\right]^{n} \quad , \quad \frac{\mathrm{d}^{n+1}\alpha(z)}{\mathrm{d}z^{n+1}} = 0\,. \tag{4.65}$$

The sum is a geometric series, and we find

$$\alpha_{\mathrm{B}}(z) \approx [1 - \hat{\alpha}(z)]^{-\frac{1}{2}}\hat{\alpha}(z)\,. \tag{4.66}$$

Inversion of equation (4.66) yields the admissible solution

$$\hat{\alpha}(z) \approx \hat{\hat{\alpha}}(z) = \left[\left(1 + \frac{1}{4}\alpha_{\mathrm{B}}^{2}(z)\right)^{\frac{1}{2}} - \frac{1}{2}\alpha_{\mathrm{B}}(z)\right]\alpha_{\mathrm{B}}(z)\,. \tag{4.67}$$

Equation (4.67) shows that once α_{B} has been derived, then the squeezed potential estimate $\hat{\hat{\alpha}}$ can be obtained,

$$\hat{\hat{\alpha}}(z) = A_{\mathrm{W}}(z)\alpha_{\mathrm{B}}(z) \tag{4.68}$$

by multiplying α_{B} by the the WKBJ correction amplitude

$$A_{\mathrm{W}}(z) = \left(1 + \frac{1}{4}\alpha_{\mathrm{B}}^{2}(z)\right)^{\frac{1}{2}} - \frac{1}{2}\alpha_{\mathrm{B}}(z)\,. \tag{4.69}$$

The only information that is required for this estimation is the Born potential itself. In Appendix 4.C we show that relation (4.68) is precise for layered media where the product of reflection coefficients from any three interfaces is negligible compared to the reflection coefficients themselves. Therefore, for such media, equation (4.63) can be re-written in the following form:

$$\hat{\hat{\alpha}}(z) = \alpha\left(z + \int_{-\infty}^{z} \mathrm{d}z' \left[\left(1 - \hat{\hat{\alpha}}(z')\right)^{-\frac{1}{2}} - 1\right]\right)\,. \tag{4.70}$$

Provided that the Born potential has been computed according to equation (4.42), then equation (4.70) suggests a two-step solution for the scattering potential α. First, the Born potential is scaled by the WKBJ correction amplitude (4.69) to find the squeezed potential estimate $\hat{\hat{\alpha}}$. Then the potential α is derived as a non-linear shift of $\hat{\hat{\alpha}}$ according to equation (4.70). The non-linear shift is seen to correspond to stretching the depth axis of the squeezed potential result, $\hat{\hat{\alpha}}$. The effect of shifting is to locate interfaces that are mislocated in $\hat{\hat{\alpha}}$ towards their correct location. Thus, in the absence of the actual velocity function, the scale and shift algorithm extracts the necessary information from the Born depth profile $\alpha_{\mathrm{B}}(z)$.

4.3.4 Eikonal approximation

The eikonal approximation for the scattering potential follows from equation (4.63) and (4.70) by an expansion of the square roots to first order in the potential α. The eikonal approximation data-driven, direct solution corresponding to equation (4.70) is

$$\hat{\hat{\alpha}}(z) = \alpha\left(z + \int_{-\infty}^{z} \mathrm{d}z' \left[\left(1 - \frac{1}{2}\hat{\hat{\alpha}}(z')\right)^{-1} - 1\right]\right)\,, \tag{4.71}$$

in which the squeezed potential estimate $\hat{\hat{\alpha}}$ in the eikonal approximation,

$$\hat{\hat{\alpha}}(z) = A_{\mathrm{E}}(z)\alpha_{\mathrm{B}}(z)\,, \tag{4.72}$$

is obtained by multiplying α_{B} by the eikonal correction amplitude

$$A_{\mathrm{E}}(z) = \left(1 + \frac{1}{2}\alpha_{\mathrm{B}}(z)\right)^{-1} . \tag{4.73}$$

4.4 Model calculations

As an example of data-driven estimation of the scattering potential, we consider once more the high-velocity contrast piecewise-constant ten-layer acoustic medium listed in table 4.1 and displayed in figure 4.2a. The reference velocity is $c_0 = 1500$ m/s. The actual potential is plotted in figure 4.7a. First, single scattering data are computed according to equation (4.45) for infinite bandwidth. The scattered data are displayed in figure 4.3. Second, the Born potential is derived by constant velocity imaging according to equation (4.46). The Born depth profile is shown by the blue line in figure 4.7b. Third, the squeezed potential estimate $\hat{\hat{\alpha}}$ is calculated from the Born potential by use of equation (4.68) for the WKBJ approximation and equation (4.72) for the eikonal approximation. Essentially, $\hat{\hat{\alpha}}$ which for the WKBJ and eikonal cases, respectively, is displayed in red and pink lines in figure 4.7b, is obtained by scaling α_{B} by the the proper correction amplitude, A_{W} or A_{E}.

Now, the actual potential can be estimated in the WKBJ and eikonal approximations simply by stretching the depth axis of the squeezed potential estimate $\hat{\hat{\alpha}}$ according to the formula (4.70) and (4.71), respectively. The WKBJ derived result is shown in figure 4.7c, and the corresponding eikonal derived potential is plotted in figure 4.7d. For the purpose of comparison, the actual potential is re-plotted in black line. As can be expected, for the high velocity contrast example, the WKBJ approximation performs better than the eikonal approximation (which essentially is an approximation to the WKBJ approximation) with respect to estimating the potential discontinuities (layer boundaries). The estimated depths of the potential discontinuities are listed in table 4.1.

As a perhaps more realistic example [1]of data-driven estimation of the scattering potential, we now consider single scattering data with finite bandwidth in the inversion procedure. Again we use the high-velocity contrast piecewise-constant ten-layer acoustic medium listed in table 4.2 and

---

[1] This example is not included in the Inverse Problems paper.

displayed in figure 4.2a as the actual medium. The reference velocity is $c_0 = 1500$ m/s. The actual potential is plotted in figure 4.8a. Instead of considering single scattering data with infinite bandwidth, we now generate synthetic data with finite bandwidth by multiplying the forward model given by (4.45) with a source-wavefield in the frequency domain. The source-wavefield is represented by $S(\omega) = \frac{ic_0}{2\omega}s(\omega)$ where $s(\omega)$ is a Richer wavelet with 1 ms sampling-interval and 50 Hz as dominant frequency. The source-wavefield is then removed from the data by spectral division in the frequency domain. The source-wavelet is displayed in figure 4.9a. The scattered data are displayed in figure 4.9b. The scattered data after removing the source wavelet are displayed in figure 4.9b. Then, the Born potential is derived by constant velocity imaging according to equation (4.46). The Born depth profile is shown by the blue line in figure 4.8b. Next, the squeezed potential estimate $\hat{\hat{\alpha}}$ is calculated from the Born potential by use of equation (4.68) for the WKBJ approximation and equation (4.72) for the eikonal approximation. In figure 4.8b $\hat{\hat{\alpha}}$ is displayed in red and pink lines for the WKBJ and eikonal cases, respectively. $\hat{\hat{\alpha}}$ is obtained by scaling α_{B} by the the proper correction amplitude, A_{W} or A_{E}.

Now, the actual potential can be estimated in the same manner as described above. The WKBJ derived result is shown in figure 4.8c, and the corresponding eikonal derived potential is plotted in figure 4.8d. For the purpose of comparison, the actual potential is re-plotted in black line. As before, the WKBJ approximation performs better than the eikonal approximation with respect to estimating the potential discontinuities (layer boundaries). The estimated depths of the potential discontinuities are listed in table 4.2. The estimated values for this example where we have considered single scattering data with finite bandwidth in the inversion procedure are very similar to the estimated values where we considered single scattering data with infinite bandwidth.

4.5 Future work

In the present paper we have restricted the inverse scattering analysis to 1D (plane-wave normal-incidence) acoustic scattering. However, many of the elements of the inverse scattering theory are general, and extend to higher dimensions as well as to elastic media. Work is in progress to study inverse acoustic and elastic multidimensional single scattering in stratified media and results will be reported as they are obtained (Amundsen *et al* (2006)).

In the practical applications of inverse scattering theory many questions arise, relating for example to the optimum collection of data and to the preprocessing of data. Such questions are being addressed by several university consortia as well as by the seismic contractors and we expect to benefit from their ongoing studies.

4.6 Conclusions

The ultimate objective of inverse scattering is to determine the medium and its properties from measurements external to the object under investigation. We have given a brief review of the forward models for acoustic single scattering from one-dimensional layered media in the WKBJ, eikonal and Born approximations. From the Born potential associated with constant-velocity imaging of the single scattering data, we derived a closed-form, implicit expression for the scattering potential. The inverse scattering solution estimates by iteration the potential by stretching the depth axis of the Born potential solution while at the same time applying an amplitude scaling function that corrects the Born amplitude onto the actual potential amplitude.

For a layered medium we showed that the WKBJ and eikonal approximations, in addition to providing an implicit solution for the scattering potential, provide an explicit estimate of the potential, not within the actual potential discontinuities (layer interfaces), but within the Born potential discontinuities derived by the constant velocity imaging. The estimate is fed directly into the inverse acoustic scattering solution such that the inversion problem becomes fully explicit and non-iterative. Further, this solution is data-driven in the respect that no other information of the medium other than the Born potential is required. The data-driven method is split into two steps. First, within the layer boundaries provided by the Born potential, it is estimated what the squeezed potential would be. Since the layer boundaries are mislocated in the Born potential, this first step obtains accurate estimates of the amplitude of the actual potential but at wrong depths. The amplitude estimation is simply obtained by scaling the Born potential by a function of itself. In the second step the mislocated reflectors in the estimated squeezed potential are moved with high precision towards their correct spatial location by applying a non-linear stretch function that is a function of the Born potential only.

A simple model example showed how the potential could be estimated in the WKBJ and eikonal approximations, given the Born potential. For high-velocity contrast media (strong potential), WKBJ theory gives an inverse scattering procedure that with high precision reconstructs the potential and its nature. The eikonal approximation, which is based upon an expansion of the square root in the WKBJ shift function to first order in the potential, and thus involves a weak-discontinuity potential assumption, does not provide the same precise depth location of layer interfaces as that provided by WKBJ theory for high-contrast velocity media.

Acknowledgments

We thank Statoil ASA for allowing us to publish this work. H. K. H. thanks Statoil for financial support.

Table 4.1: Ten-layer model with reference velocity $c_0 = 1500$ m/s. Here, z_n is the actual layer depth, $z_{n\mathrm{B}}$ is the layer depth from Born constant-velocity imaging, $\hat{z}_{n\mathrm{W}}$ is the estimated layer depth from depth imaging in the WKBJ approximation, $\hat{z}_{n\mathrm{E}}$ is the estimated layer depth from depth imaging in the eikonal approximation, c_n is the actual layer velocity, $\hat{c}_{n\mathrm{W}}$ is the estimated layer velocity in the WKBJ approximation computed according to equation (4-C-8), $\hat{c}_{n\mathrm{E}}$ is the estimated layer velocity in the eikonal approximation computed according to equation (4-C-8), α_n is the actual potential, $\alpha_{n\mathrm{B}}$ is the Born potential, and R_n is the reflection coefficient.

n	$z_n[m]$	$z_{n\mathrm{B}}[m]$	$\hat{z}_{n\mathrm{W}}$[m]	$\hat{z}_{n\mathrm{E}}$[m]	c_n[m/s]	$\hat{c}_{n\mathrm{W}}$[m/s]	$\hat{c}_{n\mathrm{E}}$[m/s]	α_n	$\alpha_{n\mathrm{B}}$	R_n
0					1500	1500	1500	0.00	0.00	
1	300	300	300	300	1900	1894	1906	0.38	0.47	0.118
2	400	378.9	400	397	2000	1989	2013	0.44	0.57	0.026
3	500	453.9	499	494	2100	2082	2123	0.49	0.67	0.024
4	600	525.4	599	590	2200	2174	2237	0.54	0.76	0.023
5	700	593.6	697	684	2600	2523	2759	0.67	1.09	0.083
6	800	651.3	795	773	2300	2266	2359	0.57	0.85	-0.061
7	1000	781.7	991	958	2200	2176	2240	0.54	0.76	-0.022
8	1100	849.9	1090	1052	2400	2353	2484	0.61	0.93	0.043
9	1200	912.4	1189	1144	2500	2438	2616	0.64	1.01	0.020

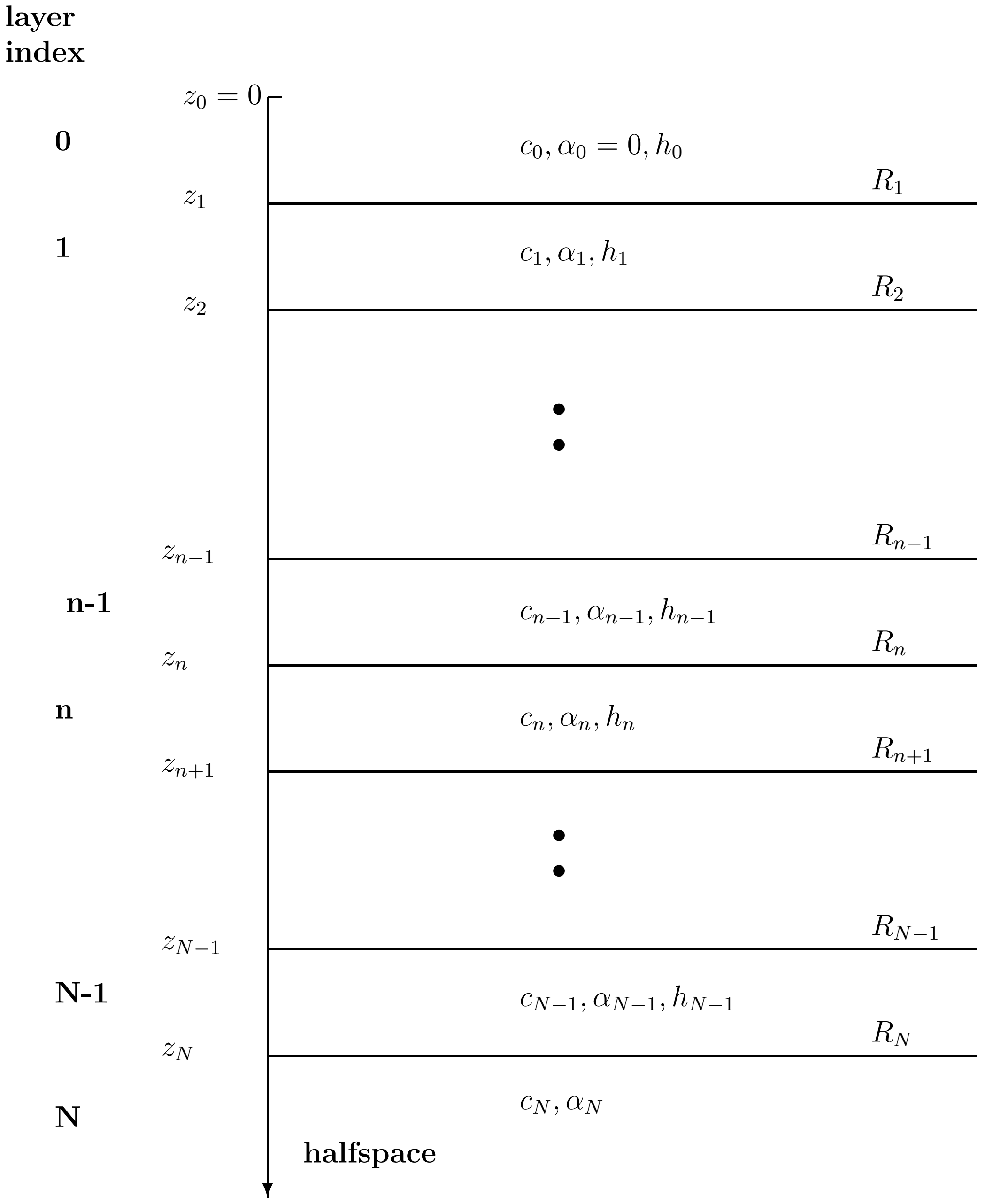

Figure 4.1: Layered medium. The velocity $c(z)$ and potential $\alpha(z)$ are generally discontinuous at layer interfaces $z_1, z_2, ..., z_N$.

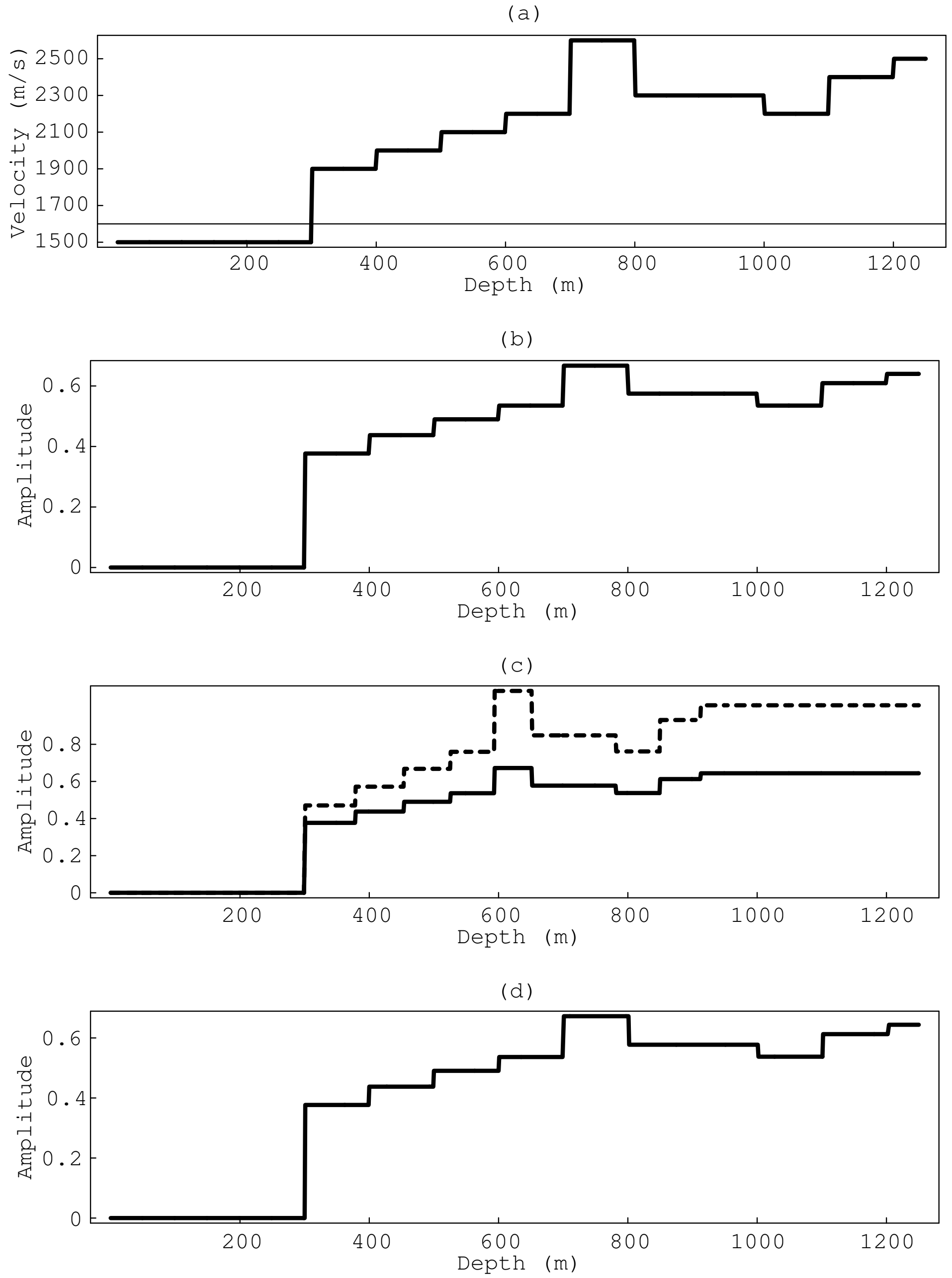

Figure 4.2: “Squeezing” and “stretching” of potentials. (a) The actual velocity model, $c(z)$, which is listed in table 4.1. (b) The actual potential, $\alpha(z)$. (c) Squeezing of the actual potential according to equation (4.48). Comparison of the squeezed potential $\hat{\alpha}$ (solid line) and the Born potential α_{B} (dashed line) shows that the layer boundaries are at identical depths. Note that $\hat{\alpha}$ can be estimated from α_{B} according to equation (4.68). (d) Stretching of the squeezed potential $\hat{\alpha}$ according to equation (4.49) restores the actual potential, α.

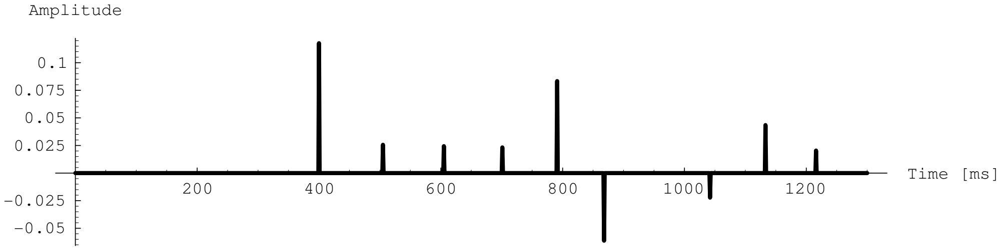

Figure 4.3: Primary reflection events from the ten layer (nine-interface) model in figure 4.2a.

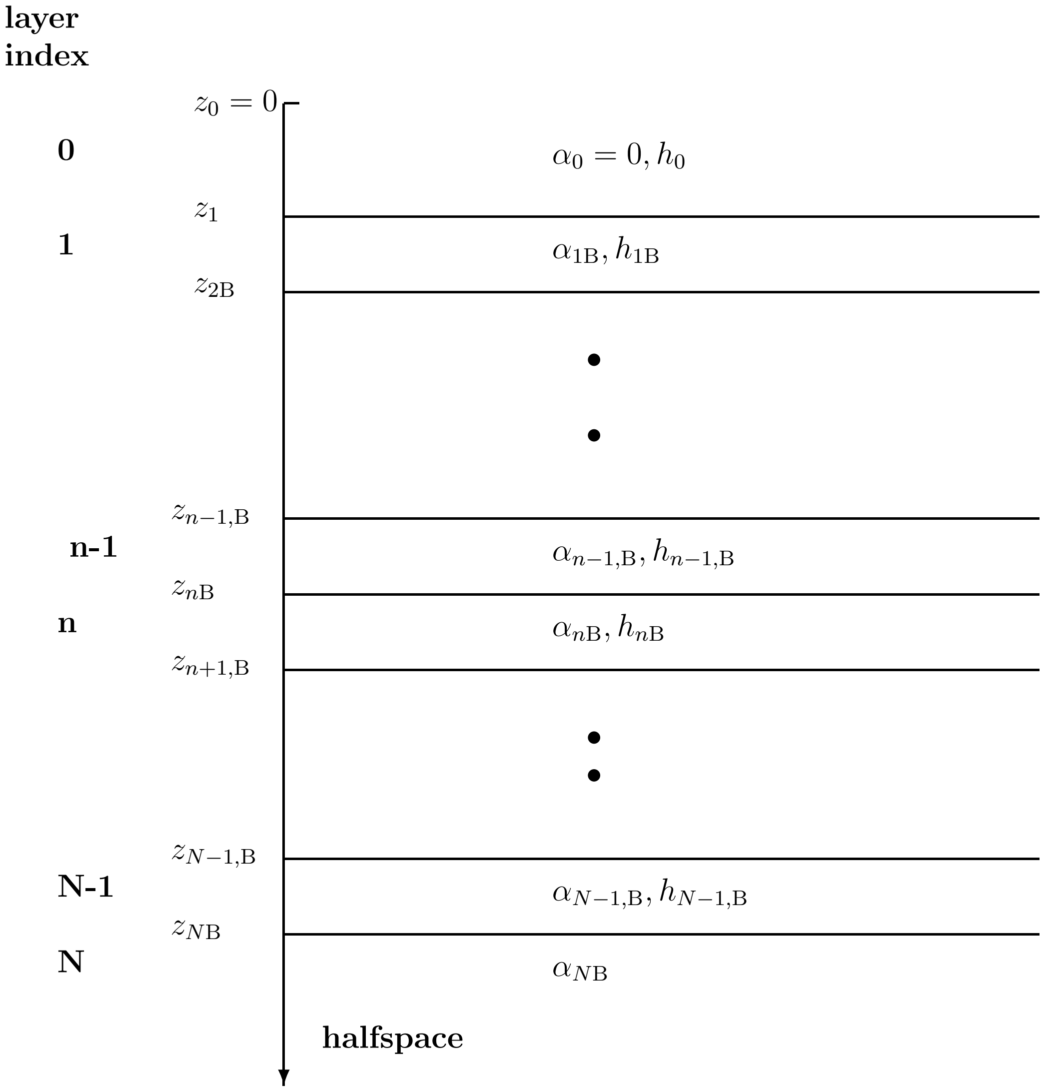

Figure 4.4: Layered medium that would be obtained from Born constant-velocity imaging.

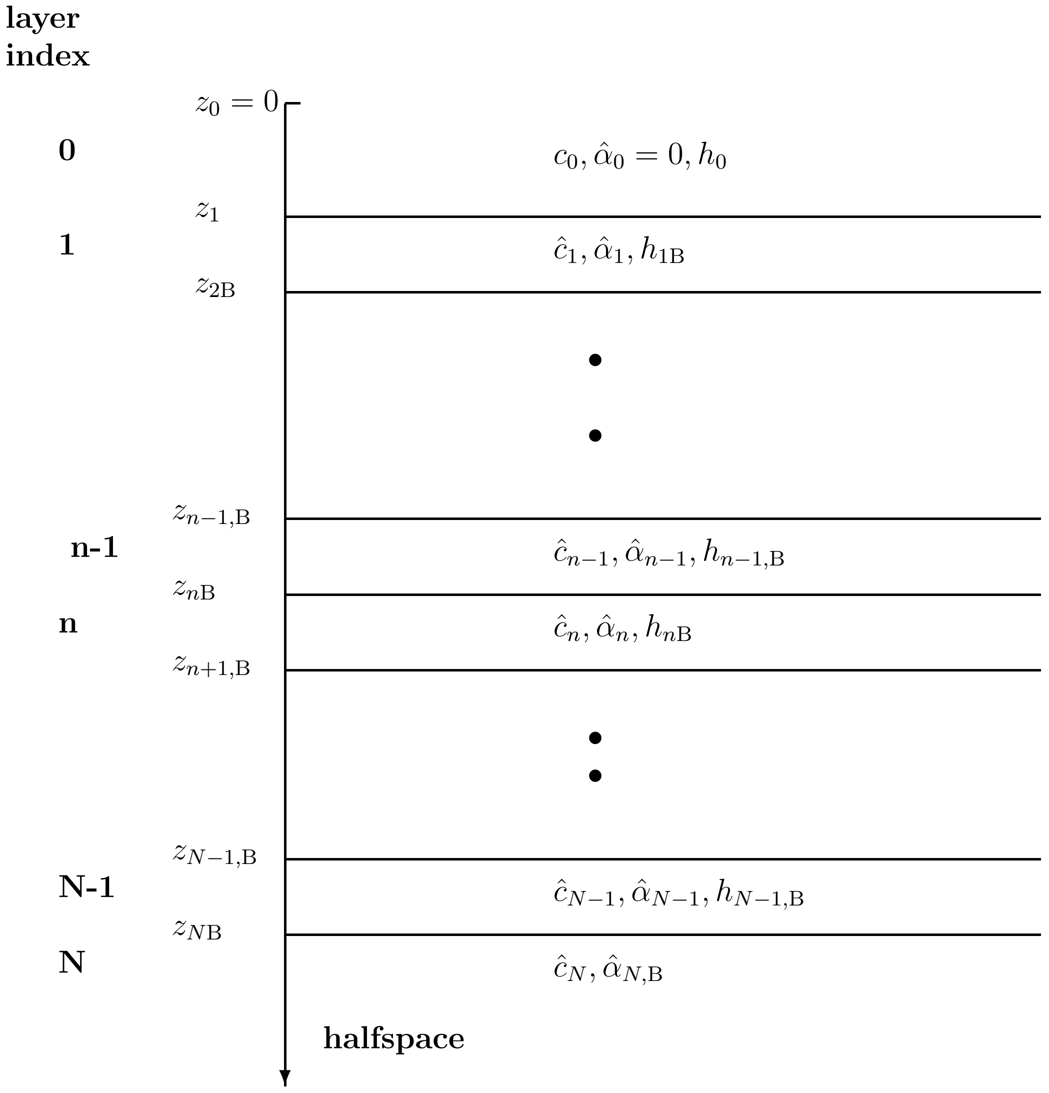

Figure 4.5: The layer boundaries of the "squeezed" potential $\hat{\alpha}$ correspond to those of α_{B} shown in figure 4.4. The amplitudes $\hat{\alpha}_n$ correspond to those of α_n illustrated in figure 4.1. As shown by equation (4.68), $\hat{\alpha}_n$ can be estimated from α_{B}, leading to an estimate of layer velocities $\hat{c}_n$ according to equation (4-C-8).

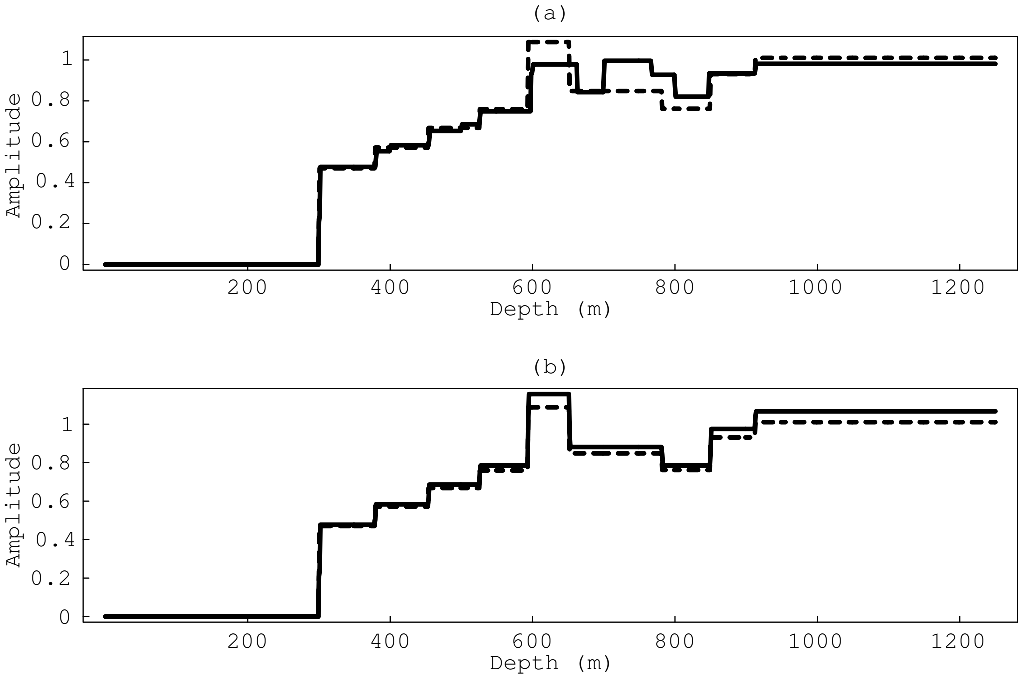

Figure 4.6: Born potential α_{B} estimated (solid lines) from (a) equation (4.60) and (b) equation (4.63). The exact Born potential is displayed in dashed line.

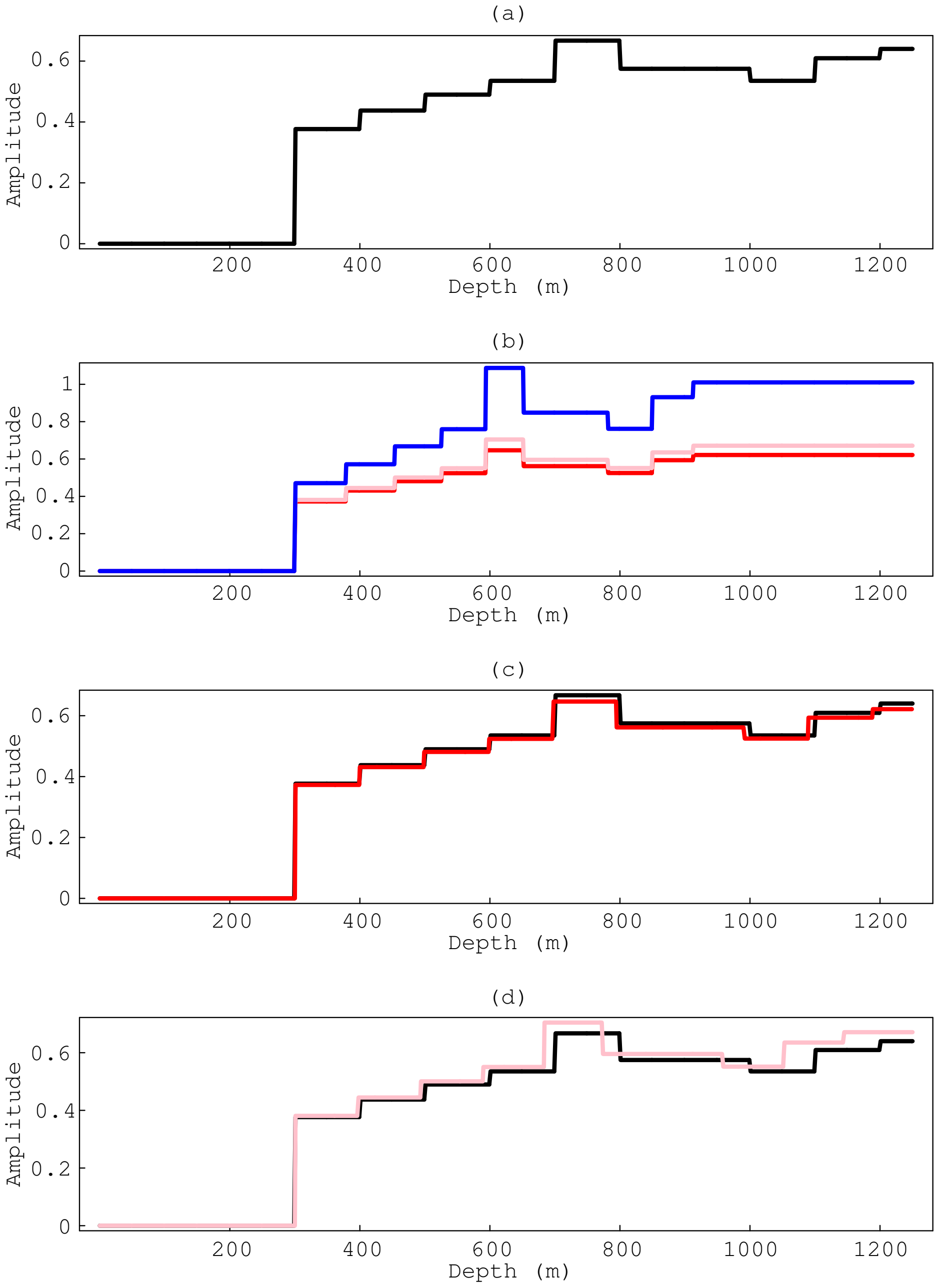

Figure 4.7: (a) The actual scattering potential. (b) The Born (blue line) and estimated squeezed potentials in the WKBJ (red line) and eikonal (pink line) approximations. (c) WKBJ-derived potential (red line) obtained by stretching the squeezed WKBJ potential in (b, red line) compared to the actual potential (black line). (d) Eikonal-derived potential (pink line) obtained by stretching the squeezed eikonal velocity potential in (b, pink line) compared to the actual potential (black line).

Table 4.2: Ten-layer model with reference velocity $c_0 = 1500$ m/s. Here, z_n is the actual layer depth, $z_{n\mathrm{B}}$ is the layer depth from Born constant-velocity imaging, $\hat{z}_{n\mathrm{W}}$ is the estimated layer depth from depth imaging in the WKBJ approximation, $\hat{z}_{n\mathrm{E}}$ is the estimated layer depth from depth imaging in the eikonal approximation, c_n is the actual layer velocity, $\hat{c}_{n\mathrm{W}}$ is the estimated layer velocity in the WKBJ approximation computed according to equation (4-C-8), $\hat{c}_{n\mathrm{E}}$ is the estimated layer velocity in the eikonal approximation computed according to equation (4-C-8), α_n is the actual potential, $\alpha_{n\mathrm{B}}$ is the Born potential, and R_n is the reflection coefficient.

n	$z_n[m]$	$z_{n\mathrm{B}}[m]$	$\hat{z}_{n\mathrm{W}}$[m]	$\hat{z}_{n\mathrm{E}}$[m]	c_n[m/s]	$\hat{c}_{n\mathrm{W}}$[m/s]	$\hat{c}_{n\mathrm{E}}$[m/s]	α_n	$\alpha_{n\mathrm{B}}$	R_n
0	0	0	0	0	1500	1500	1500	0.00	0.00	-
1	300	300.0	300	300	1900	1895	1907	0.38	0.47	0.118
2	400	378.5	400	398	2000	1990	2013	0.44	0.57	0.026
3	500	453.5	499	495	2100	2082	2122	0.49	0.67	0.024
4	600	524.8	599	590	2200	2173	2235	0.54	0.76	0.023
5	700	593.1	697	684	2600	2521	2757	0.67	1.09	0.083
6	800	650.6	795	773	2300	2263	2355	0.57	0.85	-0.061
7	1000	781.1	992	959	2200	2172	2234	0.54	0.76	-0.022
8	1100	849.4	1090	1053	2400	2347	2475	0.61	0.93	0.043
9	1200	911.9	1188	1144	2500	2432	2605	0.64	1.01	0.020

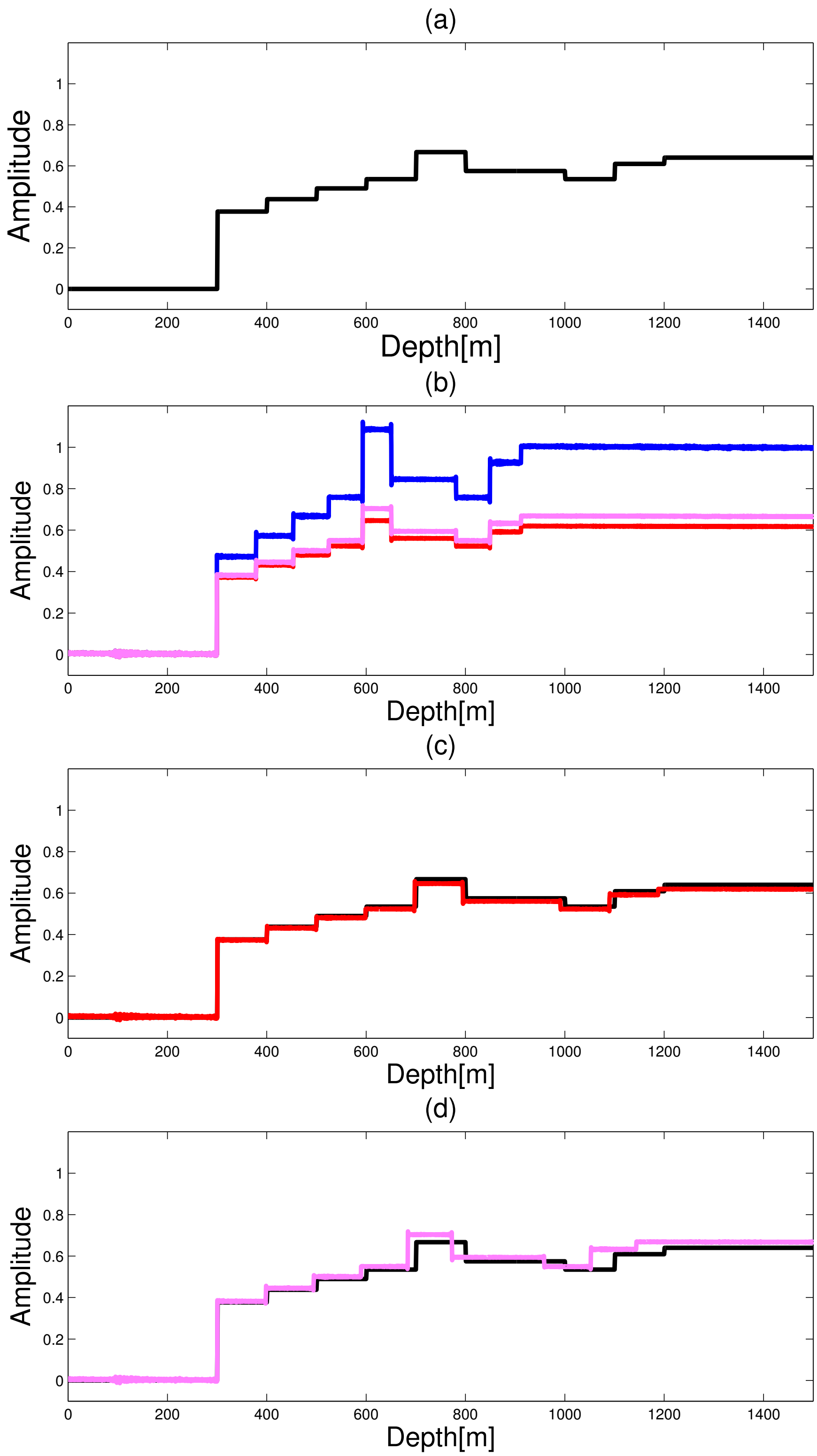

Figure 4.8: (a) The actual scattering potential. (b) The Born (blue line) and estimated squeezed potentials in the WKBJ (red line) and eikonal (pink line) approximations. (c) The WKBJ-derived potential (red line) obtained by stretching the squeezed WKBJ potential in (b, red line) compared to the actual potential (black line). (d) The eikonal-derived potential (pink line) obtained by stretching the squeezed eikonal potential in (b, pink line) compared to the actual potential (black line).

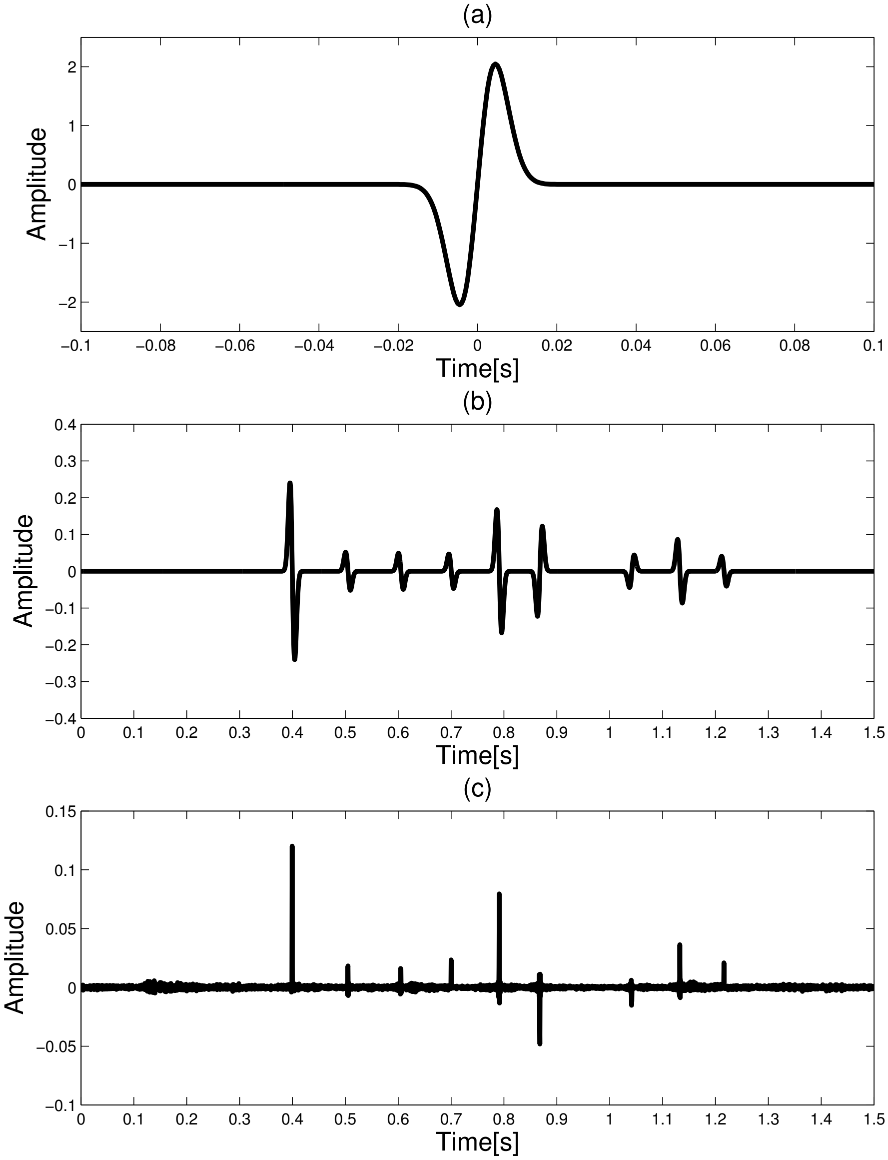

Figure 4.9: (a) The source wavelet used in the forward modeling of the scattered data. (b) The modeled single scattering data. (c) The modeled single scattering data where the source wavelet has been removed by spectral division.

Appendix 4.A
Modeling of the primary reflection response

We consider plane-wave propagation through a medium with $N+1$ homogeneous layers with constant layer velocities c_n and thicknesses h_n as shown in figure 4.1. The source and receiver are both located at depth $z=0$ in the zero'th layer which is the reference medium with velocity c_0.

The differential equation (4.2) together with proper boundary conditions yield that the pressure field is made up of an infinite sum of reflections and refractions inside the medium (Bremmer (1951)). In what follows we show how to model the exact primary reflection response, that is, the waves that are split off by reflection from the downgoing source wavefield when it is transmitted into the medium. To this end, it is necessary to define the reflection and transmission coefficients in the stack of layers. As is well known, the coefficients can be derived by assuming that the pressure and displacement are continuous fields at every boundary. For a plane wave incident in layer $n-1$, the reflection coefficient is

$$R_n = \frac{c_n - c_{n-1}}{c_n + c_{n-1}}\,, \qquad \text{(4-A-1)}$$

and the transmission coefficient is $T_n^{(D)} = 1 + R_n$. We will also need that a wave transmitted in the opposite direction, upwards from layer n into layer $n-1$, has transmission coefficient $T_n^{(U)} = 1 - R_n$. Thus, the two-way transmission loss for a plane wave passing down and up through the interface at depth z_n is $T_n^{(D)}T_n^{(U)} = 1 - R_n^2$.

When the source is initiated with unit strength a plane wave propagates downwards with velocity c_0 into the discontinuous, layered medium. At the boundary of the first layer, at depth $z_1 = h_0$, the incident wave which is represented by

$$D_0(\omega) = \exp(\mathrm{i}\omega h_0/c_0)\,,$$

is split into [I] a refracted wave penetrating into this layer with amplitude $T_1^{(D)}$ and represented by

$$D_1(\omega) = D_0(\omega)T_1^{(D)}\exp[\mathrm{i}\omega(z-z_1)/c_1] \;\;,\;\; z_1 < z < z_2\,,$$

and [II] a reflected wave with amplitude R_1 returning to the receiver level where it is represented by

$$\Phi_1(\omega) = R_1\exp(2\mathrm{i}\omega h_0/c_0)\,.$$

The downgoing wave $D_1(\omega)$ will be split at the next interface at depth z_2 into a refracted wave

$$D_2(\omega) = D_1(\omega) T_2^{(D)} \exp[\mathrm{i}\omega(z - z_2)/c_2] \quad , \quad z_2 < z < z_3 \, ,$$

penetrating into layer 2, and a reflected wave which, after being refracted through the interface at depth z_1 returns to the receiver level with representation

$$\Phi_2(\omega) = R_2(1 - R_1^2) \exp(2\mathrm{i}\omega h_1/c_1) \exp(2\mathrm{i}\omega h_0/c_0) \, .$$

This procedure of splitting is repeated at each next interface. The chain of wave consisting of the sequence $\Phi_1, \Phi_2, ..., \Phi_N$ is by Bremmer (1951) called the principal wave, but is in reflection seismology called the primary reflection response.

In the frequency domain the N events of the dimensionless scattering amplitude can be is modeled as

$$\Phi_{\mathrm{X}}(\omega) = \sum_{n=1}^{N} \Phi_n(\omega) = \sum_{n=1}^{N} \hat{R}_n \exp\left(2\mathrm{i}\omega \sum_{m=0}^{n-1} \frac{h_m}{c_m}\right) \, , \tag{4-A-2}$$

where each wave has the form of the product of an amplitude function and a delay function. The frequency dependency comes only as a complex exponential due to the delay. The amplitude of the wave from the interface at depth z_n is the product of the plane-wave reflection coefficient at z_n and the transmission coefficients encountered by the wave, namely

$$\hat{R}_1 = R_1 \quad , \quad \hat{R}_n = R_n \prod_{j=1}^{n-1} \left(1 - R_j^2\right) \quad , \quad n = 2, 3, ..., N \, . \tag{4-A-3}$$

Performing an inverse Fourier transform over frequency, the dimensionless scattering amplitude in the time domain becomes

$$\Phi_{\mathrm{X}}(t) = \sum_{n=1}^{N} \hat{R}_n \delta(t - t_n) \, , \tag{4-A-4}$$

where $\delta(t)$ is the Dirac delta-function. The arrival time of the primary reflection from depth z_n is $t_n = 2\sum_{m=0}^{n-1} \frac{h_m}{c_m}$.

Appendix 4.B
Two approximations introduced into the WKBJ approximation

In this appendix we develop two approximations that are introduced into equation (4.60).

4.6.1 First approximation

Writing

$$\xi(z) = \int_{-\infty}^{z} \mathrm{d}z' \, \xi'(z') \tag{4-B-1}$$

and

$$\tilde{\xi}(z) = \int_{-\infty}^{z} \mathrm{d}z' \, \tilde{\xi}'(z') \, , \tag{4-B-2}$$

and introducing

$$\tilde{\xi}'(z) = \frac{\xi'(z)}{1-\xi'(z)} \, , \tag{4-B-3}$$

partial integration gives

$$\tilde{\xi}(z) = \left. \frac{\xi(z')}{1-\xi'(z')} \right|_{0}^{z} - \int_{-\infty}^{z} \mathrm{d}z' \frac{\xi(z')\xi''(z')}{(1-\xi'(z'))^2} \, . \tag{4-B-4}$$

In the WKBJ approximation, $\xi''(z) = 0$; therefore,

$$\tilde{\xi}(z) = \frac{\xi(z)}{1-\xi'(z)} = \int_{-\infty}^{z} \mathrm{d}z' \, \frac{\xi'(z')}{1-\xi'(z')} \, . \tag{4-B-5}$$

4.6.2 Second approximation

By writing

$$\frac{1}{\sqrt{1-\alpha(z)}} = \frac{1}{\sqrt{1-\hat{\alpha}(z)}} \sqrt{1 + \frac{\alpha(z)-\hat{\alpha}(z)}{1-\alpha(z)}} \, , \tag{4-B-6}$$

we readily observe that a sufficient criterion for the the validity of the approximation (4.62) in the WKBJ approximation, is

$$\frac{\alpha(z)-\hat{\alpha}(z)}{1-\alpha(z)} \approx 0 \quad , \quad \frac{\mathrm{d}^n \xi(z)}{\mathrm{d}z^n} = 0 \quad , \quad n \geq 2\,. \tag{4-B-7}$$

By writing equation (4.49) in the form

$$\hat{\alpha}(z) = \alpha\left(z + \hat{\xi}(z)\right)\,, \tag{4-B-8}$$

where

$$\hat{\xi}(z) = \int_{-\infty}^{z} \mathrm{d}z' \,\left[(1-\hat{\alpha}(z'))^{-\frac{1}{2}} - 1\right]\,, \tag{4-B-9}$$

it can be shown that

$$\frac{\alpha(z)-\hat{\alpha}(z)}{1-\alpha(z)} = \\ -\frac{1}{1-\alpha(z)}\left[\alpha'(z)\hat{\xi}(z) + \frac{1}{2}\alpha''(z)\hat{\xi}^2(z) + \frac{1}{6}\alpha^{(3)}(z)\hat{\xi}^3(z) + ...\right]\,. \tag{4-B-10}$$

Further, from equation (4.34) it follows that in the WKBJ approximation where the second-order and all higher order derivatives of the shift function $\xi(z)$ can be disregarded, then $\alpha^{(n)}$ for $n \geq 1$ can be neglected. Therefore, in the WKBJ approximation it is allowed to write

$$\frac{1}{\sqrt{1-\alpha(z)}} \approx \frac{1}{\sqrt{1-\hat{\alpha}(z)}} \quad , \quad \frac{\mathrm{d}^n \xi(z)}{\mathrm{d}z^n} = 0 \quad , \quad n \geq 2\,. \tag{4-B-11}$$

Appendix 4.C[2]

Analysis of the relationship between the squeezed potential estimate $\hat{\hat{\alpha}}$ and the Born potential α_{B}

The WKBJ-derived equation (4.68) gives a relationship between the estimated squeezed potential $\hat{\hat{\alpha}}$ and the Born potential α_{B}. In this appendix we

---

[2] This appendix is not included in the Inverse Problems paper.

show that $\hat{\hat{\alpha}}$, derived from α_{B}, is a precise estimate of α for those acoustic media where the product of any three reflection coefficients is small compared to the reflection coefficients themselves. Further, the relationship between $\hat{\hat{\alpha}}$ and α_{B} can be used to estimate the acoustic velocity in the layered medium. The corresponding eikonal-derived equation (4.72) is not analyzed in this paper but can be shown to have similar properties.

The relationship is analyzed for a layered model by evaluating the accuracy between the n-layer potentials α_n and $\hat{\hat{\alpha}}_n$. The n-layer Born potential $\alpha_{n\mathrm{B}}$ derived in equation (4.47) is expressed as function of the reflection coefficients R_1 to R_n. Therefore, $\hat{\hat{\alpha}}_n$ can be represented in terms of the same reflection coefficients. The n-layer actual potential α_n defined in equation (4.44), on the other hand, is given in terms of the velocity ratio c_0/c_n. For the purpose of comparison with $\hat{\hat{\alpha}}_n$ it needs to be expressed in terms of the reflection coefficients. Equation (4-A-1) yields

$$\frac{c_{n-1}}{c_n} = \frac{1-R_n}{1+R_n}\,,$$

therefore the velocity ratio c_0/c_n can be written as

$$\frac{c_0}{c_n} = \frac{c_0}{c_1}\frac{c_1}{c_2}\ldots\frac{c_{n-1}}{c_n} = \prod_{j=1}^{n}\frac{1-R_j}{1+R_j}\,.$$

Hence, the n-layer actual potential α_n can be represented as

$$\alpha_n = 1 - \left(\prod_{j=1}^{n}\frac{1-R_j}{1+R_j}\right)^2 . \tag{4-C-1}$$

Series expanding and subtracting α_n and $\hat{\hat{\alpha}}_n$ show that

$$|\alpha_n - \hat{\hat{\alpha}}_n| = \mathrm{O}_n[R^3]\,, \tag{4-C-2}$$

where $\mathrm{O}_n[R^3]$ represents the product of any combination of reflection coefficients $R_1, R_2, \ldots, R_n$ to the power of three. Therefore, the difference between the n-layer actual potential and its estimate from the Born potential is always proportional to the third power of any of the reflection coefficients of the n-layered medium. Thus, when reflection coefficients of the medium are "small" in the sense that the product of any three of the reflection coefficients is vanishingly small compared to any of the reflection coefficients, it is a good approximation to estimate the squeezed potential from the Born potential by the algorithm

$$\hat{\hat{\alpha}}(z) = A_{\mathrm{W}}(z)\alpha_{\mathrm{B}}(z)\,, \tag{4-C-3}$$

where the WKBJ correction amplitude A_{W} is given in equation (4.69).

For example, consider $n = 1$, in which case α_1 and $\hat{\hat{\alpha}}_1$ can be written in terms of reflection coefficients as

$$\alpha_1/4 = \frac{R_1}{1 + 2R_1 + R_1^2} = R_1 - 2R_1^2 + 3R_1^3 - 4R_1^4 + \mathrm{O}[R_1^5]\,,$$

and

$$\hat{\hat{\alpha}}_1/4 = R_1\left[\left(1 + 4R_1^2\right)^{\frac{1}{2}} - 2R_1\right] = R_1 - 2R_1^2 + 2R_1^3 + \mathrm{O}_1[R_1^5]\,,$$

respectively. Subtraction of α_1 and $\hat{\hat{\alpha}}_1$ shows that

$$|\alpha_1 - \hat{\hat{\alpha}}_1|/4 = R_1^3 - 4R_1^4 + \mathrm{O}_1[R_1^5]\,. \tag{4-C-4}$$

Equation (4-C-4) implies that $\hat{\hat{\alpha}}_1$ is a good approximation to α_1 when R_1^3 is much smaller than R_1. Next, consider $n = 2$, in which case α_2 and $\hat{\hat{\alpha}}_2$ can be written in terms of reflection coefficients as

$$\alpha_2/4 = R_1 + R_2 - 4R_1R_2 - 2R_1^2 - 2R_2^2 + \mathrm{O}_2[R^3]\,,$$

and

$$\hat{\hat{\alpha}}_2/4 = R_1 + R_2 - 4R_1R_2 - 2R_1^2 - 2R_2^2 + \mathrm{O}_2[R^3]\,,$$

respectively. Subtraction of α_2 and $\hat{\hat{\alpha}}_2$ shows that

$$\begin{gathered}|\alpha_2 - \hat{\hat{\alpha}}_2|/4 = \\ 2R_1R_2^2 + 3R_1^2R_2 + R_1^3 + R_2^3 + 5R_1R_2^3 + 4R_1^3R_2 + 7R_1^2R_2^2 + \mathrm{O}_2[R^5]\,.\end{gathered} \tag{4-C-5}$$

Equation (4-C-5) implies that $\hat{\hat{\alpha}}_2$ is a good approximation to α_2 when the product of reflection coefficients R_1 and R_2 of the third power are negligible compared to the reflection coefficients R_1 and R_2. Likewise, the case $n = 3$ yields

$$\alpha_3/4 = R_1 + R_2 + R_3 - 4R_1R_2 - 4R_1R_3 - 4R_2R_3 - 2R_1^2 - 2R_2^2 - 2R_3^2 + \mathrm{O}_3[R^3]\,,$$

and

$$\hat{\hat{\alpha}}_3/4 = R_1 + R_2 + R_3 - 4R_1R_2 - 4R_1R_3 - 4R_2R_3 - 2R_1^2 - 2R_2^2 - 2R_3^2 + \mathrm{O}_3[R^3]\,.$$

Subtraction of the series expansions of α_3 and $\hat{\hat{\alpha}}_3$ gives

$$\begin{aligned} |\alpha_3 - \hat{\hat{\alpha}}_3|/4 \;&=\; R_1^3 + R_2^3 + R_3^3 + 2R_1R_2^2 + 2R_1R_3^2 + 2R_2R_3^2 + 3R_1^2R_2 + 3R_1^2R_3 \\ &\quad +3R_2^2R_3 + 4R_1R_2R_3 + \mathrm{O}_3[R^4]\,. \end{aligned} \tag{4-C-6}$$

Equation (4-C-6) shows that $\hat{\hat{\alpha}}_3$ is a good approximation to α_3 when the product of any of the reflection coefficients R_1, R_2 and R_3 to the third power is small compared to the reflection coefficients themselves. For a general n, equation (4-C-2) can be shown to be valid.

4.6.3 Layer velocities from the estimated potential

From the computation of $\hat{\hat{\alpha}}_n$ the velocity of layer n can be estimated. Equation (4.44) leads to the algorithm

$$\hat{c}_n = \frac{c_0}{\sqrt{1 - \hat{\hat{\alpha}}_n}}\,. \tag{4-C-7}$$

In the case that a continuous depth Born profile $\alpha_{\mathrm{B}}(z)$ is derived, the continuous velocity estimate reads

$$\hat{c}(z) = \frac{c_0}{\sqrt{1 - \hat{\hat{\alpha}}(z)}}\,. \tag{4-C-8}$$

The only information that is required to estimate the layer velocities is the Born potential obtained from constant-velocity imaging.

4.6.4 Analytic example

Consider the ten-layer medium where layer velocities c_n, actual potentials α_n and reflection coefficients R_n for $n = 1, ..., 9$ are listed in table 4.1. Assume that the Born potentials $\alpha_{n\mathrm{B}}$ corresponding to each of the layers have been found through constant-velocity imaging. Then, compute $\hat{\hat{\alpha}}_n$ from the Born potentials $\alpha_{n\mathrm{B}}$ by use of equation (4-C-3). Inputting $\hat{\hat{\alpha}}_n$ into equation (4-C-7) yields the estimated layer velocities, $\hat{c}_{n\mathrm{W}}$. The results presented in table 4.1

show that the layer velocity estimates are quite precise, the errors being less than three percent. Further, it is observed that the size of the error correlates with the amplitude size of the Born potential, α_{B}. When the same exercise is repeated in the eikonal approximation, one obtains the velocity estimates $\hat{c}_{n\mathrm{E}}$ presented in the table.

Appendix 4.D [3]
Simplification of equation (4.43)

In this appendix, we simplify equation (4.43), that is,

$$\alpha_B(z) = \sum_{n=0}^{\infty} \frac{1}{n!} \frac{d^n}{\mathrm{d}z^n} \alpha(z) \xi^n(z) \tag{4-D-1}$$

under the WKBJ approximation. First, we must evaluate the nth order derivatives. For order one to five we obtain:

$$(\alpha\xi)' = \alpha\xi' + \alpha'\xi \tag{4-D-2}$$

$$(\alpha\xi^2)'' = 2\alpha(\xi')^2 + 4\xi\alpha'\xi' + \xi^2\alpha'' + 2\alpha\xi\xi'' \tag{4-D-3}$$

$$\begin{aligned} (\alpha\xi^3)^{(3)} &= 6\alpha(\xi')^3 + 18\xi\alpha'(\xi')^2 + 9\xi^2\xi'\alpha'' + \xi^3\alpha^{(3)} + 9\xi^2\alpha'\xi'' \\ &\quad +18\alpha\xi\xi'\xi'' + 3\alpha\xi^2\xi^{(3)} \end{aligned} \tag{4-D-4}$$

$$\begin{aligned} (\alpha\xi^4)^{(4)} &= 24\alpha(\xi')^4 + 96\xi\alpha'(\xi')^3 + 72\xi^2(\xi')^2\alpha'' + 16\xi^3\xi'\alpha^{(3)} + \xi^4\alpha^{(4)} \\ &\quad +144\xi^2\alpha'\xi'\xi'' + 144\alpha\xi(\xi')^2\xi'' + 24\xi^3\alpha''\xi'' + 36\alpha\xi^2(\xi'')^2 \\ &\quad +16\xi^3\alpha'\xi^{(3)} + 48\alpha\xi^2\xi'\xi^{(3)} + 4\alpha\xi^3\xi^{(4)} \end{aligned} \tag{4-D-5}$$

$$\begin{aligned} (\alpha\xi^5)^{(5)} &= 120\alpha(\xi')^5 + 600\xi\alpha'(\xi')^4 + 600\xi^2(\xi')^3\alpha'' + 200\xi^3(\xi')^2\alpha^{(3)} \\ &\quad +25\xi^4\xi'\alpha^{(4)} + \xi^5\alpha^{(5)} + 1800\xi^2\alpha'(\xi')^2\xi'' + 1200\alpha\xi(\xi')^3\xi'' \\ &\quad +600\xi^3\xi'\alpha''\xi'' + 300\xi^3\alpha'(\xi'')^2 + 900\alpha\xi^2\xi'(\xi'')^2 + 50\xi^4\xi''\alpha^{(3)} \\ &\quad +400\xi^3\alpha'\xi'\xi^{(3)} + 600\alpha\xi^2(\xi')^2\xi^{(3)} + 50\xi^4\alpha''\xi^{(3)} \\ &\quad +200\alpha\xi^3\xi''\xi^{(3)} + 25\xi^4\alpha'\xi^{(4)} + 100\alpha\xi^3\xi'\xi^{(4)} + 5\alpha\xi^4\xi^{(5)} \end{aligned} \tag{4-D-6}$$

---

[3] This appendix is not included in the Inverse Problems paper.

Neglecting terms of order ξ'' and higher gives

$$(\alpha\xi)' = \alpha\xi' + \alpha'\xi \tag{4-D-7}$$

$$(\alpha\xi^2)'' = 2\alpha(\xi')^2 + 4\alpha'\xi\xi' + \alpha''\xi^2 \tag{4-D-8}$$

$$(\alpha\xi^3)^{(3)} = 6\alpha(\xi')^3 + 18\alpha'\xi(\xi')^2 + 9\alpha''\xi^2\xi' + \alpha^{(3)}\xi^3 \tag{4-D-9}$$

$$\begin{aligned}(\alpha\xi^4)^{(4)} &= 24\alpha(\xi')^4 + 96\alpha'\xi(\xi')^3 + 72\alpha''\xi^2(\xi')^2 \\ &\quad +16\alpha^{(3)}\xi^3\xi' + \alpha^{(4)}\xi^4\end{aligned} \tag{4-D-10}$$

$$\begin{aligned}(\alpha\xi^5)^{(5)} &= 120\alpha(\xi')^5 + 600\alpha'\xi(\xi')^4 + 600\alpha''\xi^2(\xi')^3 + 200\alpha^{(3)}\xi^3(\xi')^2 \\ &\quad +25\alpha^{(4)}\xi^4\xi' + \alpha^{(5)}\xi^5\end{aligned} \tag{4-D-11}$$

With this approximation, in Table 4.3 we list the terms entering equation (4-D-1) for $n = 0, ..., 5$. Considering the table, observe that summing along diagonals, gives the following series representation for α_B:

$$\alpha_B = \sum_{n=0}^{\infty} \alpha_n = \sum_{n=0}^{\infty} (\xi')^n \hat{\alpha}_n \tag{4-D-12}$$

where

$$\hat{\alpha}_0 = \alpha + \alpha'\xi + \frac{1}{2!}\alpha''\xi^2 + \frac{1}{3!}\alpha^{(3)}\xi^3 + \frac{1}{4!}\alpha^{(4)}\xi^4 + \frac{1}{5!}\alpha^{(5)}\xi^5 + ... \tag{4-D-13}$$

$$\hat{\alpha}_1 = \alpha\xi' + \frac{4}{2!}\alpha'\xi + \frac{9}{3!}\alpha''\xi^2\xi' + \frac{16}{4!}\alpha^{(3)}\xi^3\xi' + \frac{25}{5!}\alpha^{(4)}\xi^4\xi' + ... \tag{4-D-14}$$

$$\hat{\alpha}_2 = \frac{2}{2!}\alpha + \frac{18}{3!}\alpha'\xi + \frac{72}{4!}\alpha''\xi^2 + \frac{200}{5!}\alpha^{(3)}\xi^3 + ... \tag{4-D-15}$$

$$\hat{\alpha}_3 = \frac{6}{3!}\alpha + \frac{96}{4!}\alpha'\xi + \frac{600}{5!}\alpha''\xi^2 + ... \tag{4-D-16}$$

$$\hat{\alpha}_4 = \frac{24}{4!}\alpha + \frac{600}{5!}\alpha'\xi + ... \tag{4-D-17}$$

n						
0	$\frac{1}{0!}\alpha$					
1	$\frac{1}{1!}\alpha\xi'$	$\frac{1}{1!}\alpha'\xi$				
2	$\frac{2}{2!}\alpha(\xi')^2$	$\frac{4}{2!}\alpha'\xi\xi'$	$\frac{1}{2!}\alpha''\xi^2$			
3	$\frac{6}{3!}\alpha(\xi')^3$	$\frac{18}{3!}\alpha'\xi(\xi')^2$	$\frac{9}{3!}\alpha''\xi^2\xi'$	$\frac{1}{3!}\alpha^{(3)}\xi^3$		
4	$\frac{24}{4!}\alpha(\xi')^4$	$\frac{96}{4!}\alpha'\xi(\xi')^3$	$\frac{72}{4!}\alpha''\xi^2(\xi')^2$	$\frac{16}{4!}\alpha^{(3)}\xi^3\xi'$	$\frac{1}{4!}\alpha^{(4)}\xi^4$	
5	$\frac{120}{5!}\alpha(\xi')^5$	$\frac{600}{5!}\alpha'\xi(\xi')^4$	$\frac{600}{5!}\alpha''\xi^2(\xi')^3$	$\frac{200}{5!}\alpha^{(3)}\xi^3(\xi')^2$	$\frac{25}{5!}\alpha^{(4)}\xi^4\xi'$	$\frac{1}{5!}\alpha^{(5)}\xi^5$

Table 4.3: Terms in equation (4-D-1).

$$\hat{\alpha}_5 = \frac{120}{5!}\alpha + ... \tag{4-D-18}$$

It follows that $\hat{\alpha}_n$ and α become

$$\begin{aligned}\hat{\alpha}_n = \sum_{m=n}^{\infty} \frac{n!}{m!} \left(\begin{array}{c} m \\ n \end{array} \right)^2 \xi^{m-n} \alpha^{(m-n)} = \\ \sum_{m=n}^{\infty} \frac{1}{(m-n)!} \left(\begin{array}{c} m \\ n \end{array} \right) \xi^{m-n} \alpha^{(m-n)}\end{aligned} \tag{4-D-19}$$

and

$$\alpha_n = (\xi')^n \sum_{m=n}^{\infty} \frac{1}{(m-n)!} \left(\begin{array}{c} m \\ n \end{array} \right) \xi^{m-n} \alpha^{(m-n)} \tag{4-D-20}$$

Observe that α_n is proportional to $(\xi')^n$.

Appendix 4.E [4]

Closed-form expression for equation (4.53)

---

[4] This appendix is not included in the Inverse Problems paper.

Our goal is to derive a closed-form expression for equation (4.53). First consider

$$\alpha_n(z) = \left(\frac{\mathrm{d}\xi(z)}{\mathrm{d}z}\right)^n \sum_{m=n}^{\infty} \frac{1}{(m-n)!} \left(\begin{array}{c} m \\ n \end{array} \right) \xi^{m-n}(z) \frac{d^{m-n}\alpha(z)}{\mathrm{d}z^{m-n}}. \tag{4-E-1}$$

To this end, the Fourier representation of $\alpha_n(z)$ is introduced, which gives

$$\begin{aligned} \alpha_n(z) &= \\ &\left(\frac{\mathrm{d}\xi(z)}{\mathrm{d}z}\right)^n \sum_{m=n}^{\infty} \frac{1}{(m-n)!} \left(\begin{array}{c} m \\ n \end{array} \right) \xi^{m-n}(z) \frac{1}{2\pi} \int_{-\infty}^{\infty} \mathrm{d}k \exp(-ikz)(-ik)^{m-n}\alpha(k) \\ &= \left(\frac{\mathrm{d}\xi(z)}{\mathrm{d}z}\right)^n \frac{1}{2\pi} \int_{-\infty}^{\infty} \mathrm{d}k D_n(k\xi) \exp(-ikz)\alpha(k), \qquad (4\text{-E-}2) \end{aligned}$$

where

$$D_n(k\xi) = \sum_{m=n}^{\infty} \frac{1}{(m-n)!} \left(\begin{array}{c} m \\ n \end{array} \right) [-ik\xi(z)]^{m-n}. \tag{4-E-3}$$

Setting $x = ik\xi$, D_n for $n = 0, ..., 5$ becomes

$$\begin{aligned} D_0 &= \exp(-x) && (4\text{-E-}4) \\ D_1 &= (1-x)\exp(-x) && (4\text{-E-}5) \\ D_2 &= \frac{1}{2}(2-4x+x^2)\exp(-x) && (4\text{-E-}6) \\ D_3 &= \frac{1}{6}(6-18x+9x^2-x^3)\exp(-x) && (4\text{-E-}7) \\ D_4 &= \frac{1}{24}(24-96x+72x^2-16x^3+x^4)\exp(-x) && (4\text{-E-}8) \\ D_5 &= \frac{1}{120}(120-600x+600x^2-200x^3+25x^4-x^5)\exp(-x) && (4\text{-E-}9) \end{aligned}$$

D_n can be written

$$D_n = \exp(-x) \sum_{m=0}^{n} \frac{1}{m!} \left(\begin{array}{c} n \\ m \end{array} \right) (-x)^{n-m}. \tag{4-E-10}$$

The evaluation of the Born potential in equation (4.53), that is,

$$\alpha_B = \sum_{n=0}^{\infty} \alpha_n \tag{4-E-11}$$

now amounts to evaluating

$$\alpha_B = \frac{1}{2\pi}\int_{-\infty}^{\infty}\mathrm{d}k\left\{\sum_{n=0}^{\infty}\left(\frac{\mathrm{d}\xi}{\mathrm{d}z}\right)^n\sum_{m=0}^{n}\frac{1}{m!}\binom{n}{m}(-ik\xi)^{n-m}\right\}\exp[-ik(z+\xi)]\alpha(k). \quad (4\text{-E-12})$$

As before, let $x = ik\xi$. Introducing $y = \mathrm{d}\xi/\mathrm{d}z$, we must evaluate the double sum

$$S = \sum_{n=0}^{\infty} y^n \sum_{m=0}^{n}\frac{1}{m!}\left(\begin{array}{c} n \\ m \end{array}\right)(-x)^{n-m}. \quad (4\text{-E-13})$$

Considering equations (4-E-4) to (4-E-9), we obtain by grouping terms in powers of x (that is, summing in the vertical direction)

$$S = \sum_{n=0}^{\infty} S_n, \quad (4\text{-E-14})$$

where

$$\begin{aligned}
S_0 &= 1 + y + y^2 + y^3 + y^4 + y^5 + ... = \frac{1}{1-y} && (4\text{-E-15})\\
S_1 &= -xy\left(1 + 2y + 3y^2 + 4y^3 + 5y^4 + ...\right) = -\frac{xy}{(1-y)^2} && (4\text{-E-16})\\
S_2 &= \frac{1}{2!}(xy)^2\left(1 + 3y + 6y^2 + 10y^3 + ...\right) = \frac{1}{2!}\frac{(xy)^2}{(1-y)^3} && (4\text{-E-17})\\
S_3 &= -\frac{1}{3!}(xy)^3\left(1 + 4y + 10y^2 + ...\right) = -\frac{1}{3!}\frac{(xy)^3}{(1-y)^4} && (4\text{-E-18})
\end{aligned}$$

and

$$S_n = (-1)^n\frac{1}{n!}\frac{(xy)^n}{(1-y)^{n+1}}. \quad (4\text{-E-19})$$

Therefore, the sum (4-E-14) becomes

$$S = \frac{1}{(1-y)}\sum_{n=0}^{\infty}(-1)^n\frac{1}{n!}\left(\frac{xy}{1-y}\right)^n = \frac{1}{(1-y)}\exp\left(-\frac{xy}{1-y}\right). \quad (4\text{-E-20})$$

The Born potential in equation (4-E-12) becomes

$$\alpha_B = \frac{1}{1-\frac{\mathrm{d}\xi}{\mathrm{d}z}} \frac{1}{2\pi} \int_{-\infty}^{\infty} \mathrm{d}k \exp\left[-ik \left(z + \xi + \xi \frac{\mathrm{d}\xi}{\mathrm{d}z} / \left(1 - \frac{\mathrm{d}\xi}{\mathrm{d}z} \right) \right) \right] \alpha(k). \tag{4-E-21}$$

Simplifying the expression in the exponential function,

$$\xi + \xi \frac{\mathrm{d}\xi}{\mathrm{d}z} / \left(1 - \frac{\mathrm{d}\xi}{\mathrm{d}z} \right) = \frac{\xi}{1 - \frac{\mathrm{d}\xi}{\mathrm{d}z}}, \tag{4-E-22}$$

and using the translation property of the Fourier transform, we obtain a closed-form expression for the Born potential,

$$\alpha_B = \frac{1}{1-\frac{\mathrm{d}\xi}{\mathrm{d}z}} \quad \alpha \left(z + \frac{\xi}{1 - \frac{\mathrm{d}\xi}{\mathrm{d}z}} \right). \tag{4-E-23}$$

Appendix 4.F [5]

Inverse Fourier transform of equation (4.40)

This appendix demonstrates that the inverse Fourier transform over frequency of equation (4.40) yields equation (4.41). To this end, we make use of the Dirac delta function properties.

$$\int_{-\infty}^{\infty} \mathrm{d}x f(x) \frac{\mathrm{d}^n \delta(x-a)}{\mathrm{d}x^n} = (-1)^n \frac{\mathrm{d}^n f(a)}{\mathrm{d}x^n}, \tag{4-F-1}$$

$$\delta(ax) = \frac{1}{|a|} \delta(x), \tag{4-F-2}$$

and the Fourier transform representation

$$\frac{\mathrm{d}^n \delta(x-a)}{\mathrm{d}x^n} = \frac{1}{2\pi} \int_{-\infty}^{\infty} \mathrm{d}k (\mathrm{i}k)^n \exp[\mathrm{i}k(x-a)]. \tag{4-F-3}$$

---

[5] This appendix is not included in the Inverse Problems paper.

In addition we make use of the Fourier integral transform

$$\frac{1}{2\pi}\int_{-\infty}^{\infty} \mathrm{d}k\ \exp[-\mathrm{i}kz]\frac{f(k)}{-\mathrm{i}k} = \int_{-\infty}^{z} \mathrm{d}t\ f(t). \tag{4-F-4}$$

For any finite k and $\xi(z)$, express the exponential function $\exp[\mathrm{i}k\xi(z)]$ in equation (4.40) as an infinite series

$$\exp[-2\mathrm{i}k\xi(z)] = \sum_{n=0}^{\infty} \frac{(-2\mathrm{i}k)^n}{n!}\ \xi^n(z). \tag{4-F-5}$$

Equation (4.40) is then written as

$$\frac{\Phi(\omega)}{-\mathrm{i}\omega} = \frac{q}{2}\sum_{n=0}^{\infty}\frac{(-q)^n}{n!}\int_0^{\infty} \mathrm{d}z'\ \alpha(z')(2\mathrm{i}\omega)^n \exp[2\mathrm{i}\omega q z'], \tag{4-F-6}$$

where we have used that $k = \omega q$. Applying the inverse Fourier transform $(2\pi)^{-1}\int \mathrm{d}\omega\ \exp[-\mathrm{i}\omega(2qz]$ to equation (4-F-6), and using equation (4-F-4), and interchanging the depth and frequency integrals give

$$4\int_{-\infty}^{2qz}\mathrm{d}t'\,\Phi(t') = q\sum_{n=0}^{\infty}\frac{(-q)^n}{n!}\int_0^{\infty}\mathrm{d}z'\,\alpha(z')\frac{1}{2\pi}\int_{-\infty}^{\infty}\mathrm{d}\omega\,(\mathrm{i}\omega)^n\exp[\mathrm{i}\omega q(z'-z)]. \tag{4-F-7}$$

By using the Delta function properties (4-F-3), (4-F-2) and (4-F-1), and recalling that $q = 1/c_0$, one obtains equation (4.41).

References

Aki K and Richards P G 1980 *Quantitative seismology* (W H Freeman and Co)

Amundsen L 1994 The propagator matrix related to the Kirchhoff-Helmholtz integral in inverse wavefield extrapolation *Geophysics* **59** 1902-1910

Amundsen L, Reitan A and Arntsen B 2005 Geometric analysis of data-driven inversion/depth imaging *Journal Seismic Exploration* **14** 51-62

Bender C M and Orszag S A 1978, *Advanced mathematical methods for scientists and engineers* (McGraw-Hill)

Berkhout A J 1982, *Seismic Migration, Imaging of Acoustic Wave Energy by Wavefield Extrapolation, A: Theoretical Aspects* 2nd edn (Amsterdam: Elsevier)

Berryman J G and Greene R R 1980 Discrete inverse methods for elastic waves in layered media *Geophysics* **45** 213-233

Bleistein N 1984 *Mathematical methods for wave phenomena* (Academic Press)

Bransden B H and Joachain C 1989 *Introduction to quantum mechanics* (Longman Scientific & Technical)

Bremmer H 1951 The W.K.B. approximation as a first term of a geometric-optical series *The theory of electromagnetic waves, A symposium* (New York: Interscience Publ.) p 169-179

Bruckstein A M, Levy B C and Kailath T 1985 Differential methods in inverse scattering *SIAM J. Appl. Math.* **45** 312-335

Bube P K and Burridge B 1983 The one-dimensional inverse problem of reflection seismology *SIAM Review* **25** 497-559

Burridge R 1980 The Gel'fand-Levitan, the Marchenko, and the Gopinath-Sondhi integral equations in inverse scattering theory, regarded in the context of inverse impulse response problems *Wave motion* **2** 305-323

Carroll R and Santosa F 1981 Scattering techniques for a one-dimensional inverse problem in geophysics *Math. Meth. in the Appl. Sci.* **3** 145-171

Claerbout J F 1968 Synthesis of a layered medium from its acoustic transmission response *Geophysics* **33** 264-269

Claerbout J F 1971 Towards a unified theory of reflector mapping *Geophysics* **36** 467-481

Clayton R W and Stolt R H 1981 A Born-WKBJ inversion method for acoustic reflection data *Geophysics* **46** 1559-1567

Coen S 1981 On the elastic profiles of a layered medium from reflection data. I. Plane wave sources *J. Acoust. Soc. Am.* **70**

Fröman N and Fröman P O 1965 *JWKB approximation. Contributions to the theory* (North Holland Publ. Co)

Gjevik B, Nilsen A, and Høyen J 1976 An attempt at the inversion of reflection data *Geophysical Prospecting* **24** 492-505

Gladwell G M L 1993 *Inverse problems in scattering: an introduction* (Kluwer Academic Publishers)

Glauber R J 1959 High-energy collision theory *Lectures in theoretical physics, Boulder 1958* ed W E Brittin and L G Dunham (New York: Interscience Publishers Inc) p 315-414

Goupillaud P 1961 An approach to inverse filtering of near-surface layer effects from seismic records *Geophysics* **26** 754-760

Ikelle L T and Amundsen L 2005 *Introduction to petroleum seismology* (Society of Exploration Geophysics)

Innanen K A 2003 *Methods for the treatment of acoustic and absorptive/dispersive wave field measurements* (Ph.D. thesis, University of British Columbia)

Innanen K A and Weglein A B 2003 Simultaneous imaging and inversion with the inverse scattering series *Proc. 8th Internat. Cong. of the SBGf and 5th Latin American Geophys. Conf.*

Koehler F and Taner M T 1977 Direct and inverse problems relating reflection coefficients and reflection response for horizontally layered media *Geophysics* **42** 1199-1206

Liu F, Weglein A B, Innanen K A, and Nita B G, 2005, Extension of the non-linear depth imaging capability of the inverse scattering series to multidimensional media: strategies and numerical results *Proc. 9th Internat. Cong. of the SBGf and 6th Latin American Geophys. Conf.*

Morse P M and Feshbach H 1953 *Methods of theoretical physics* (McGraw-Hill Book Co)

Morse P M and Ingard K U 1968 *Theoretical acoustics* (New York: McGraw-Hill)

Newton R 1981 Inversion of reflection data for layered media: a review of exact methods *Geophys. J. Roy. Astr. Soc.* **65** 191-215

Nilsen A and Gjevik B 1978 Inversion of reflection data *Geophysical Prospecting* **26** 421-432

Ramirez A C and Weglein A B 2005 Progressing the analysis of the phase and amplitude prediction properties of the inverse scattering internal multiple attenuation algorithm *J. Seis. Expl.* **13** 283-301

Razavy M 1975 Determination of the wave velocity in an inhomogeneous medium from the reflection coefficient *J. Acoust. Soc. Am.* **58** 956-963

Reitan A 1979 Relativistic Glauber amplitudes for elastic electron and positron scattering by hydrogen atoms and hydrogenlike ions in the ground state *Phys. Rev.* A **20** 1385-1392

Robinson E A 1982 Migration of seismic data as W.K.B. approximation *Geoexploration* **20** 7-30

Robinson E A 1986 Migration of seismic data by the WKBJ method *Proc. IEEE* **74** 428-439

Santosa F 1982 Numerical scheme for the inversion of acoustical impedance profile based on the Gelfand-Levitan method *Geophys. J. Roy. Astr. Soc.* **70**

Santosa F and Schwetlick H 1982 The inversion of acoustical impedance profiles by the method of characteristics *Wave motion* **4** 99-110

Schiff L I 1955 *Quantum mechanics* (London: McGraw-Hill Publishing Company Ltd)

Shaw S A 2005 *An inverse scattering series algorithm for depth imaging of reflection data from a layered acoustic medium with an unknown velocity model* (Ph.D. thesis, University of Houston)

Shaw S A, Weglein A B, Foster D J, Matson K H and Keys R G 2004 Isolation of a leading order depth imaging series and analysis of its convergence properties for a 1D acoustic medium *J. Seis. Expl.* **13** 99-120

Stolt R H and Benson A K 1986 *Seismic migration: Theroy and Practice* (London: Geophysical Press)

Stolt R H and Weglein A B 1985 Migration and inversion of seismic data *Geophysics* **50** 2458-2472

Symes W 1981 Stable solution of the inverse reflection problem for a smoothly stratified medium *SIAM J. Math. Anal.* **12**

Ursin B 1984 Seismic migration using the WKB approximation *Geophys. J. Roy. Astr. Soc.* **79** 339-352

Ursin B 1987 The plane-wave reflection and transmission response of a vertically inhomogeneous acoustic medium *Deconvolution and inversion* ed M Bernabini *et al* (Blackwell Scientific Publications) p 189-207

Ursin B and Berteussen K A 1986 Comparison of some inverse methods for wave propagation in layered media *Proceedings of the IEEE* **74** 389-400

Ware J A and Aki K 1968 Continuous and discrete inverse-scattering problems in a stratified elastic medium. I Plane waves at normal incidence *J. Acoust. Soc. Am.* **45** 911-921

Weglein A B 1985 The inverse scattering concept and its seismic application *Developments in Geophysical Exploration Methods* vol 6, ed A A Fitch (Amsterdam: Elsevier) pp 111-138

Weglein A B, Araújo R V, Carvalho P M, Stolt R H, Matson K H, Coates R T, Corrigan D, Foster D J, Shaw S A and Zhang H 2003 Inverse scattering series and seismic exploration *Inverse Problems* **19** R27-R83

Weglein A B, Foster D J, Matson K H, Shaw S A, Carvalho P M and Corrigan D 2002 Predicting the correct spatial location of reflectors without knowing or determining the precise medium and wave velocity: initial concept, and analytic and numerical example *J. Seis. Expl.* **10** 367-382

Weglein A B, Gasparotto F A, Carvalho P M and Stolt R H 1997 An inverse scattering series method for attenuating multiples in seismic data *Geophysics* **62** 1975-1989

Weglein A B, Matson K H, Foster D J, Carvalho P M , Corrigan D and Shaw S A 2000 Imaging and inversion at depth without a velocity model: theory, concepts, and initial evaluation *Expanded Abstracts, 70th Ann. Internat. Mtg., Soc. Expl. Geophys.*

Zhang H and Weglein A B 2005 The inverse scattering series for tasks associated with primaries: depth imaging and direct non-linear inversion of 1D variable velocity and density acoustic media *Expanded Abstracts, 75th Ann. Internat. Mtg., Soc. Expl. Geophys.*

Chapter 5

Forward and inverse models in one-dimensional acoustic scattering

Abstract

This paper presents a new model for single forward scattering of acoustic waves in a 1D stratified medium. The new model is compared to the model presented in Chapter 4. Analytic studies and numerical examples show that the new model performs more accurately both with regards to amplitude handling in the forward modeling and thus with regards to estimation of the layer depths and layer velocities in the inversion.

The method is evaluated through analytic studies and synthetic data examples.

5.1 Introduction

General inverse geophysical methods have been the subject of many research papers since the 1970s. In particular, inverse scattering methods from the mainstream physics were introduced to the petroleum exploration industry during the late 1970s and early 1980s (see, e.g., Razavy (1975) and Weglein (1985)). During the last few years, inverse scattering theories related to seismic have been revisited and further developed. Weglein *et al* (2000, 2002, 2003) introduced the general and exact inverse scattering series, where the three-dimensional (3D) potential is expanded in a series, each term of which is determined in terms of the scattering data and a reference Green's function. Further, Weglein and coworkers introduce the subseries approach for eliminating multiples and imaging/inverting primaries. Significant results related to the inverse scattering series and its subseries for inversion/imaging are reported in Innanen (2003), Innanen and Weglein (2003), Shaw *et al* (2004), Shaw (2005), Zhang and Weglein (2005) and Liu *et al* (2005). On the other hand, influenced by the results of Weglein and coworkers and those presented in Shaw *et al* (2004) in particular, Amundsen *et al* (2005a, 2005b) by limiting the inverse scattering problem to that of processing single scattering data, proposed to directly invert for the scattering potential for a one-dimensional (1D) forward scattering model in the WKBJ approximation.

In this paper we derive a new physical model for single scattering of acoustic waves in a 1D stratified medium based on the first-order WKBJ approximation. The model is inverted using the same strategy as presented in Chapter 4. The model is then compared with the model presented in Chapter 4 and by Amundsen *et al* (2005b) both with regards to the amplitude handling in the forward modeling and with regards to inversion results.

5.2 The forward scattering model

In this section we present the forward model of acoustic scattering in a 1D medium. For a 1D medium it is standard procedure to transform the physical field variables by applying a Fourier transform with respect to time. This transforms the acoustic equations into a system of first order differential equations.

Let t denote time and z the depth coordinate, where z is positive downwards. An acoustic medium, where wave velocity c is a function of z is embedded in a homogeneous reference medium with wave velocity c_0. Density $\rho = \rho_0$ is constant. The system of equations governing wave motion consists of the pressure-particle velocity relation (the time derivative of Hooke's law),

$$\frac{\partial v(z,t)}{\partial z} + \frac{1}{M(z)}\frac{\partial p(z,t)}{\partial t} = \frac{\partial i_v(z,t)}{\partial t}\,, \tag{5.1}$$

and the equation of motion

$$\frac{\partial p(z,t)}{\partial z} + \rho_0\frac{\partial v(z,t)}{\partial t} = 0\,, \tag{5.2}$$

where p is the pressure, v is the particle velocity, $M = \rho_0 c^2$ is the bulk modulus, and i_v is a source distribution which represents a volume density of volume injection. A monopole point source at $z = 0$ is represented by

$$\rho_0 \frac{\partial^2 i_v(z,t)}{\partial t^2} = \delta(z)s(t)\,,$$

where $s(t)$ is the source signature and $\delta(z)$ represents a Dirac delta function. The boundary conditions state continuity of pressure and particle velocity at the interfaces. In addition, we impose the radiation conditions that the only downgoing wave in the source layer is that radiated by the source, and that there are no upgoing waves in the lower halfspace.

We introduce the Fourier transform with respect to time

$$G(\omega) = \int_{-\infty}^{\infty} \mathrm{d}t \exp(\mathrm{i}\omega t) g(t)\,, \tag{5.3}$$

with inverse

$$g(t) = \frac{1}{2\pi} \int_{-\infty}^{\infty} \mathrm{d}\omega \exp(-\mathrm{i}\omega t) G(\omega)\,. \tag{5.4}$$

were ω denotes circular frequency. In the following we introduce the wavenumber $k(z) = \omega / c(z)$. In the reference medium the wavenumber is denoted by $k_0 = \omega / c_0$.

Fourier transform of equations (5.1) and (5.2) leads to the first-order wave equation for pressure P and particle velocity V (Ursin 1983),

$$\frac{\mathrm{d}}{\mathrm{d}z} \boldsymbol{B}(z) = \boldsymbol{A}(z)\boldsymbol{B}(z) + \boldsymbol{\Sigma}(z)\,, \tag{5.5}$$

with field vector

$$\boldsymbol{B}(z) = \begin{bmatrix} P(z) \\ V(z) \end{bmatrix}, \tag{5.6}$$

system matrix

$$\boldsymbol{A}(z) = \begin{bmatrix} 0 & \mathrm{i}\omega\rho_0 \\ -[\mathrm{i}\omega\rho_0]^{-1} k^2(z) & 0 \end{bmatrix}, \tag{5.7}$$

and source vector

$$\boldsymbol{\Sigma}(z) = \begin{bmatrix} 0 \\ -i\omega I_v(z) \end{bmatrix}. \tag{5.8}$$

To characterize the difference between the reference and actual media we introduce the velocity potential

$$\alpha_c(z) = 1 - \left(\frac{c_0}{c(z)}\right)^2 . \tag{5.9}$$

The wavenumber now can be expressed as

$$k(z) = k_0 \, \Gamma(z) \, ,$$

where

$$\Gamma(z) = [1 - \alpha_c(z)]^{\frac{1}{2}} = \frac{c_0}{c(z)} \tag{5.10}$$

is a function of the velocity potential and defines the ratio between the velocities in the reference and actual media. In the scattering formalism, the system matrix then can be written

$$\boldsymbol{A}(z) = \left[\begin{array}{ll} 0 & \mathrm{i}\omega\rho_0 \\ -[\mathrm{i}\omega\rho_0]^{-1} k_0^2 \Gamma^2(z) & \quad 0 \end{array} \right] . \tag{5.11}$$

The field vector $\boldsymbol{B}$ can be decomposed into a wave vector $\boldsymbol{W} = (U, D)^T$ containing upgoing (U) and downgoing (D) pressure waves by an eigensystem analysis of the system matrix $\boldsymbol{A}$. By inserting the eigenvectors of $\boldsymbol{A}$ into the columns of the matrix $\boldsymbol{L}$, the up/down decomposition is achieved by the linear transformation

$$\boldsymbol{W} = \boldsymbol{L}^{-1} \boldsymbol{B} \, , \tag{5.12}$$

where

$$\boldsymbol{L}^{-1} = \frac{1}{2} \left[\begin{array}{rr} 1 & -Z \\ 1 & Z \end{array} \right] \tag{5.13}$$

is the decomposition matrix, and

$$\boldsymbol{L} = \left[\begin{array}{rr} 1 & 1 \\ -Z^{-1} & Z^{-1} \end{array} \right] \tag{5.14}$$

is the composition matrix, with

$$Z(z) = Z_0 \, [\Gamma(z)]^{-1} \, ,$$

where $Z_0 = \rho_0 \omega / k_0$ is the acoustic impedance of the reference medium.

5.2.1 Differential equation for $\boldsymbol{W}$ in an inhomogeneous medium

Disregarding the source term in equation (5.5) the differential equation for $\boldsymbol{W}$ in an inhomogeneous medium follows from equation (5.5) as

$$\frac{\mathrm{d}\boldsymbol{W}(z)}{\mathrm{d}z} = \left[\boldsymbol{\Lambda}(z) - \boldsymbol{L}^{-1}(z)\frac{\mathrm{d}\boldsymbol{L}(z)}{\mathrm{d}z}\right]\boldsymbol{W}(z)\,, \tag{5.15}$$

where the eigenvalue decomposition of $\boldsymbol{A}$ gives the diagonal eigenvalue matrix

$$\boldsymbol{\Lambda} = \boldsymbol{L}^{-1}\boldsymbol{A}\boldsymbol{L}\,. \tag{5.16}$$

Equation (5.15) then can be written

$$\frac{d\boldsymbol{W}(z)}{dz} = \begin{bmatrix} -\mathrm{i}k_0\Gamma(z) & 0 \\ 0 & \mathrm{i}k_0\Gamma(z) \end{bmatrix}\boldsymbol{W}(z) + s(z)\begin{bmatrix} 1 & -1 \\ -1 & 1 \end{bmatrix}\boldsymbol{W}(z)\,, \tag{5.17}$$

where s is the scattering function,

$$s(z) = -\frac{1}{2}Z(z)\left(\frac{\mathrm{d}Z^{-1}(z)}{\mathrm{d}z}\right) = -\frac{1}{2}\frac{\mathrm{d}}{\mathrm{d}z}\ln\left[\Gamma(z)\right]\,. \tag{5.18}$$

The differential equations for U and D thus become

$$\frac{\mathrm{d}U(z)}{\mathrm{d}z} = -\mathrm{i}k_0\Gamma(z)U(z) + s(z)\left[U(z) - D(z)\right]\,, \tag{5.19}$$

and

$$\frac{\mathrm{d}D(z)}{\mathrm{d}z} = \mathrm{i}k_0\Gamma(z)D(z) + s(z)\left[D(z) - U(z)\right]\,. \tag{5.20}$$

Note that the upgoing and downgoing waves are coupled because of the vertical variations of the medium parameters, which are expressed by the term $\mathrm{d}\boldsymbol{L}/\mathrm{d}z$.

In the reference medium, $\alpha_c = 0$, and the exact solution for the upgoing and downgoing waves is

$$\begin{aligned} U(z) &= \exp(-ik_0z)U(0)\,, \\ D(z) &= \exp(ik_0z)D(0)\,. \end{aligned}$$

Neither of these two solutions admit scattering.

As is usual in scattering theory, the potential $\alpha_c(z)$ is assumed to vanish asymptotically, i.e., $\alpha_c(z) \to 0$ as $z \to \pm\infty$, at which limit the wave function P is merely a plane propagating wave described by $\exp(\pm\mathrm{i}k_0z)$.

5.2.2 WKBJ solutions for incident and scattered waves

Equations (5.19) and (5.20) are general differential equations for U and D, and they describe all possible wave arrivals in the layered medium. In particular, they show how the entire wave field is made up of all the internal reflections and transmissions within the medium. This wave field can be represented by an infinite series, known as the Bremmer series (Bremmer 1951), each term which of represents a wave that is reflected a particular number of times inside the medium.

In this paper, however, our interest is to describe single scattering. To this end, we must describe the downward propagation of the incident field, and its interaction with the upward propagating single-scattered wave. Then, for the incident field we neglect the coupling of U with D. (We do not include the generation of downgoing waves (multiples) caused by the upgoing scattered field.) Disregarding this interaction, which is called the zero-order WKBJ approximation, gives the one-way wave equation for the incident field,

$$\frac{\mathrm{d}D_0(z)}{\mathrm{d}z} = \left[\mathrm{i}k_0\Gamma(z) + s(z)\right] D_0(z)\,, \tag{5.21}$$

with solution

$$D_0(z) = D_0(0)\exp\left(\int_0^z \mathrm{d}z' s(z')\right)\exp\left(\mathrm{i}k_0\int_0^z \mathrm{d}z'\,\Gamma(z')\right)\,. \tag{5.22}$$

The boundary condition states that the only downgoing wave in the source layer is that radiated by the source. Considering a point-source represented by a Dirac delta function at $z = 0$, the downgoing field just below the source is:

$$D_0(0^+) = A(k_0) = -\frac{a(\omega)}{2\mathrm{i}k_0}\,, \tag{5.23}$$

where $a(\omega)$ is the source strength. By evaluating the integral over s we obtain the following zero-order WKBJ solution for the downgoing field

$$D_0(z) = A(k_0)\left[\Gamma(z)\right]^{-\frac{1}{2}}\exp\left(\mathrm{i}k_0\int_0^z \mathrm{d}z'\,\Gamma(z')\right)\,. \tag{5.24}$$

It is convenient to characterize the phase of the incident field in terms of the difference between wave propagation in models without and with the influence of the velocity potential. Equation (5.24) then can be written

$$D_0(z) = A(k_0)\left[\Gamma(z)\right]^{-\frac{1}{2}}\exp\left(\mathrm{i}k_0\left[z - \xi(z)\right]\right)\,, \tag{5.25}$$

where the WKBJ shift function

$$\xi = \xi_{\mathrm{W}}(z) = \int_{-\infty}^{z} \mathrm{d}z' \, [1 - \Gamma(z')] \tag{5.26}$$

now picks up the additional phase caused by the velocity potential. The WKBJ shift function obeys the differential equation

$$-2\xi_{\mathrm{W}}' + (\xi_{\mathrm{W}}')^2 + \alpha_c = 0 \quad , \quad \xi_{\mathrm{W}}^{(n)} = 0 \ , \ \ n \geq 2\,. \tag{5.27}$$

The zero of the second and higher order derivatives of the shift function implies that it inside a layer must vary slowly over a wavelength.

The scattered field is solved in the first-order WKBJ approximation, as shown in Appendix 5.B, where the zero-order WKBJ approximation incident field (5.25) is substituted into the differential equation (5.19). The scattered field then satisfies the linear first order differential equation

$$\frac{\mathrm{d}U_1(z)}{\mathrm{d}z} + [\mathrm{i}k_0\Gamma(z) - s(z)]\, U_1(z) = -s(z) D_0(z)\,. \tag{5.28}$$

Taking into account the radiation condition, $U(\infty) = 0$ (no scattered (upgoing) waves at infinity) the solution for the scattered field at the measurement level is

$$U_1(z = 0) = A(k_0) \int_0^{\infty} \mathrm{d}z \, s(z) \exp\left(2\mathrm{i}k_0 \, [z - \xi(z)]\right) \,. \tag{5.29}$$

Thus, the scattered field is an integral over all depths of the derivative of the logarithm of the acoustic velocity ratio, retarded by two-way traveltimes.

5.2.3 The single scattering forward model

It is convenient to express the single scattering data in terms of the dimensionless scattering amplitude $\Phi = A^{-1}U_1$. Our objective is to analyze the logarithmic changes of the acoustic potential, and not the vertical derivatives as expressed by the scattering function s in equation (5.18). A partial integration in equation (5.29) leads to the following result for the dimensionless scattering amplitude

$$\Phi(k_0) = -\frac{\mathrm{i}k_0}{2} \int_0^{\infty} \mathrm{d}z \, \alpha(z) \exp\left(2\mathrm{i}k_0 \, [z - \xi(z)]\right) \,, \tag{5.30}$$

where $\alpha(z)$ is the scattering potential

$$\alpha(z) = -2\ln\left[\Gamma(z)\right]\Gamma(z)\,. \tag{5.31}$$

The forward model presented in Chapter 4 and in Amundsen *et al* (2005b) is a special case of the model (5.30). When

$$\frac{(\alpha_c)^2}{24} \ll 1 \tag{5.32}$$

the following approximation is reasonable[1]

$$\left[1-\alpha_c(z)\right]^{\frac{1}{2}}\ln\left[1-\alpha_c(z)\right] \approx -\alpha_c(z)\,, \tag{5.33}$$

and the potential $\alpha(z)$ can be written

$$\alpha(z) \approx \alpha_c(z)\,. \tag{5.34}$$

Thus, the approximation $\alpha(z) \approx \alpha_c(z)$ yields the single scattering forward model used in Chapter 4 and in Amundsen *et al* (2005b).

Equation (5.30) is a non-linear forward model for computing the dimensionless scattering amplitude $\Phi(k)$ from the potential α. The single scattering amplitude is found by performing an integral over depth over the product of an amplitude function and a delay function. The amplitude function is the scattering potential. The delay function consists of the product of two functions, where the first $\exp(2\mathrm{i}k_0 z)$ accounts for two-way wave propagation of the unperturbed wave in the reference medium, whereas the second $\exp[-2\mathrm{i}k_0\xi(z)]$ corrects for the influence of the potential. Since the scattered wave $U_1(z)$ travels through the same potential $\alpha(z)$ as the incident wave $D_0(z)$ the shift function $\xi(z)$ is the same for both cases. For a piecewise-constant layered medium the delay function in the WKBJ approximation predicts the exact traveltimes of the single scattering events. However, performing the integral over depth, the predicted amplitudes of the single scattering events will not be exact for the piecewise-constant layered medium

---

[1] We have used that

$$(1-x)^{\frac{1}{2}}\ln(1-x) \approx -x + \frac{x^3}{24} + \frac{x^4}{24} + \ldots$$

unless the boundary conditions of continuity of the pressure and the vertical component of the particle velocity at the interfaces are explicitly introduced. For the sake of forward modeling, the boundary conditions easily can be accounted for. Interfaces or discontinuities in the potential are then treated by correctly coupling the incident wave to the scattered waves. However, for the inverse problem, where the location of interfaces is not known, it would be cumbersome to account for the continuity conditions in an explicit manner. Therefore, we choose to neglect these conditions at the expense of using a forward model that predicts slightly incorrect amplitudes of the single scattering events.

We will later compare the two forward models presented in this section (with scattering potentials $\alpha(z)$ and $\alpha_c(z)$, respectively) against an exact forward model. We will in particular be considering the amplitude handling of the two forward models.

5.3 Inverse scattering

The inverse scattering problem consists of reconstructing the potential α from the dimensionless scattering amplitude $\Phi(k)$ (the single scattering data measured at depth $z = 0$).

We refer the reader to Chapter 4 for a more detailed description of the inversion approach. Here we will give a overview of the main elements in the inversion method.

The inversion method is obtained in three main steps. In step one the Born potential profile is computed by constant-velocity imaging (migration) of the single scattering data in the time domain. Generally, interfaces in the Born potential are severely mislocated in depth compared to the true potential. In step two, a “squeezed” depth-dependent velocity potential is estimated by non-linear direct inversion of the Born potential. We denote this potential the “squeezed” potential since it mimics the actual velocity potential when the depth axis is squeezed. Step three estimates the actual depth-dependent velocity potential by stretching the squeezed potential so that the interfaces are moved towards the correct depth. The stretch function is a function of the Born potential. Thus, the solution for the velocity potential can be considered obtained by amplitude and shift adjusting the Born potential. No information other than the Born potential is required.

5.3.1 The Born potential and the single scattering data

As shown in Appendix 4.F, the inverse Fourier transform over frequency of equation (5.30) yields

$$4\int_{-\infty}^{2z/c_0} \mathrm{d}t'\Phi(t') = \sum_{n=0}^{\infty} \frac{1}{n!}\frac{\mathrm{d}^n}{\mathrm{d}z^n}\alpha(z)\xi^n(z)\,, \tag{5.35}$$

where $z = c_0 t/2$. In the Born approximation, the shift function is zero. By considering $\xi = 0$ in the forward model (5.30), and inverse Fourier transforming over frequency, the Born potential, per definition, is obtained:

$$\alpha_{\mathrm{B}}(z) \equiv 4\int_{-\infty}^{2z/c_0} dt'\Phi(t')\,. \tag{5.36}$$

Equation (5.36), which amounts to data trace integration of single scattering events, is known as linear migration-inversion. The primary events are placed at depths computed linearly using their traveltimes together with the constant reference velocity. Thus, the trace integration yields the Born approximation of the scattering potential. Equation (5.35) therefore can be written

$$\alpha_{\mathrm{B}}(z) = \sum_{n=0}^{\infty} \frac{1}{n!}\frac{\mathrm{d}^n}{\mathrm{d}z^n}\alpha(z)\xi^n(z)\,. \tag{5.37}$$

Given the Born potential $\alpha_{\mathrm{B}}(z)$ associated with constant-velocity imaging of single scattering data, our goal is now to use equation (5.37) as the basis for solving the inverse scattering problem in the WKBJ approximation.

In Appendix 4.D it is shown that by neglecting terms $\mathrm{d}^n\xi/\mathrm{d}z^n$ for $n = 2, ..., \infty$, we can write equation (5.37) as an infinite sum where the nth term is proportional to the nth power of the derivative of the shift function,

$$\alpha_{\mathrm{B}}(z) \approx \sum_{n=0}^{\infty}\left(\frac{\mathrm{d}\xi(z)}{\mathrm{d}z}\right)^n \sum_{m=n}^{\infty}\frac{1}{(m-n)!}\left(\begin{array}{c} m \\ n \end{array}\right)\xi^{m-n}(z)\frac{\mathrm{d}^{m-n}\alpha(z)}{\mathrm{d}z^{m-n}}\,. \tag{5.38}$$

Equation (5.38) is a new basis for deriving a closed-form solution for α.

5.3.2 Estimation of the squeezed velocity potential $\hat{\alpha}_c$ from α_{B}

We now show that we can predict what the velocity potential is, not as a function of the true depth, but as a function of the interface depths provided by the Born potential. This potential which is predicted from α_B is called a "squeezed" velocity potential, denoted $\hat{\alpha}_c$, because it mimics the actual velocity potential when the depth axis is squeezed so that the discontinuities of the actual velocity potential match those of the Born potential.

Inside a layer, velocities are assumed to vary smoothly with depth. It is then reasonable to disregard in equation (5.38) all derivatives of α. The non-zero terms in equation (5.38) arrive for all $n = m$, giving

$$\alpha_{\mathrm{B}}(z) \approx \hat{\alpha}(z) \sum_{n=0}^{\infty} \left[1 - (1 - \hat{\alpha}_c(z))^{\frac{1}{2}} \right]^n \quad , \quad \frac{\mathrm{d}^{n+1}\alpha(z)}{\mathrm{d}z^{n+1}} = 0 \, . \tag{5.39}$$

The sum is a geometric series, and we find

$$\alpha_{\mathrm{B}}(z) \approx \hat{\alpha}(z)[1 - \hat{\alpha}_c(z)]^{-\frac{1}{2}} \, . \tag{5.40}$$

By inserting equation (5.31) for $\hat{\alpha}(z)$, we find

$$\alpha_{\mathrm{B}}(z) = -2 \ln[1 - \hat{\alpha}_c(z)]^{\frac{1}{2}} \, . \tag{5.41}$$

Solving for $\hat{\alpha}_c(z)$ now gives

$$\hat{\alpha}_c(z) = 1 - \exp\left[-\alpha_{\mathrm{B}}(z)\right] \, . \tag{5.42}$$

Equation (5.42) shows that once α_{B} has been derived, then the squeezed velocity potential estimate $\hat{\alpha}_c(z)$ can be obtained. The only information that is required for this estimation is the Born potential itself.

5.3.3 Stretching of the squeezed velocity potential towards the actual velocity potential

For the 1D inverse scattering problem, Amundsen *et al* (2005a, 2005b) have shown how the squeezed velocity potential can be non-linearly stretched with respect to the depth axis so that the potential discontinuities are moved towards their correct location. We will here follow the same procedure.

Equation (5.38) is a basis for deriving a closed-form solution for α. To this end, the Fourier representation of $\alpha(z)$ is introduced, which gives

$$\alpha_{\mathrm{B}}(z) \quad \approx \quad \sum_{n=0}^{\infty} \left(\frac{\mathrm{d}\xi(z)}{\mathrm{d}z} \right)^n \frac{1}{2\pi} \int_{-\infty}^{\infty} \mathrm{d}k D_n(k\xi) \exp(-\mathrm{i}kz) \alpha(k) \, , \tag{5.43}$$

where

$$D_n(k\xi) = \sum_{m=n}^{\infty} \frac{1}{(m-n)!} \begin{pmatrix} m \\ n \end{pmatrix} [-\mathrm{i}k\xi(z)]^{m-n} \,. \tag{5.44}$$

The sum D_n can be written

$$D_n(k\xi) = \exp[-\mathrm{i}k\xi(z)] \sum_{m=0}^{n} \frac{1}{m!} \begin{pmatrix} n \\ m \end{pmatrix} [-\mathrm{i}k\xi(z)]^{n-m} \,, \tag{5.45}$$

and the expression for the Born potential then becomes

$$\alpha_{\mathrm{B}}(z) \approx$$
$$\frac{1}{2\pi}\int_{-\infty}^{\infty} \mathrm{d}k \left\{ \sum_{n=0}^{\infty} \left(\frac{\mathrm{d}\xi(z)}{\mathrm{d}z}\right)^n \sum_{m=0}^{n} \frac{1}{m!} \begin{pmatrix} n \\ m \end{pmatrix} [-\mathrm{i}k\xi(z)]^{n-m} \right\} \exp[-\mathrm{i}k(z+\xi(z))]\alpha(k) \,. \tag{5.46}$$

In equation (5.46) the double sum can be written as a single sum that is recognized as an expression for the exponential function,

$$\begin{aligned} \sum_{n=0}^{\infty} \left(\frac{\mathrm{d}\xi(z)}{\mathrm{d}z}\right)^n \sum_{m=0}^{n} \frac{1}{m!} \begin{pmatrix} n \\ m \end{pmatrix} [-\mathrm{i}k\xi(z)]^{n-m} &= \\ \frac{1}{1-\xi'(z)} \sum_{n=0}^{\infty} \frac{(-1)^n}{n!} \left(\frac{\mathrm{i}k\xi(z)\xi'(z)}{1-\xi'(z)}\right)^n & \\ = \frac{1}{1-\xi'(z)} \exp\left(-\frac{\mathrm{i}k\xi(z)\xi'(z)}{1-\xi'(z)}\right) \,. & \end{aligned} \tag{5.47}$$

The Born potential in equation (5.46) now reads

$$\alpha_{\mathrm{B}}(z) \approx \left(1 - \frac{\mathrm{d}\xi(z)}{\mathrm{d}z}\right)^{-1} \frac{1}{2\pi}\int_{-\infty}^{\infty} \mathrm{d}k \exp\left[-\mathrm{i}k\left(z + \frac{\xi(z)}{1-\xi'(z)}\right)\right] \alpha(k) \,. \tag{5.48}$$

Using the translation property of the Fourier transform, we obtain a closed-form expression for the Born potential,

$$\alpha_{\mathrm{B}}(z) \approx \left(1 - \frac{\mathrm{d}\xi(z)}{\mathrm{d}z}\right)^{-1} \alpha\left(z + \frac{\xi(z)}{1 - \frac{\mathrm{d}\xi(z)}{\mathrm{d}z}}\right) \,. \tag{5.49}$$

As shown in Chapter 4, equation (5.49) can be improved by introducing two new approximations, both which are valid in the WKBJ approximation. First, under the WKBJ assumption that $\xi''(z)$ is negligible, the replacement

$$\frac{\xi(z)}{1-\frac{\mathrm{d}\xi(z)}{\mathrm{d}z}} \rightarrow \int_{-\infty}^{z} \mathrm{d}z' \, \frac{\frac{\mathrm{d}\xi(z')}{\mathrm{d}z'}}{1-\frac{\mathrm{d}\xi(z')}{\mathrm{d}z'}} \quad , \quad \xi''(z) = 0 \, , \tag{5.50}$$

is justified. Second, when $\xi''(z)$ and all higher-order derivatives are disregarded, the following replacement is justified:

$$[1-\alpha_c(z)]^{-\frac{1}{2}} \rightarrow [1-\hat{\alpha}_c(z)]^{-\frac{1}{2}} \quad , \quad \frac{\mathrm{d}^n \xi(z)}{\mathrm{d}z^n} = 0 \quad , \quad n \geq 2 \, . \tag{5.51}$$

Inserting the two approximations into equation (5.49) and recalling equation (5.26) give the result

$$\alpha_{\mathrm{B}}(z) \;\; \approx \;\; [1-\hat{\alpha}_c(z)]^{-\frac{1}{2}} \, \alpha\left(z + \int_{-\infty}^{z} \mathrm{d}z' \, \left[(1-\hat{\alpha}_c(z'))^{-\frac{1}{2}} - 1\right]\right) . \tag{5.52}$$

By using the relationship (5.40) between the Born potential α_{B} and the squeezed potential $\hat{\alpha}$, equation (5.52) can be re-written in the following form:

$$\hat{\alpha}(z) = \alpha\left(z + \int_{-\infty}^{z} \mathrm{d}z' \, \left[(1-\hat{\alpha}_c(z'))^{-\frac{1}{2}} - 1\right]\right) . \tag{5.53}$$

The scattering potential α and the velocity potential α_c have the same potential discontinuities in depth. The shift function of the velocity potential must therefore obey the same shift-formula as the scattering potential, that is

$$\hat{\alpha}_c(z) = \alpha_c\left(z + \int_{-\infty}^{z} \mathrm{d}z' \, \left[(1-\hat{\alpha}_c(z'))^{-\frac{1}{2}} - 1\right]\right) . \tag{5.54}$$

Observe that the non-linear shift function is a function of the Born potential. Thus, the solution for the velocity potential can be considered obtained by amplitude and shift adjusting the Born potential.

Provided that the Born potential has been computed according to equation (5.36), then equations (5.42)and (5.54) suggest a two-step solution for the velocity potential α_c. First, the squeezed potential $\hat{\alpha}_c$ is estimated from the Born potential according to equation (5.42). Then the potential α_c is derived as a non-linear shift of $\hat{\alpha}_c$ according to equation (5.54). The non-linear shift is seen to correspond to stretching the depth axis of the squeezed potential result, $\hat{\alpha}_c$. The effect of shifting is to locate interfaces that are mislocated in $\hat{\alpha}_c$ towards their correct location. Thus, in the absence of the actual velocity function, the scale and shift algorithm extracts the necessary information from the Born depth profile $\alpha_{\mathrm{B}}(z)$.

5.4 Comparing forward models with regards to amplitude handling

In this section we compare the amplitude handling of the two forward models described previously. The amplitudes of the forward models are compared against the exact amplitudes from an exact forward model for primary reflections in a piecewise-constant layered medium. This exact model is described in Appendix 4.A. The performance of the forward model (5.30) with respect to amplitude handling is derived in Appendix 5.A.

Exact modeling in the frequency domain of the N events of the dimensionless scattering amplitude can be performed according to

$$\Phi_{\mathrm{X}}(\omega) = \sum_{n=1}^{N} \hat{R}_n \exp\left(2\mathrm{i}\omega \sum_{m=0}^{n-1} \frac{h_m}{c_m}\right) , \tag{5.55}$$

where each wave has the form of the product of an amplitude function and a delay function. The frequency dependency comes only as a complex exponential due to the delay. The amplitude of the wave from the interface at depth z_n is the product of the plane-wave reflection coefficient at z_n and the transmission coefficients encountered by the wave, namely

$$\hat{R}_1 = R_1 \ , \ \ \hat{R}_n = R_n \prod_{j=1}^{n-1} \left(1 - R_j^2\right) \ , \ \ n = 2, 3, ..., N \, . \tag{5.56}$$

For the piecewise-constant layered medium the frequency response in the WKBJ model gives

$$\Phi_{\mathrm{W}}(\omega) = \sum_{n=1}^{N} \Upsilon_n \exp\left(2\mathrm{i}\omega \sum_{m=0}^{n-1} \frac{h_m}{c_m}\right) , \tag{5.57}$$

where the amplitude of the wave from the interface at depth z_n is

$$\Upsilon_n = \frac{c_n}{4c_0}\alpha_n - \frac{c_{n-1}}{4c_0}\alpha_{n-1} \ , \ \ n = 1, 2, ..., N \, . \tag{5.58}$$

By comparing the modeling schemes (5.55) and (5.57) we observe that the delay functions are equal but that the amplitude functions differ.

We now consider two numerical examples in order to analyze the amplitude error of the WKBJ forward models given by (5.30). Results for both $\alpha = -2 \ln [1 - \alpha_c]^{\frac{1}{2}} \, [1 - \alpha_c]^{\frac{1}{2}}$ and $\alpha = \alpha_c$ are presented and compared. First we consider a ten-layer medium with reference velocity $c_0 = 1500$ m/s. Next we consider a fifteen-layer medium with reference velocity $c_0 = 1500$ m/s. The major difference between these two media is the sea-bottom properties. In the ten-layer medium there is a high contrast in velocity at the sea-bottom while in the fifteen layer medium there is a more gradual increase in velocity at the sea-bottom. The velocity profiles of the ten-layer medium and the fifteen-layer medium are given in figures 5.2a and 5.4a, respectively. The amplitude responses for the ten-layer medium and the fifteen layer medium are presented in tables 5.1 and 5.2, respectively.

The analytic studies and the numerical examples show that the forward scattering model given by equation (5.30) performs more accurately with regards to the amplitude handling when the scattering potential is represented by $\alpha = -2 \ln [1 - \alpha_c]^{\frac{1}{2}} \, [1 - \alpha_c]^{\frac{1}{2}}$ compared to the $\alpha = \alpha_c$ representation. The amplitude error for the ten-layer example ranges from approximately 0.5 to 3 percent and 1.5 to 15.5 percent, respectively, for the two representations. For the fifteen-layer medium the amplitude errors are significantly smaller (the ranges are approximately 0 to 2 percent and 0 to 14.5 percent for the two representations). The amplitude errors are smaller for the fifteen-layer medium due to the fact that the velocity contrast between layers and then also the reflection coefficient are smaller for the fifteen-layer medium than on the ten-layer medium. Amundsen *et al* (2005b) showed that the forward scattering model is more accurate for those media where the product of any three reflection coefficients is small compared to the reflection coefficients themselves.

5.5 Comparing the inverse solutions

In this section we compare three different solutions of the inverse scattering problem.

For the forward scattering model given by equations (5.30) and (5.31) the squeezed velocity potential is determined from the Born potential by

$$\hat{\alpha}_c(z) = 1 - \exp\left[-\alpha_{\mathrm{B}}(z)\right] . \tag{5.59}$$

An approximation to (5.60) which is exact for the single-interface problem is[2],

$$\hat{\alpha}_c(z) \approx \frac{\alpha_{\mathrm{B}}(z)}{(1+\alpha_{\mathrm{B}}(z)/4)^2} . \tag{5.60}$$

By considering the approximation $\alpha(z) \approx \alpha_c(z)$ in the single scattering forward model given by equation (5.30) we obtain the squeezed velocity potential formula developed in Chapter 4

$$\hat{\alpha}_c(z) = \left[\left(1 + \frac{1}{4}\alpha_{\mathrm{B}}^2(z)\right)^{\frac{1}{2}} - \frac{1}{2}\alpha_{\mathrm{B}}(z)\right]\alpha_{\mathrm{B}}(z) . \tag{5.61}$$

The three different inverse solutions for the squeezed velocity potential given by equations (5.59), (5.60) and (5.61) are subject to comparison with regards to how accurate the layer depths and layer velocities are estimated.

We consider the same models as in the previous section – the ten-layer medium and the fifteen-layer medium. Synthetic data are generated based on the exact forward model described in Appendix 4.A. The synthetic data for the ten-layer medium and the fifteen-layer medium are displayed in figures 5.1 and 5.3, respectively. We then apply the different inverse scattering solutions described above. Recall that the inverse solution is obtained in three steps. First, the Born potential is computed by constant-velocity migration of the single scattering data. Second, the squeezed velocity potential is estimated

---

[2] We have written

$$\exp[-\alpha_{\mathrm{B}}] = \left(\frac{\exp[-\alpha_{\mathrm{B}}/4]}{\exp[\alpha_{\mathrm{B}}/4]}\right)^2 \approx \left(\frac{1-\alpha_{\mathrm{B}}/4}{1+\alpha_{\mathrm{B}}/4}\right)^2$$

by nonlinear direct inversion of the Born potential. Third, the actual velocity potential is estimated by stretching the estimated squeezed velocity potential according to equation (5.54). The estimated velocity profiles from the different inverse solutions of the ten-layer medium and fifteen-layer medium are given in figures 5.2b and 5.4b, respectively. The estimated layer depths and layer velocities for the ten-layer medium and fifteen layer medium are presented in tables 5.3 and 5.5, respectively. The estimated velocity potentials for the two media are presented in tables 5.4 and 5.6.

The numerical examples show that the inversion scheme given by (5.59) gives the most accurate estimates of the layer depths and layer velocities for both media considered. The inversion method gives very good estimates for both layer depths and layer velocities with errors below 0.5 percent for the ten-layer medium and below 0.2 percent for the fifteen-layer medium. The other inversion schemes give sligthly higher errors, but still perform quite well. The errors are consistently higher for the ten-layer medium than for the fifteen-layer medium. This is consistent with the observations done when analyzing the amplitude prediction in the forward scattering model developed in this chapter and Chapter 4.

5.6 Conclusions

In this paper we have derived a new and improved physical model for single scattering of acoustic waves in a 1D stratified medium based on the first-order WKBJ approximation. The analytic studies and the numerical examples showed that the improved forward scattering model performed more accurately with regards to amplitude handling compared to the forward model presented in Chapter 4. An improved forward model also yields more accurate inversion results. The numerical examples showed that the inversion scheme based on the improved forward model gave more accurate estimates of the layer depths and layer velocities compared estimates based on the model in Chapter 4.

Acknowledgments

H. K. H. thanks Statoil for financial support.

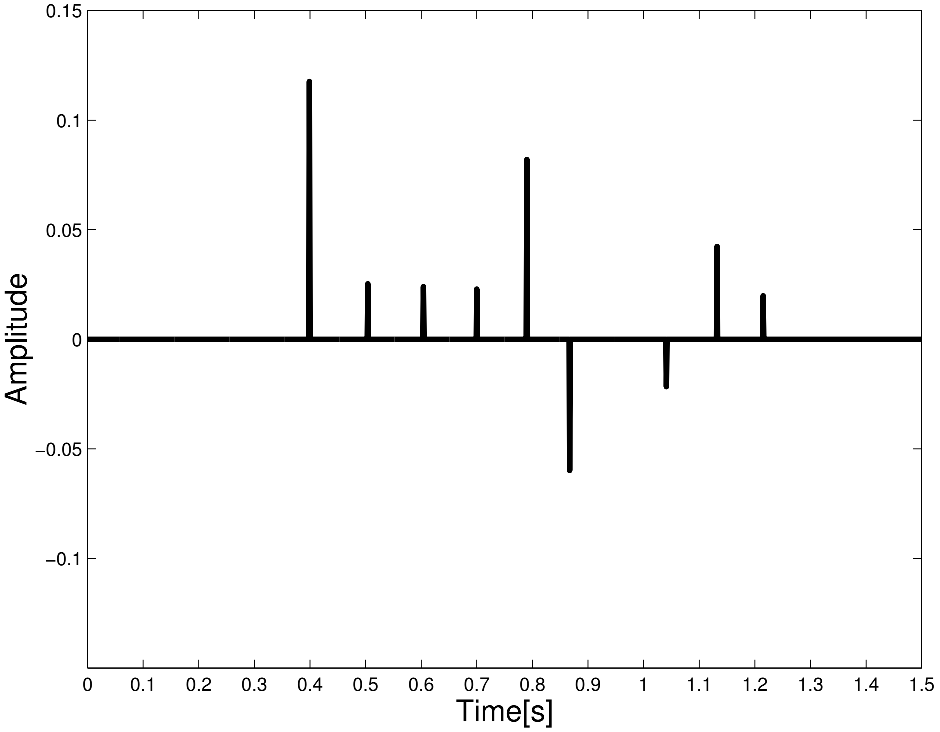

Figure 5.1: The modeled data for the ten-layer medium example.

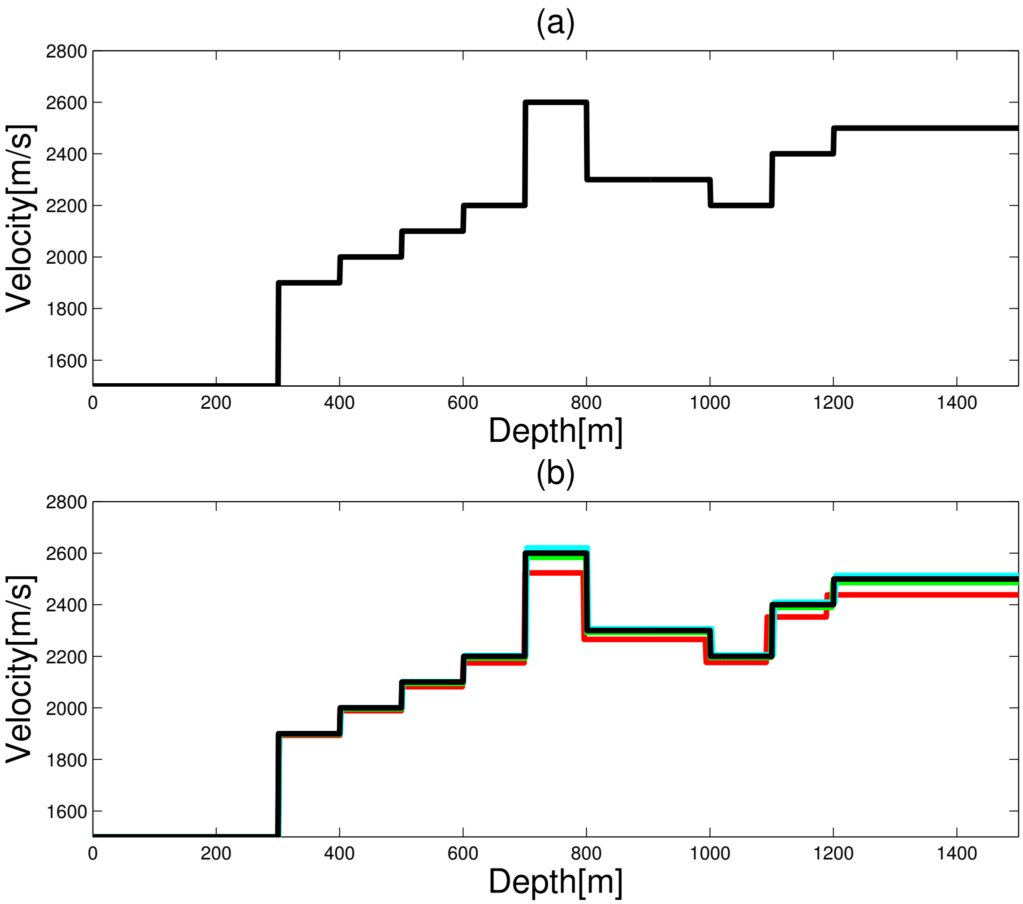

Figure 5.2: The ten-layer medium. (a) The actual velocity model. (b) The estimated velocity models obtained from the estimated squeezed velocity potentials given by (5.59), (5.60) and (5.61) in green, turquoise and red, respectively. The estimated velocity models are obtained by stretching the estimated squeezed velocity potentials according to equation (5.54) and solving for the velocity model $c(z)$ using the relationship (5.9) between the velocity potential and the velocity model. For the purpose of comparison, the actual velocity model is re-plotted in black.

Table 5.1: Ten-layer medium with reference velocity $c_0 = 1500$ m/s. Here, R_n is the reflection coefficient, $\hat{R}_n$ is the effective reflection coefficient (the product of the reflection coefficient and the transmission coefficients), $\Upsilon_n(\alpha_c)$ is the analytically derived primary reflection amplitude using $\alpha = \alpha_c$, $\Delta\Upsilon_n(\alpha_c)$ is the error $(|(\hat{R}_n - \Upsilon_n)/\hat{R}_n|)$ in $\Upsilon_n(\alpha_c)$ relative to the effective reflection coefficient, $\Upsilon_n(\alpha)$ is the analytically derived primary reflection amplitude using $\alpha = -2\ln\left[1-\alpha_c\right]^{\frac{1}{2}}\left[1-\alpha_c\right]^{\frac{1}{2}}$ and $\Delta\Upsilon_n(\alpha)$ is the error in $\Upsilon_n(\alpha)$ relative to the effective reflection coefficient.

n	R_n	$\hat{R}_n$	$\Upsilon_n(\alpha_c)$	$\Delta\Upsilon_n(\alpha_c)$ [%]	$\Upsilon_n(\alpha)$	$\Delta\Upsilon_n(\alpha)$ [%]
0	-	-	-	-	-	-
1	0.11760	0.11760	0.11930	1.4	0.11820	0.5
2	0.02564	0.02529	0.02654	4.9	0.02565	1.4
3	0.02439	0.02404	0.02560	6.5	0.02440	1.5
4	0.02326	0.02291	0.02478	8.2	0.02326	1.5
5	0.08333	0.08203	0.09289	13.2	0.08353	1.8
6	-0.06122	-0.05985	-0.06881	15.0	-0.06130	2.4
7	-0.02222	-0.02164	-0.02408	11.3	-0.02223	2.7
8	0.04348	0.04232	0.04754	12.3	0.04351	2.8
9	0.02041	0.01983	0.02292	15.6	0.02041	2.9

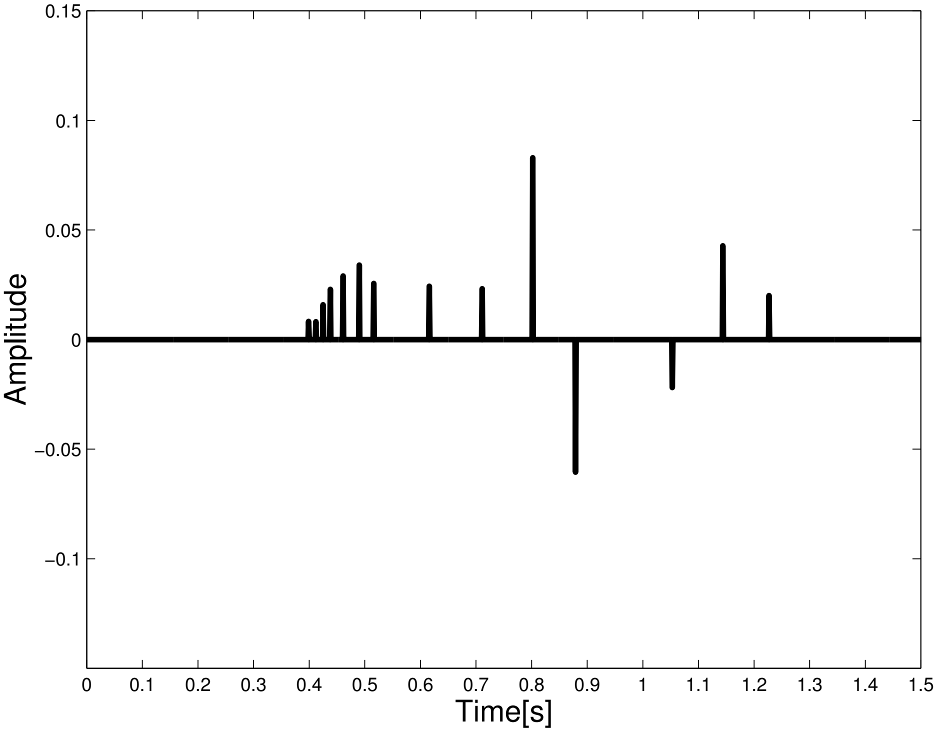

Figure 5.3: The modeled data for the fifteen-layer medium example.

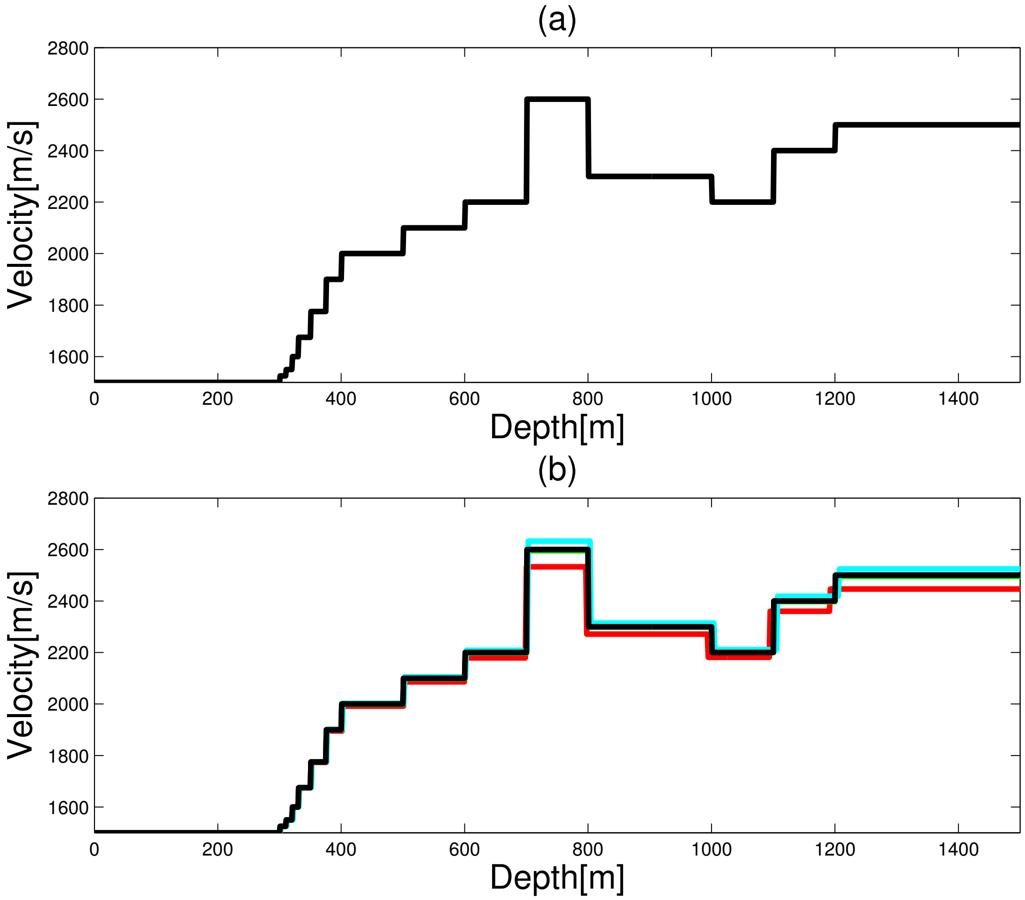

Figure 5.4: The fifteen-layer medium. (a) The actual velocity model. (b) The estimated velocity models obtained from the estimated squeezed velocity potentials given by (5.59), (5.60) and (5.61) in green (almost identical to the actual velocity model), turquoise and red, respectively. The estimated velocity models are obtained by stretching the estimated squeezed velocity potentials according to equation (5.54) and solving for the velocity model $c(z)$ using the relationship (5.9) between the velocity potential and the velocity model. For the purpose of comparison, the actual velocity model is re-plotted in black.

Table 5.2: Fifteen-layer medium with reference velocity $c_0 = 1500$ m/s. Here, R_n is the reflection coefficient, $\hat{R}_n$ is the effective reflection coefficient (the product of the reflection coefficient and the transmission coefficients), $\Upsilon_n(\alpha_c)$ is the analytically derived primary reflection amplitude using $\alpha = \alpha_c$, $\Delta\Upsilon_n(\alpha_c)$ is the error $(|(\hat{R}_n - \Upsilon_n)/\hat{R}_n|)$ in $\Upsilon_n(\alpha_c)$ relative to the effective reflection coefficient, $\Upsilon_n(\alpha)$ is the analytically derived primary reflection amplitude using $\alpha = -2\ln\left[1-\alpha_c\right]^{\frac{1}{2}}\left[1-\alpha_c\right]^{\frac{1}{2}}$ and $\Delta\Upsilon_n(\alpha)$ is the error in $\Upsilon_n(\alpha)$ relative to the effective reflection coefficient.

n	R_n	$\hat{R}_n$	$\Upsilon_n(\alpha_c)$	$\Delta\Upsilon_n(\alpha_c)$ [%]	$\Upsilon_n(\alpha)$	$\Delta\Upsilon_n(\alpha)$ [%]
0	-	-	-	-	-	-
1	0.00826	0.00826	0.00826	0.0	0.00826	0.0
2	0.00813	0.00813	0.00813	0.0	0.00813	0.0
3	0.01587	0.01587	0.01589	0.1	0.01587	0.0
4	0.02290	0.02289	0.02299	0.4	0.02290	0.1
5	0.02899	0.02896	0.02928	1.1	0.02899	0.1
6	0.03401	0.03395	0.03473	2.3	0.03403	0.2
7	0.02564	0.02557	0.02654	3.8	0.02565	0.3
8	0.02439	0.02430	0.02560	5.3	0.02440	0.4
9	0.02326	0.02316	0.02478	7.0	0.02326	0.4
10	0.08333	0.08294	0.09289	12.0	0.08353	0.7
11	-0.06122	-0.06051	-0.06881	13.7	-0.06130	1.3
12	-0.02222	-0.02188	-0.02408	10.0	-0.02223	1.6
13	0.04348	0.04279	0.04754	11.1	0.04351	1.7
14	0.02041	0.02005	0.02292	14.3	0.02041	1.8

Table 5.3: Ten-layer medium with reference velocity $c_0 = 1500$ m/s. Here, z_n is the actual layer depth, $\hat{z}_{n\mathrm{W1}}$, $\hat{z}_{n\mathrm{W2}}$ and $\hat{z}_{n\mathrm{W3}}$ are the estimated layer depths obtained from stretching the estimated squeezed potentials given by (5.59), (5.60) and (5.61), respectively. c_n is the actual layer velocity, $\hat{c}_{n\mathrm{W1}}$, $\hat{c}_{n\mathrm{W2}}$ and $\hat{c}_{n\mathrm{W3}}$ are the estimated layer velocities obtained from the estimated squeezed potentials (5.59), (5.60) and (5.61), respectively. $\Delta\hat{c}_{n\mathrm{W1}}$, $\Delta\hat{c}_{n\mathrm{W2}}$ and $\Delta\hat{c}_{n\mathrm{W3}}$ are the errors in $\hat{c}_{n\mathrm{W1}}$, $\hat{c}_{n\mathrm{W2}}$ and $\hat{c}_{n\mathrm{W3}}$, respectively, relative to the actual velocity.

n	$z_n[m]$	$\hat{z}_{n\mathrm{W1}}$[m]	$\hat{z}_{n\mathrm{W2}}$[m]	$\hat{z}_{n\mathrm{W3}}$[m]
0	0	0	0	0
1	300	300	300	300
2	400	400	400	401
3	500	501	501	500
4	600	600	601	599
5	700	701	702	699
6	800	799	801	795
7	1000	999	1003	993
8	1100	1099	1103	1091
9	1200	1198	1203	1188

n	c_n[m/s]	$\hat{c}_{n\mathrm{W1}}$[m/s]	$\Delta\hat{c}_{n\mathrm{W1}}$[%]	$\hat{c}_{n\mathrm{W2}}$[m/s]	$\Delta\hat{c}_{n\mathrm{W2}}$[%]	$\hat{c}_{n\mathrm{W3}}$[m/s]	$\Delta\hat{c}_{n\mathrm{W3}}$[%]
0	1500	1500	0.0	1500	0.0	1500	0.0
1	1900	1898	0.1	1900	0.0	1894	0.3
2	2000	1996	0.2	2000	0.0	1989	0.6
3	2100	2095	0.3	2101	0.1	2082	0.8
4	2200	2193	0.3	2203	0.1	2174	1.2
5	2600	2584	0.6	2620	0.8	2523	3.0
6	2300	2292	0.3	2307	0.3	2266	1.5
7	2200	2195	0.2	2206	0.3	2176	1.1
8	2400	2389	0.5	2410	0.4	2353	2.0
9	2500	2486	0.6	2514	0.5	2438	2.5

Table 5.4: Ten-layer medium with reference velocity $c_0 = 1500$ m/s. Here, α_n is the actual velocity potential, $\hat{\alpha}_{n\mathrm{W1}}$, $\hat{\alpha}_{n\mathrm{W2}}$ and $\hat{\alpha}_{n\mathrm{W3}}$ are the estimated velocity potentials obtained from the estimated squeezed potentials (5.59), (5.60) and (5.61), respectively. Notice that α_n and $\hat{\alpha}_{n\mathrm{W2}}$ are exactly equal for n=1, in agreement with the construction of the solution (5.60).

n	α_n	$\hat{\alpha}_{n\mathrm{W1}}$	$\hat{\alpha}_{n\mathrm{W2}}$	$\hat{\alpha}_{n\mathrm{W3}}$
0	0.0000	0.0000	0.0000	0.0000
1	0.3767	0.3754	0.3767	0.3727
2	0.4375	0.4355	0.4377	0.4312
3	0.4898	0.4872	0.4904	0.4811
4	0.5351	0.5321	0.5364	0.5240
5	0.6672	0.6630	0.6723	0.6466
6	0.5747	0.5718	0.5774	0.5616
7	0.5351	0.5331	0.5375	0.5250
8	0.6094	0.6058	0.6126	0.5935
9	0.6400	0.6359	0.6439	0.6215

Table 5.5: Fifteen-layer medium with reference velocity $c_0 = 1500$ m/s. Here, z_n is the actual layer depth, $\hat{z}_{n\mathrm{W}1}$, $\hat{z}_{n\mathrm{W}2}$ and $\hat{z}_{n\mathrm{W}3}$ are the estimated layer depths obtained from stretching the estimated squeezed potentials given by (5.59), (5.60) and (5.61), respectively. c_n is the actual layer velocity, $\hat{c}_{n\mathrm{W}1}$, $\hat{c}_{n\mathrm{W}2}$ and $\hat{c}_{n\mathrm{W}3}$ are the estimated layer velocities obtained from the estimated squeezed potentials (5.59), (5.60) and (5.61), respectively. $\Delta\hat{c}_{n\mathrm{W}1}$, $\Delta\hat{c}_{n\mathrm{W}2}$ and $\Delta\hat{c}_{n\mathrm{W}3}$ are the errors in $\hat{c}_{n\mathrm{W}1}$, $\hat{c}_{n\mathrm{W}2}$ and $\hat{c}_{n\mathrm{W}3}$, respectively, relative to the actual velocity.

n	$z_n[m]$	$\hat{z}_{n\mathrm{W}1}$[m]	$\hat{z}_{n\mathrm{W}2}$[m]	$\hat{z}_{n\mathrm{W}3}$[m]
0	0	0	0	0
1	300	300	300	300
2	310	310	310	310
3	320	320	320	320
4	330	330	330	330
5	350	350	350	350
6	375	376	376	376
7	400	401	401	401
8	500	502	502	501
9	600	600	601	600
10	700	700	701	698
11	800	800	803	797
12	1000	1000	1004	993
13	1100	1101	1106	1094
14	1200	1200	1205	1191

n	c_n[m/s]	$\hat{c}_{n\mathrm{W}1}$[m/s]	$\Delta\hat{c}_{n\mathrm{W}1}$[%]	$\hat{c}_{n\mathrm{W}2}$[m/s]	$\Delta\hat{c}_{n\mathrm{W}2}$[%]	$\hat{c}_{n\mathrm{W}3}$[m/s]	$\Delta\hat{c}_{n\mathrm{W}3}$[%]
0	1500	1500	0.0	1500	0.0	1500	0.0
1	1525	1525	0.0	1525	0.0	1525	0.0
2	1550	1550	0.0	1550	0.0	1550	0.0
3	1600	1600	0.0	1600	0.0	1600	0.0
4	1675	1675	0.0	1675	0.0	1675	0.0
5	1775	1775	0.0	1776	0.0	1773	0.1
6	1900	1900	0.0	1902	0.1	1895	0.2
7	2000	1999	0.1	2003	0.2	1992	0.4
8	2100	2099	0.0	2106	0.3	2086	0.7
9	2200	2198	0.1	2209	0.4	2179	0.9
10	2600	2595	0.2	2632	1.2	2533	2.6
11	2300	2299	0.0	2315	0.6	2272	1.2
12	2200	2201	0.0	2211	0.5	2181	0.8
13	2400	2397	0.1	2419	0.8	2360	1.7
14	2500	2495	0.2	2524	1.0	2447	2.1

Table 5.6: Fifteen-layer medium with reference velocity $c_0 = 1500$ m/s. Here, α_n is the actual velocity potential, $\hat{\alpha}_{n\text{W}1}$, $\hat{\alpha}_{n\text{W}2}$ and $\hat{\alpha}_{n\text{W}3}$ are the estimated velocity potentials obtained from the estimated squeezed potentials (5.59), (5.60) and (5.61), respectively.

n	α_n	$\hat{\alpha}_{n\text{W}1}$	$\hat{\alpha}_{n\text{W}2}$	$\hat{\alpha}_{n\text{W}3}$
0	0.0000	0.0000	0.0000	0.0000
1	0.0325	0.0325	0.0325	0.0325
2	0.0635	0.0635	0.0635	0.0635
3	0.1211	0.1211	0.1211	0.1210
4	0.1980	0.1980	0.1988	0.1976
5	0.2859	0.2857	0.2863	0.2846
6	0.3767	0.3764	0.3778	0.3737
7	0.4375	0.4370	0.4393	0.4327
8	0.4898	0.4892	0.4925	0.4830
9	0.5351	0.5344	0.5388	0.5262
10	0.6672	0.6659	0.6753	0.6492
11	0.5747	0.5743	0.5800	0.5640
12	0.5351	0.5354	0.5398	0.5271
13	0.6094	0.6085	0.6154	0.5960
14	0.6400	0.6387	0.6468	0.6241

Appendix 5.A

Modeling of the primary reflection response in the WKBJ approximation

In Appendix 4.A we showed how to model the primary reflection response of a medium with $N+1$ homogeneous layers. The primary reflection response is exact since the boundary conditions of continuity of the pressure and the vertical component of particle velocity were explicitly introduced at every boundary.

In the main text of this chapter we have noted that for a piecewise-constant layered medium the WKBJ forward model (5.30) predicts the exact traveltimes of single scattering events, but not exact amplitudes unless the boundary conditions inside the medium are explicitly accounted for. In this appendix we derive analytic expressions for the amplitude of the single scattering events when the boundary conditions are not explicitly introduced as for the WKBJ forward model.

As an illustration we consider plane-wave propagation in a medium consisting of two halfspaces above and below a single layer (two interfaces). The interfaces are at depths z_1 and z_2, and the source and the receiver are both located at depth $z = 0$ in the zero'th layer which is the reference medium with velocity c_0. The single layer has velocity c_1 and the lower halfspace has velocity c_2.

The forward model being considered is given by (5.30), that is,

$$\Phi_{\mathrm{W}}(\omega) = -\frac{\mathrm{i}k_0}{2}\int_0^{\infty} \mathrm{d}z\,\alpha(z)\exp\left(2\mathrm{i}k_0\left[z-\xi(z)\right]\right)\,, \tag{5-A-1}$$

where the WKBJ shift function

$$\xi(z) = \xi_{\mathrm{W}}(z) = \int_{-\infty}^{z}\mathrm{d}z'\left[1-\left(1-\alpha_c(z)\right)^{\frac{1}{2}}\right]. \tag{5-A-2}$$

The potential for this two interface model is

$$\alpha(z) = \begin{cases} 0 & z < z_1 \\ \alpha_1 & z_1 < z < z_2 \\ \alpha_2 & z \geq z_2. \end{cases} \tag{5-A-3}$$

The shift function becomes

$$\xi(z) = \begin{cases} 0 & z < z_1 \\ (1 - \frac{c_0}{c_1})(z - z_1) & z_1 < z < z_2 \\ (1 - \frac{c_0}{c_1})(z_2 - z_1) + (1 - \frac{c_0}{c_2})(z - z_2) & z \geq z_2 . \end{cases} \tag{5-A-4}$$

By evaluating the integral in (5-A-1), one obtains

$$\Phi_{\mathrm{W}}(\omega) = \frac{c_1 \alpha_1}{4c_0} \exp\left(2\mathrm{i}\omega \frac{h_0}{c_0}\right) + \frac{c_2\alpha_2 - c_1\alpha_1}{4c_0} \exp\left(2\mathrm{i}\omega \frac{h_1}{c_1}\right) \exp\left(2\mathrm{i}\omega \frac{h_0}{c_0}\right) , \tag{5-A-5}$$

where $h_0 = z_1$ and $h_2 = z_2 - z_1$.

For a piecewise-constant $N + 1$ layered medium the frequency response in the WKBJ model gives

$$\Phi_{\mathrm{W}}(\omega) = \sum_{n=1}^{N} \Upsilon_n \exp\left(2\mathrm{i}\omega \sum_{m=0}^{n-1} \frac{h_m}{c_m}\right) , \tag{5-A-6}$$

where the amplitude of the wave from the interface at depth z_n is

$$\Upsilon_n = \frac{c_n}{4c_0}\alpha_n - \frac{c_{n-1}}{4c_0}\alpha_{n-1} \ , \ \ n = 1, 2, ..., N \, . \tag{5-A-7}$$

and $h_m = z_{m+1} - z_m$. By comparing the modeling schemes (4-A-2) derived in Appendix 4.A and (5-A-6) we observe that the delay functions are equal but that the amplitude functions differ.

Appendix 5.B

The scattered field in the first-order WKBJ approximation

In this appendix we solve the linear first order differential equation (5.28) for the scattered field[3],

$$\frac{\mathrm{d}U_1(z)}{\mathrm{d}z} + \left(\mathrm{i}k_0[1 - \alpha_c(z)]^{\frac{1}{2}} - s(z)\right) U_1(z) = -s(z) D_0(z) \, . \tag{5-B-1}$$

---

[3] The linear first order differential equation

$$u'(z) + f(z)u(z) = g(z),$$

Letting

$$f(z) = \mathrm{i}k_0[1-\alpha_c(z)]^{\frac{1}{2}} - s(z)$$

$$g(z) = -s(z)D_0(z)$$

the solution for U_1 is

$$U_1(z) = \exp\left(-\int^z \mathrm{d}z' f(z')\right)\left[\int^z \mathrm{d}z' g(z') \exp\left(\int^{z'} \mathrm{d}z'' f(z'')\right) + C\right] \quad \text{(5-B-2)}$$

i.e.,

$$U_1(z) = \exp\left(-\int_\infty^z \mathrm{d}z' f(z')\right)\left[\int_\infty^z \mathrm{d}z' g(z') \exp\left(\int_\infty^{z'} \mathrm{d}z'' f(z'')\right) + C\right] \quad \text{(5-B-3)}$$

i.e.,

$$U_1(z) = -\exp\left(\int_z^\infty \mathrm{d}z' f(z')\right)\left[\int_z^\infty \mathrm{d}z' g(z') \exp\left(-\int_{z'}^\infty \mathrm{d}z'' f(z'')\right) - C\right]. \quad \text{(5-B-4)}$$

The radiation condition (no upgoing waves at infinity) gives $C = 0$. Then

$$U_1(z) = -\exp\left(\int_z^\infty \mathrm{d}z' f(z')\right)\int_z^\infty \mathrm{d}z' g(z') \exp\left(-\int_{z'}^\infty \mathrm{d}z'' f(z'')\right). \quad \text{(5-B-5)}$$

The integral in the exponential function becomes

$$\int_z^\infty \mathrm{d}z' f(z') = \mathrm{i}k_0 \int_z^\infty \mathrm{d}z' [1-\alpha_c(z')]^{\frac{1}{2}} - \int_z^\infty \mathrm{d}z' s(z'). \quad \text{(5-B-6)}$$

---

has the solution

$$u(z) = \exp\left(-\int^z \mathrm{d}z' f(z')\right)\left[\int^z \mathrm{d}z' g(z') \exp\left(\int^{z'} \mathrm{d}z'' f(z'')\right) + C\right].$$

The last integral gives

$$\begin{aligned}\int_z^\infty \mathrm{d}z' s(z') &= \int_z^\infty \mathrm{d}z' \frac{\mathrm{d}}{\mathrm{d}z'} \ln\left([1-\alpha_c(z')]^{-1/4}\right) \\ &= \ln\left([1-\alpha_c(z')]^{-1/4}\right)_z^\infty \\ &= -\ln\left([1-\alpha_c(z)]^{-1/4}\right) \qquad \text{(5-B-7)}\end{aligned}$$

hence,

$$\int_z^\infty \mathrm{d}z' f(z') = \ln\left([1-\alpha_c(z)]^{-1/4}\right) + \mathrm{i}k_0 \int_z^\infty \mathrm{d}z' [1-\alpha_c(z')]^{\frac{1}{2}}. \qquad \text{(5-B-8)}$$

Thus,

$$\exp\left(\int_z^\infty \mathrm{d}z' f(z')\right) = [1-\alpha_c(z)]^{-1/4} \exp\left(\mathrm{i}k_0 \int_z^\infty \mathrm{d}z' [1-\alpha_c(z')]^{\frac{1}{2}}\right) \qquad \text{(5-B-9)}$$

and

$$\exp\left(-\int_{z'}^\infty \mathrm{d}z'' f(z'')\right) = [1-\alpha_c(z')]^{1/4} \exp\left(-\mathrm{i}k_0 \int_{z'}^\infty \mathrm{d}z'' [1-\alpha_c(z'')]^{\frac{1}{2}}\right). \qquad \text{(5-B-10)}$$

Equation (5-B-5) now gives

$$\begin{aligned}U_1(z) = A(k_0) \exp\left(\mathrm{i}k_0 \int_z^\infty \mathrm{d}z' [1-\alpha_c(z')]^{\frac{1}{2}}\right) \\ \times \int_z^\infty \mathrm{d}z' s(z') \exp\left(\mathrm{i}k_0 \int_0^{z'} \mathrm{d}z'' \, [1-\alpha_c(z'')]^{\frac{1}{2}}\right) \exp\left(-\mathrm{i}k_0 \int_{z'}^\infty \mathrm{d}z'' [1-\alpha_c(z'')]^{\frac{1}{2}}\right).\end{aligned} \qquad \text{(5-B-11)}$$

Using that

$$\begin{aligned}\exp\left(\mathrm{i}k_0 \int_0^{z'} \mathrm{d}z'' \, [1-\alpha_c(z'')]^{\frac{1}{2}}\right) \exp\left(-\mathrm{i}k_= \int_{z'}^\infty \mathrm{d}z'' [1-\alpha_c(z'')]^{\frac{1}{2}}\right) = \\ \exp\left(2\mathrm{i}k_0 \int_0^{z'} \mathrm{d}z'' \, [1-\alpha_c(z'')]^{\frac{1}{2}}\right) \exp\left(-\mathrm{i}k_0 \int_0^\infty \mathrm{d}z' [1-\alpha_c(z')]^{\frac{1}{2}}\right),\end{aligned} \qquad \text{(5-B-12)}$$

equation (5-B-11) yields

$$U_1(z) = A(k_0)\exp\left(-\mathrm{i}k_0\int_0^z \mathrm{d}z'[1-\alpha_c(z')]^{\frac{1}{2}}\right)$$
$$\times\int_z^\infty \mathrm{d}z' s(z')\exp\left(2\mathrm{i}k_0\int_0^{z'}\mathrm{d}z''\,[1-\alpha_c(z'')]^{\frac{1}{2}}\right). \qquad (5\text{-B-}13)$$

The scattered field at $z = 0$ is

$$U_1(z=0) = A(k_0)\int_0^\infty \mathrm{d}z s(z)\exp\left(2\mathrm{i}k_0\int_0^z \mathrm{d}z'\,[1-\alpha_c(z')]^{\frac{1}{2}}\right), \qquad (5\text{-B-}14)$$

where the scattering function s is given in equation (5.18). In terms of the WKBJ shift function (5.26) the upgoing field is written

$$U_1(z=0) = A(k_0)\int_0^\infty \mathrm{d}z s(z)\exp\left(2\mathrm{i}k_0\,[z-\xi_{\mathrm{W}}(z)]\right). \qquad (5\text{-B-}15)$$

References

Amundsen L, Reitan A and Arntsen B 2005a Geometric analysis of data-driven inversion/depth imaging *Journal Seismic Exploration* **14** 51-62

Amundsen L, Reitan A, Helgesen H K and Arntsen B 2005b Data-driven inversion/depth imaging derived from approximations to one-dimensional inverse acoustic scattering *Inverse Problems* **21** 1823-1850

Bremmer H 1951 The W.K.B. approximation as a first term of a geometric-optical series *The theory of electromagnetic waves, A symposium* (New York: Interscience Publ.) p 169-179

Innanen K A 2003 *Methods for the treatment of acoustic and absorptive/dispersive wave field measurements* (Ph.D. thesis, University of British Columbia)

Innanen K A and Weglein A B 2003 Simultaneous imaging and inversion with the inverse scattering series *Proc. 8th Internat. Cong. of the SBGf and 5th Latin American Geophys. Conf.*

Liu F, Weglein A B, Innanen K A, and Nita B G, 2005, Extension of the non-linear depth imaging capability of the inverse scattering series to multidimensional media: strategies and numerical results *Proc. 9th Internat. Cong. of the SBGf and 6th Latin American Geophys. Conf.*

Razavy M 1975 Determination of the wave velocity in an inhomogeneous medium from the reflection coefficient *J. Acoust. Soc. Am.* **58** 956-963

Shaw S A 2005 *An inverse scattering series algorithm for depth imaging of reflection data from a layered acoustic medium with an unknown velocity model* (Ph.D. thesis, University of Houston)

Shaw S A, Weglein A B, Foster D J, Matson K H and Keys R G 2004 Isolation of a leading order depth imaging series and analysis of its convergence properties for a 1D acoustic medium *J. Seis. Expl.* **13** 99-120

Ursin B 1983 Review of elastic and electromagnetic wave propagation in horizontally layered media *Geophysics* **48** 1063-1081

Weglein A B 1985 The inverse scattering concept and its seismic application *Developments in Geophysical Exploration Methods* vol 6, ed A A Fitch (Amsterdam: Elsevier) pp 111-138

Weglein A B, Araújo R V, Carvalho P M, Stolt R H, Matson K H, Coates R T, Corrigan D, Foster D J, Shaw S A and Zhang H 2003 Inverse scattering series and seismic exploration *Inverse Problems* **19** R27-R83

Weglein A B, Foster D J, Matson K H, Shaw S A, Carvalho P M and Corrigan D 2002 Predicting the correct spatial location of reflectors without knowing or determining the precise medium and wave velocity: initial concept, and analytic and numerical example *J. Seis. Expl.* **10** 367-382

Weglein A B, Matson K H, Foster D J, Carvalho P M , Corrigan D and Shaw S A 2000 Imaging and inversion at depth without a velocity model: theory, concepts, and initial evaluation *Expanded Abstracts, 70th Ann. Internat. Mtg., Soc. Expl. Geophys.*

Zhang H and Weglein A B 2005 The inverse scattering series for tasks associated with primaries: depth imaging and direct non-linear inversion of 1D variable velocity and density acoustic media *Expanded Abstracts, 75th Ann. Internat. Mtg., Soc. Expl. Geophys.*